國立臺灣大學電機資訊學院光電工程學研究所

碩士論文

Graduate Institute of Photonics and Optoelectronics

College of Electrical Engineering and Computer Science

National Taiwan University

Master's Thesis

研究二維硫硒化鉬之特性及其用於金氧半互補式電晶體之設計

Study on the Properties of Two-Dimensional MoSSe and Its Complementary Metal-Oxide-Semiconductor Field-Effect Transistor Design

邱允平

Yun-Ping Chiu

指導教授: 吳育任 博士

Advisor: Yuh-Renn Wu Ph.D.

中華民國 113 年 8 月

August 2024

doi:10.6342/NTU202403452

國立臺灣大學碩士學位論文

口試委員會審定書

MASTER'S THESIS ACCEPTANCE CERTIFICATE
NATIONAL TAIWAN UNIVERSITY

研究二維硫硒化鉬之特性及其用於金氧半互補式電晶體之設計

Study on the Properties of Two-Dimensional MoSSe and Its Complementary Metal-Oxide-Semiconductor Field-Effect Transistor Design

本論文係邱允平君（學號 R11941075）在國立臺灣大學光電工程學研究所完成之碩士學位論文，於民國 113 年 7 月 22 日承下列考試委員審查通過及口試及格，特此證明

The undersigned, appointed by the Graduate Institute of Photonics and Optoelectronics, on 22 July 2024 have examined a Master's thesis entitled above presented by CHIU, YUN-PING (student ID: R11941075) candidate and hereby certify that it is worthy of acceptance.

口試委員 Oral examination committee:

（指導教授 Advisor）

吳育任　　陳宏彰　　吳肇欣

所長 Director: 吳育任

doi:10.6342/NTU202403452

Acknowledgements

看著新生坐在台下聆聽我的口試，讓我回想到兩年前剛進實驗室的自己，轉瞬間，碩士生涯即將結束，這兩年發生的一切已經十分精彩，足夠成為一段在未來不斷重複玩味的回憶。在這段旅程中，首先要感謝的就是指導教授 吳育任老師的細心照顧，無論是起初擔心材料系背景的我會適應不良、課程中第一次跟我線上改 code、在美國陪我們報告或是 OPTIC 在旅館大廳跟我改 paper 等。這段期間我向您學習到許多，也感謝老師願意等待我的緩慢進步，您這兩年給予的一切栽培對我的進步影響甚大，未來我也會繼續努力成為更好的人！接下來要感謝的是戰鬥好夥伴信雯，那些討論到夜深的時光仍歷歷在目，有妳的陪伴與幫助我很幸運。也感謝實驗室的其他夥伴，我們一起面對問題、討論學業與研究以及互相勉勵，讓我在做實驗時能提起精神並繼續前進。感謝學長姐的時常關照、修齊學長給的挑戰以及學弟妹的關懷與激勵，這些都成為了我現在的養分，支持著我讓我不斷成長。感謝家人無時無刻給我的無條件支持，感謝台科大 3D 夢工坊的欣萍與各位做我的精神支柱與避風港，感謝今晚不當菸酒桑的相互陪伴，讓我的碩士生活不再孤單，感謝 Deep Gangster 的各位替我在最苦的時候排解壓力一同歡笑。感謝計畫編號 NSTC 112-2221-E-002-215-MY3、NSTC 112-2923-E-002-002 以及 NSTC 112-2221-E-002-214-MY3 這兩年來的支持。最後感謝兩年來遇到風雨時，從未放棄的自己，即便下過雨的天空不一定會有彩虹，至少在過程中仍有雨點奏樂，期許未來的自己在面對任何風雨都能學會隨之起舞，逆風飛翔。

doi:10.6342/NTU202403452

摘要

近幾年出現的非對稱過渡金屬二硫屬化物 (JTMD) 因其卓越的光學和電學特性，吸引了廣泛關注。與傳統二維材料相比，JTMD 額外的本質偶極矩可以產生 n 型和 p 型接觸，可用於太陽能電池和針型二極體等器件。在本論文中，我們利用這一特性來構建同時包含 n 型和 p 型的金屬氧化物半導體互補式場效電晶體。首先，我們通過密度泛函理論計算研究了三層二維硫硒化鉬 (MoSSe) 中的自發偶極矩電場強度。再來，我們探討 MoSSe 的自發偶極矩與不同金屬在接觸時產生的能帶彎曲，並探討電子和電洞的如何在介面累積而形成 p 型、n 型甚至歐姆接觸。利用後續這該接觸特性，透過二維有限元的泊松漂移擴散求解器進行電晶體元件模擬，透過這些模擬幫助我們構建最佳的互補型場校電晶體維度。我們最終的研究結果顯示，透過適當的設計，我們可以只使用單一個 JTMD 材料作為通道層，設計同時包含 n 型與 p 型的互補型場校電晶體，且無需額外摻雜就能形成高濃度載子區域。除此之外，我們也針對二維硫硒化鉬進行光學吸收性值的探討，並將吸收相關之關鍵參數取出，以供未來光電元件模擬做使用。

關鍵字：二維非對稱型材料、密度泛涵理論、載子遷移率、吸收係數、二維材料電晶體

doi:10.6342/NTU202403452

Abstract

Janus transition metal dichalcogenides (JTMDs) have attracted extensive attention due to their exceptional optical and electrical properties. The extra intrinsic dipole moment of JTMDs can generate n-type and p-type contacts, which can be used for devices such as solar cells and pin diodes. Our work explores JTMDs for complementary metal-oxide-semiconductor field-effect transistors (CMOSFETs), enabling n- and p-type channels in a single material. Firstly, we investigate the spontaneous dipole field strength in layered MoSSe through density-functional theory. The MoSSe spontaneous polarization influences how it interacts with contacts, leading to Ohmic, p-type, or n-type contact formations. Utilizing these contact properties, we employed a finite element Poisson-drift-diffusion two-dimensional method to simulate the transistor device, and these simulations guided us to design the best dimensions for CMOSFETs. Our final results demonstrate that, through appropriate design, we can design CMOSFETs containing both n-type and p-type transistors using only a single JTMD material as the channel layer, and form high-

doi:10.6342/NTU202403452

carrier-density regions without additional doping. In addition, we investigated the optical absorption properties of two-dimensional MoSSe, extracting key absorption-related parameters for use in future optoelectronic device simulations.

Keywords: Janus Two-dimensional material, Density Functional Theory, Carrier Mobility, Absorption Coefficient, 2D Material Transistors

doi:10.6342/NTU202403452

Contents

Page

Verification Letter from the Oral Examination Committee **i**

Acknowledgements **ii**

摘要 **iii**

Abstract **iv**

Contents **vi**

List of Figures **ix**

List of Tables **xiv**

Chapter 1 Introduction **1**

1.1 Overview of Transition Metal Dichalcogenides 1

1.2 Overview of TMD FETs 4

1.2.1 TMD Contact Properties with Electrode Materials 7

1.2.2 TMD Complementary Metal–Oxide–Semiconductor FET device . . 8

1.3 Transport Properties Simulation on TMD Materials 10

1.4 Introduction and Applications of Janus TMD Materials 12

Chapter 2 Methodology **14**

2.1 Overview 14

2.2 Structure Building 15

doi:10.6342/NTU202403452

2.3 Density Functional Theory and Related Methods 16
2.3.1 Introduction 16
2.3.2 2D System Dielectric Constant Extraction 19
2.3.3 Spontaneous Polarization Extraction 20
2.3.4 Computational Details 21
2.4 Non-parabolic Band Fitting 23
2.5 Deformation Potential Model 24
2.5.1 Intravalley Scattering 24
2.5.2 Intervalley Scattering 25
2.6 Multi-valley Monte Carlo method 27
2.7 Poisson and Drift-Diffusion Model 28
2.8 Absorption-related Properties Extraction 29
Chapter 3 Properties of Janus MoSSe **31**
3.1 Overview 31
3.2 Band Structures and Related Electronic Characteristics of MoSSe . . 32
3.2.1 Structural Relaxation and Band Structures 32
3.2.2 Spontaneous Polarization 35
3.3 Contact Characteristic of MoSSe 37
3.3.1 MoSSe with Graphene as Contact 37
3.3.2 MoSSe with Metal as Contact 38
3.4 Intrinsic Transport of Mono- and Tri-layered MoSSe 42
3.5 Absorption Properties of Mono-layer MoSSe 47

doi:10.6342/NTU202403452

Chapter 4 MoSSe Complementary Metal-Oxide-Semiconductor Field-Effect Transistor Design and Simulation **54**

4.1 Device Conceptualization and Simulation Parameter 54

4.2 Spontaneous Polarization Effect on Band Diagram 56

4.3 Effect of Gate Design 58

4.4 Effect of Equivalent Oxide Thickness 61

4.5 Effect of Spontaneous Polarization 66

4.6 2D Carrier Distribution 69

Chapter 5 Conclusion **72**

References **74**

doi:10.6342/NTU202403452

List of Figures

1.1 Two common phases seen in 2D $MoTe_2$ material. The 2H-$MoTe_2$ exists as an ambipolar characteristic. 5

1.2 A family of atomically thin TMD materials known for their diverse electrical functionalities. 6

1.3 An experimental example of a CMOSFET inverter device that combines $MoS2_2$ n-FET and TMD α-$MoTe_2$ p-FET horizontally [1]. 9

1.4 An illustration of a model used to comprehend semiconductor carrier transport. 10

1.5 An illustration of a comparison of typical TMD and Janus TMD crystal structures in atomistic configurations. Janus TMDs have an intrinsic out-of-plane dipole due to structural asymmetry. 13

2.1 Flowchart of the device simulation process. JTMD-related inputs of the device simulations are all calculated by the first-principle method. 15

2.2 Diagrammatic representation of the transition from a many-electron system to an electron density. 16

2.3 Flow chart of the self-consistent iterative algorithm in DFT [2]. 17

2.4 Diagrammatic representation of the physics-based interpolation from a course to a dense mesh, where $g_{mn,\nu}(\mathbf{k},\mathbf{q})$ is the e-ph matrix element. . . . 18

2.5 The electron/hole mechanism of intervalley e-ph scattering. Electrons from phonons can be absorbed or emitted, causing scattering between the two valleys. 26

2.6 The process of Monte Carlo simulation. 27

doi:10.6342/NTU202403452

3.1 Schematic of the calculated band diagram of (a) 1L-layer MoSSe, (b) AA' stacking 2L-MoSSe, and (c) AA'A stacking 3L-MoSSe. 33

3.2 (a) The projected band structure of 3L-MoSSe with AA'A stacking is presented. Green, blue, and red dots differentiate the top, middle, and bottom MoSSe layers, respectively. (b) The projected band structure of the 3L-MoSSe is shown from a side view, highlighting the mutual offset in each layer. This offset leads to a P_{sp} throughout the system, depicted by the black arrow. This work has been published in [3]. 34

3.3 The DFT calculated electrostatic potential plot with (a) 1L-MoSSe, (b) 2L-MoSSe, and (c) 3L-MoSSe. The intrinsic dipole field of MoSSe is also calculated. The electron affinity for each system can also be known from the left-hand side vacuum region. 36

3.4 (a) Schematic of the calculated Gr/AA'A-MoSSe/Gr heterostructure. The color scheme for the MoSSe layers corresponds to the previous 3L-MoSSe projected band figure. Gray and black dots represent the contributions from the S/Gr and Se/Gr electrodes, respectively. (b) Projected band structures for the Gr/AA'A-MoSSe/Gr system, revealing a 0.38 eV n-type Schottky barrier contact and a p-type Ohmic contact. (c) Side-view depiction of the layer separation within the Gr/AA'A-MoSSe/Gr system. The intrinsic dipole field (i.e. P_{sp}) induces p-type doping on the Gr electrode attached to the S-face of MoSSe and n-type doping on the Gr electrode attached to the Se-face. This work has been published in [3]. 38

3.5 (a) A computed 2L-MoSSe/metal heterostructure system illustration. Top views of the 2L-MoSSe/Al (111) and 2L-MoSSe/Cu (111) systems are shown in (b) and (c), respectively. 39

doi:10.6342/NTU202403452

3.6 (a) and (c) are the projected band structures with Se-side contact. (b) and (d) are the projected band structures with S-side contact. For all 2L-MoSSe/Al systems, the 2L-MoSSe DOS is given. For reference, the band-edge correspondence diagram showing the connection between the valence band (Ev) and conduction band (Ec), and Fermi level (Ef) is placed on the right side of the picture. The projected band structures and the 2L-MoSSe DOS of the MoSSe Se-side and S-side contact with Cu are shown in (c) and (d), respectively. The metals' contributions are the gray areas. This work has been published in [3]. 41

3.7 Electrons scattering rates of the lowest conduction band in (a)K and (b)Q valleys of 1L-MoSSe calculated at 300 K. Hole scattering rates in (c)Γ and (d)K valleys of 1L-MoSSe calculated at 300 K. The AC and OP denote acoustic and optical phonon; emi and abs denote emission and absorption, respectively. 43

3.8 (a) and (b) Monte Carlo simulated electron and hole mobility of the 1L-MoSSe system. (c) and (d) Monte Carlo simulated electron and hole mobility of the 3L-MoSSe system. 46

3.9 The comparison of DFT calculated JDOS versus photon energy plot with the 1L-MoSSe using a 0.001 eV broadening factor in an (a) $80\times80\times1$, (b) $100\times100\times1$, and (c) $200\times200\times1$ NSCF **k**-mesh calculation. 48

3.10 (a) Schematic of the band linear interpolation process. (b) The comparison between the theory 2D JDOS and the calculation result of different interpolation mesh sampling with a small broadening factor. (c) The 1L-MoSSe absorption coefficient α was calculated using 1000 mesh sampling JDOS. The $\mathbf{E}_p$ is first extracted using interpolated JDOS in the same condition. Then applied to the refined 1000 mesh JDOS to calculate α. . . . 50

3.11 (a) Projected band of 1L-MoSSe with the orbital composition information. (b) Orbital contribution versus Ec-Ev energy difference of the first conduction band in 1L-MoSSe. (c) Orbital contribution versus Ec-Ev energy difference of the last valance band in 1L-MoSSe. 53

doi:10.6342/NTU202403452

4.1 The illustration of 2D MoSSe JTMD CMOSFET device design. This work has been published in [3]. 56
4.2 (a) P-MOSFET and (b) N-MOSFET energy band sectional-view diagrams. The solid and dash lines compare the band diagram with and without P_{sp} from source metal to gate, respectively. This work has been published in [3]. 57
4.3 (a) and (b) Layouts of the key device dimensions and $L_g = 1$ μm structure of single- and double-gate MoSSe MOSFET devices, respectively. (c) Double-gate MoSSe MOSFET layout diagram, where $L_g = 200$ and $L_g = 50$ nm. This work has been published in [3]. 59
4.4 The plots of I_{ds}-V_g for P- and N-MOSFET, respectively, using the designs displayed in Figs. 4.3(a)–(c) for both polarities of the MOSFET, featuring a $t_{ox} = 1$ nm HfO_2 oxide thickness. Parameters are given in Table 4.1. This work has been published in [3]. 60
4.5 Design of a double-gate MoSSe MOSFET with $L_g = 200$ and 50 nm, using several oxides with varying EOT values. 61
4.6 (a) and (b) I_{ds}-V_g plots for $L_g = 200$ nm design of p- and N-MOSFETs, respectively, with different values of EOT. $t_{ox} = 1$ nm for all oxides, and, in addition, results for designs with $t_{ox} = 2$ and 10 nm are also shown for HfO_2. The parameters are given in Table 4.1. This work has been published in [3]. 62
4.7 (a) and (b) I_{ds}-V_g plots for $L_g = 50$ nm design of p- and N-MOSFETs, respectively, with different values of EOT. $t_{ox} = 1$ nm for all oxides, and, in addition, results for designs with $t_{ox} = 2$ and 10 nm are also shown for HfO_2. The parameters are given in Table 4.1. 63
4.8 (a) Lg= 200 nm P-MOSFET with EOT = 0.16 nm and 1.6 nm. The channel horizontal cross-section is shown by the black dash arrow and the 2DHG comparison point A, B, and C are indicated in purple dots. (b) Log scale Hole concentration density in P-MOSFETs channel horizontal cross-section with EOT = 0.16 nm and 1.6 nm. The concentration drop in the source and drain (black arrow) causes the increase in R_c, thus I_{ON} drops. 65

doi:10.6342/NTU202403452

4.9 Diagram MoSSe MOSFET with several chosen JTMDs and oxides with various P_{sp} and EOT numbers, correspondingly. 66
4.10 (a) 2DEG in channel vs linear scale P_{sp} magnitude diagram for N-MOSFETs. (b) Plot of I_{ds}–V_g for N-MOSFET HfO_2 with the $t_{ox} = 10$ nm design device, to comparison with distinct P_{sp}. This work has been published in [3]. 67
4.11 Simulated majority carrier concentration plots for double-gate HfO_2 devices are shown for (a) P-MOSFET under $V_g = -0.5$ V, (b) P-MOSFET under $V_g = 0.5$ V, (c) N-MOSFET under $V_g = 0.5$ V, and (d) N-MOSFET under $V_g = -0.5$ V bias conditions. For observational convenience, the V_{ds} bias is set to zero. This work has been published in [3]. 70
4.12 N-MOSFET 2D majority carrier concentration plots of enhance (HfO_2 $t_{ox} = 1$ nm) mode design (a) without P_{sp} and (b) 4.76×10^{13} cm^{-2} P_{sp} in the channel layer. And N-MOSFET depletion (HfO_2 $t_{ox} = 10$ nm) mode design (c) without P_{sp} and (d) 4.76×10^{13} cm^{-2} P_{sp} in the channel layer. All results are under an equilibrium state to observe the effect of the intrinsic dipole on carrier distribution in the channel. This work has been published in [3]. 71

doi:10.6342/NTU202403452

List of Tables

1.1 Intrinsic carrier mobility at room temperature of TMDs and Janus TMDs from the literature. Mobilities (μ) are all in units of $cm^2V^{-1}s^{-1}$. 12

2.1 First-principle DFT/DFPT simulation input parameters in QE software. . 21

2.2 First-principle e-ph scattering rate simulation input parameters in EPW software. 22

3.1 The DFT calculated lattice constants, band gaps, K−Q valley separations (ΔE_{KQ}), K – Γ valley separations ($\Delta E_{K\Gamma}$ / $\Delta E_{\Gamma K}$), and the effective masses at relevant energy valleys for all MoSSe systems. 32

3.2 The DFT calculated electron affinity, in-plane dielectric constant, out-of-plane dielectric constant, and the spontaneous polarization for all MoSSe systems. d and c are defined Eqn. (2.1) and (2.2). 36

3.3 MoSSe deformation potential constants in the K and Q conduction bands, where D stands for the deformation potential constants. ”ac” is acoustic phonons, and ”op” is optical phonons. The relevant modes’ phonon energies are averaged and shown in the third column [4]. 44

3.4 MoSSe deformation potential constants in the Γ and K valence bands, where D stands for the deformation potential constants. ”ac” is acoustic phonons and ”op” is optical phonons. The relevant modes’ phonon energies are averaged and shown in the third column. 45

3.5 The MoteCarlo simulated low-field mobility, accompanied by valley energy separation, the two valley’s effective masses, and the two valley’s non-parabolic parameter α for all MoSSe systems. 45

doi:10.6342/NTU202403452

3.6 The extracted absorption-related parameters near band edge for the 1L-MoSSe system. 51

4.1 The JTMD MOSFET simulations' input parameters. The MoSSe-related variables are represented by the values in the first section of the table, while the oxide parameters are found in the second section. Using DFT, all MoSSe parameters are derived. In 2D DDCC, the parameters SiO_2 and Al_2O_3 are intrinsically provided. This work has been published in [3]. . . 55

doi:10.6342/NTU202403452

Chapter 1

Introduction

1.1 Overview of Transition Metal Dichalcogenides

Due to their exciting potential, transition metal dichalcogenides (TMDs) have become a focal point of intensive research within the two-dimensional materials field. These materials consist primarily of a transition metal atom bonded to two identical chalcogenide atoms, typically adopting the MX_2 stoichiometry, where M represents a transition metal and X can be S, Se, or Te. While structurally similar to graphene, TMDs exhibit distinct electronic properties. Unlike graphene's semimetallic nature, most TMDs have a band gap, which often undergoes a transition from indirect to direct bandgap when reduced to a monolayer, enabling their bandgap to be tailored for specific optoelectronic applications [5, 6]. Moreover, TMDs exhibit exceptionally high absorption coefficients, particularly in the visible and near-infrared spectral regions, making them highly efficient for optoelectronic applications [7]. The direct bandgap of TMDs also facilitates efficient photon absorption and exciton generation. Nevertheless, the tunable bandgap of TMDs through thickness modulation or external perturbations allows for customizable absorption

doi:10.6342/NTU202403452

spectra, enhancing their utility in photodetectors, solar cells, and other light-harvesting devices [8, 9]. Furthermore, TMDs possess exceptionally high carrier mobility [10–12] and the unique ability to be controlled down to the atomic level [13–15]. These remarkable properties make TMDs promising candidates for the development of various optoelectronic devices.

In addition to the special photoelectric conversion properties of the material itself, its lack of dangling bonds and quantum confinement effects also allow devices to overcome the short-channel effect when developed into small sizes, making TMD materials a good candidate for field effect transistors (FETs) [9, 12, 16, 17]. The unique flexible mechanical properties of TMDs make them promising materials for flexible FETs, and techniques like growing TMDs on elastomeric substrates or encapsulating them in protective layers are being explored to maintain device performance under bending or strain [18], which creates a robust, high-performing electronics that can be integrated into wearable devices and other flexible applications. Another application of TMD-made devices is 2D resistive random access memory (RRAM), where researchers are exploring TMDs that exhibit excellent switching characteristics, enabling ultra-fast write/read speeds and low power consumption [19]. Additionally, studies show promising endurance and retention characteristics, with TMD-based RRAMs demonstrating high write/erase cycles and extended data retention times [20, 21]. Overall, research in this exciting field is focused on capitalizing on the unique advantages of TMDs to develop superior device solutions with enhanced performance, scalability, and potential for novel functionalities.

Several techniques have emerged for TMD synthesis, each offering distinct advantages and limitations. Exfoliation, a method of mechanically separating thin layers from bulk crystals, is a well-established technique for obtaining individual sheets of TMDs [22,

doi:10.6342/NTU202403452

23]. One area of focus is developing methods for achieving controlled thickness during exfoliation. Researchers are exploring techniques like liquid-phase exfoliation with specific solvents or polymers to achieve targeted numbers of TMD layers [22–24]. Additionally, researchers are investigating using shear forces or specific substrates to promote specific exfoliation thicknesses [25]. Another area of research involves increasing the yield of high-quality flakes during exfoliation. This involves minimizing defects introduced during the process and optimizing techniques to separate desired layers without damaging them [26]. However, this approach has limitations for large-scale production. Chemical vapor deposition (CVD) is another popular choice, allowing for precise control over layer thickness and uniformity across large areas. Research efforts focus on achieving films with several key characteristics. One important aspect is the large domain size, where the TMD layer grows as a continuous unit rather than many small crystals. Researchers are exploring ways to manipulate the growth process, such as using specific sapphire substrates [27]. This approach can promote the nucleation and growth of large, single-crystal domains. Another area of research involves achieving uniformity across the entire film. Techniques like proximity precursor supply are being investigated to ensure consistent material properties throughout the large area [28]. Overcoming challenges like grain boundaries is crucial for integrating these CVD-grown TMDs into future electronic devices. A recent study by Yonggang Zuo demonstrates the successful growth of high-quality TMDs in wafer scale using an active chalcogen monomer supply method, highlighting the importance of optimizing precursor delivery for controlled growth [29]. Molecular beam epitaxy (MBE) provides atomic-level control but requires expensive equipment and high-vacuum environments [30, 31]. As research progresses, further refinement of existing methods and exploration of novel techniques will be crucial for realizing the full potential

doi:10.6342/NTU202403452

of TMDs in next-generation devices.

1.2 Overview of TMD FETs

The exploration of TMD FETs began in the early 2010s, fueled by the discovery of their semiconducting properties in the monolayer form [10, 32]. Early research focused on n-type TMD FETs, with molybdenum disulfide (MoS_2) emerging as a prominent example due to its good air stability and ease of fabrication. MoS_2 FETs have demonstrated high on/off ratios (>10^8) and subthreshold swing values (< 75 mV/dec), indicating their potential for low-power logic devices [12, 17]. Another promising n-type TMD candidate is tungsten disulfide (WS_2), which exhibits even higher carrier mobility compared to MoS_2, making it attractive for high-frequency applications [16]. The development of p-type TMD FETs has been more challenging, but significant progress has been made. Gallium Selenide (GaSe) [33] and tungsten ditelluride (WTe_2) [34] are two notable examples, exhibiting good hole mobility and potential for complementary logic circuits alongside n-type TMD FETs. Additionally, research on these TMD FETs has shown promising results for achieving p-type behavior.

Beyond n-type and p-type functionalities, some TMDs exhibit ambipolar behavior, where the material can conduct both electrons and holes depending on the gate voltage. This makes them attractive for logic devices with simpler transistor configurations. 2H-Molybdenum ditelluride, often called α-$MoTe_2$, is a well-studied example of an ambipolar TMD, demonstrating good performance in both electron and hole accumulation regimes [1]. The 2H phase in $MoTe_2$ stands for the hexagonal structure, and often a 2H to 1T' phase transition would occur as both temperature and Te composition rise, chang-

doi:10.6342/NTU202403452

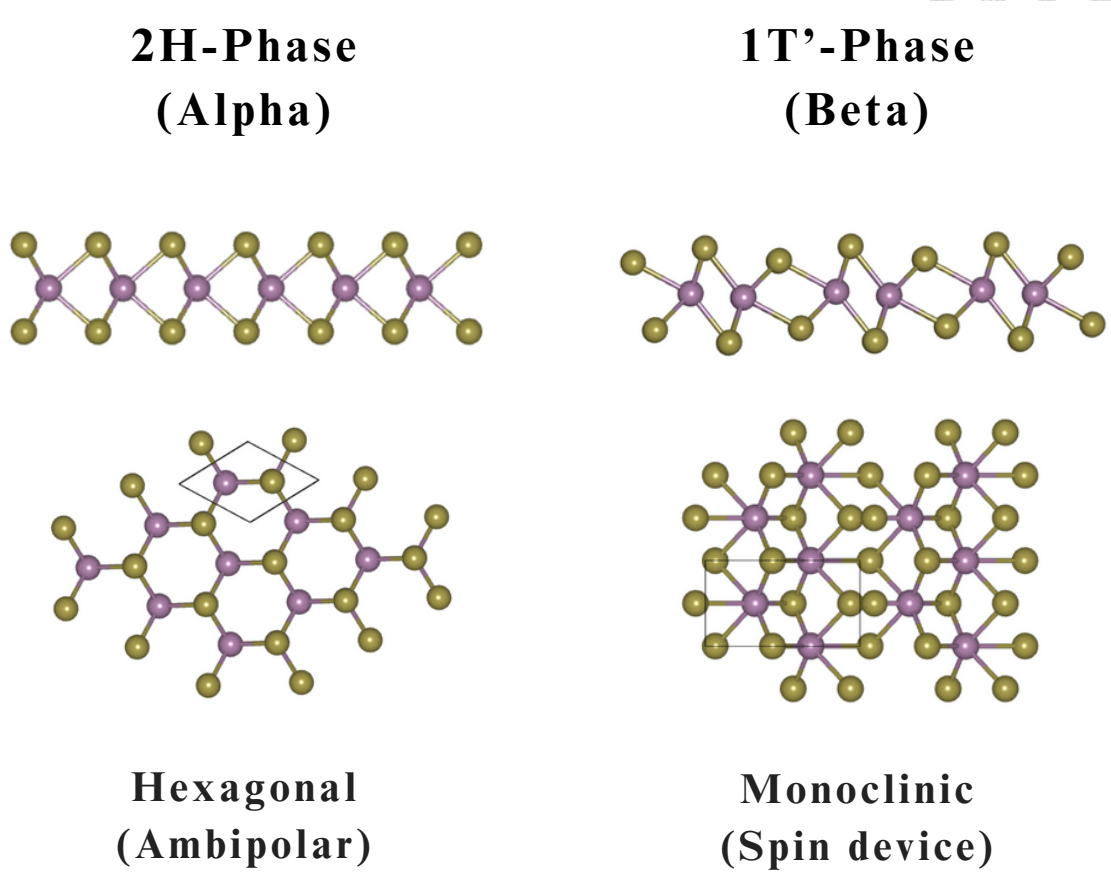

Figure 1.1: Two common phases seen in 2D $MoTe_2$ material. The 2H-$MoTe_2$ exists as an ambipolar characteristic.

ing the structure into a monoclinic phase, namely β-$MoTe_2$ [35]. Other ambipolar TMD candidates include niobium diselenide and zirconium dichalcogenides, which had been carried out in experimental studies [17].

Although TMDs have enormous potential for FETs, there are obstacles in their preparation processes. Reducing the flaws and impurities that are introduced during procedures like exfoliation and CVD is a major problem. Performance and reliability of the FET are greatly reduced [36] as a result of these defects. Furthermore, it is still difficult to achieve consistent characteristics among large-scale TMD films. The overall performance and integration of devices can be affected by discrepancies in thickness, crystal orientation, and defect density [37]. Another issue is scalability. broad-scale device manufactur-

doi:10.6342/NTU202403452

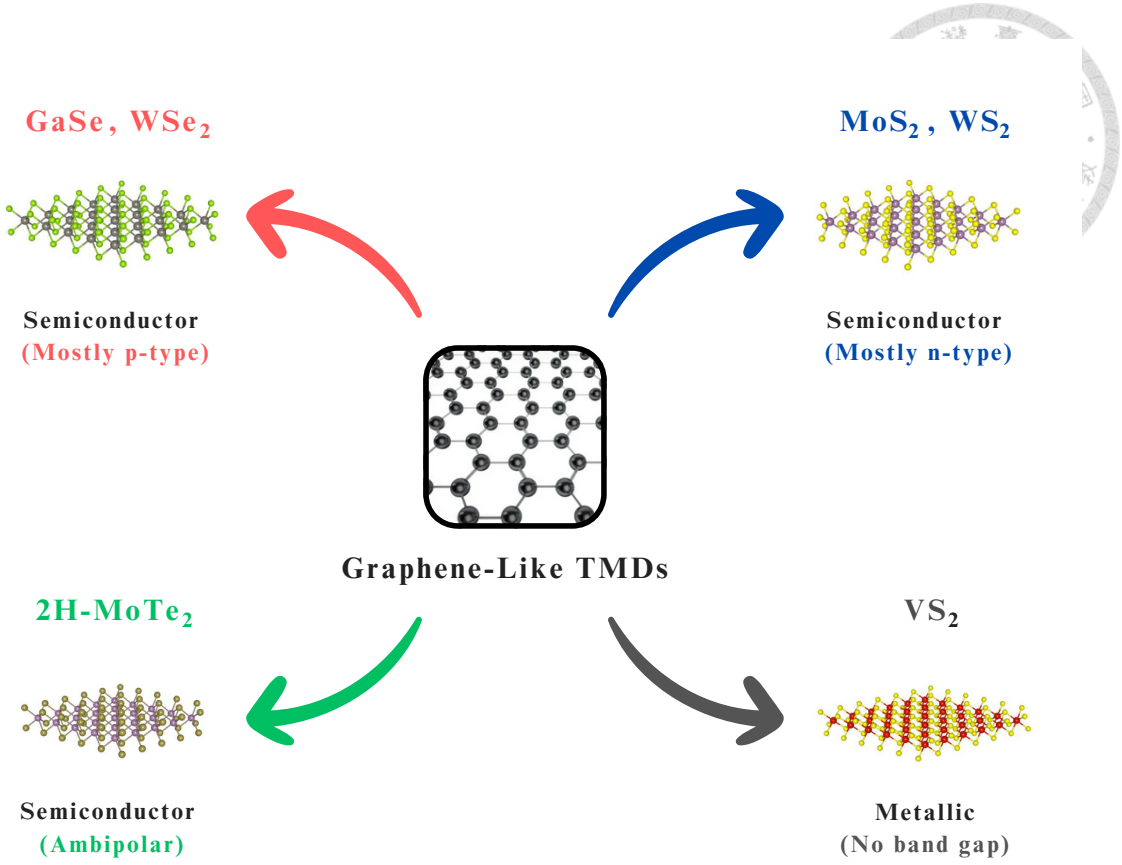

Figure 1.2: A family of atomically thin TMD materials known for their diverse electrical functionalities.

ing is limited by the difficulty of obtaining high-quality, single-crystal TMD films across broad substrates, although CVD provides a route for large-area growth [38]. However, to combine TMDs with other device components in an FET, transfer procedures are frequently needed, which can lead to damage and alignment problems. The fragile TMD flakes may get ripped, cracked, or wrinkled during the transfer procedure. Furthermore, it may transfer impurities onto the TMD surface, hence deteriorating the device's performance and electrical characteristics [39]. On the other hand [40], misalignment may result in inadequate electrical contact and decreased device performance. Lastly, high temperatures are needed for various preparation techniques, especially CVD, which may interfere with some device fabrication procedures and restrict the range of suitable substrates [41]. Notwithstanding these drawbacks, there are still difficulties in reaching high current densi-

doi:10.6342/NTU202403452

ties and resolving contact resistance problems in FET design and material selection [38]. Therefore, for the ongoing development of high-performance TMD FETs, research on novel growth processes, interface engineering, doping techniques, transfer methods, and device scaling is essential.

1.2.1 TMD Contact Properties with Electrode Materials

A FET device's I–V characteristics and performance are known to be significantly impacted by its contact characteristics. To maintain a linear I–V curve and improve the electrical performance of FETs, low contact resistance typically necessitates Ohmic connections at the semiconductor-metal interface [42, 43]. For the common 2D material electrode graphene, researchers indicated that graphene's excellent conductivity comes into play, which can significantly reduce contact resistance in MoS_2 devices compared to metal. This translates to improved performance in TMD field-effect transistors, with higher currents and better mobility [44, 45]. The ability to tune graphene's work function allows for engineering the interface with TMDs, optimizing performance in FET devices [46]. For metal, regretfully, most TMD/metal contacts typically result in the formation of Schottky barriers (SBs) [42, 43, 47–49]. For a FET with SB contacts to work, carriers need to get beyond the energy barrier that prevents them from moving from metal into the TMD channel region, which lowers the injection efficiency [50]. Furthermore, TMD material's interracial connection with metal is difficult due to the lack of dangling bonds on the surface of a 2D material, which increases contact resistance as well [42]. Substitutional doping is a generic method [51] utilized in contemporary semiconductor technology to lower contact resistance. Substitutional doping emerges as a powerful tool to tackle contact resistance, a major hurdle in TMD-based devices. Studies show dop-

doi:10.6342/NTU202403452

ing MoS_2 with group V elements like niobium (Nb) or titanium (Ti) significantly reduces resistance by creating more charge carriers near the contact to improve contact characteristics [52–54].

Since such a doping procedure will significantly change the properties of 2D materials, which often cause negative effects [55], there are better ways to minimize contact resistance. The majority of the work involved in engineering TMD/metal contacts is related to selecting an appropriate metal to modify the work function. A metal with a high work function is typically chosen for p-FETs, while a smaller work function is required for n-FETs. Numerous investigations have discovered that TMD/metal heterostructures such as MoS_2/Cu, WSe_2/Ti, and WS_2/Cu may offer n-type SB contacts [47, 48], and p-type SB contacts can be established with certain combinations such as WSe_2/Au and WSe_2/Pd [47, 56]. But TMD-based FET contact design becomes more difficult since only a particular TMD/metal combination is allowed for Ohmic contact formation [57]. Making the FET devices achieve Ohmic contact using a TMD material without further treatment is nearly impossible.

1.2.2 TMD Complementary Metal–Oxide–Semiconductor FET device

In contemporary electronics, complementary metal-oxide-semiconductor field-effect transistors (CMOSFETs) are the mainstays. The basic components of integrated circuits (ICs), which are included in practically everything electronic, including computers, cellphones, and calculators, are these tiny switches that turn electrical signals on and off. Engineers can create complex logic gates and other functionalities that power modern electronic devices by combining n-type and p-type FETs into CMOSFETs in complex cir-

doi:10.6342/NTU202403452

cuits. They are perfect for creating efficient and high-density integrated circuits due to their small size, low power consumption, and fast switching speed [58].

One common approach to achieving CMOSFETs with TMDs involves horizontally combining two different TMD channels on a single substrate. This approach leverages the unique properties of specific n-type and p-type TMD materials, similar to how traditional silicon CMOSFETs function [59–62]. However, this design presents some fabrication challenges. Firstly, the process of transferring two different TMD materials onto a single substrate can be delicate. There's a risk of introducing defects or contamination during the transfer process, which can significantly impact device performance and reliability [39, 63]. Secondly, using two different TMD materials necessitates the use of separate contact metals for each channel. This increases the processing complexity and translates to a longer and more time-consuming fabrication procedure.

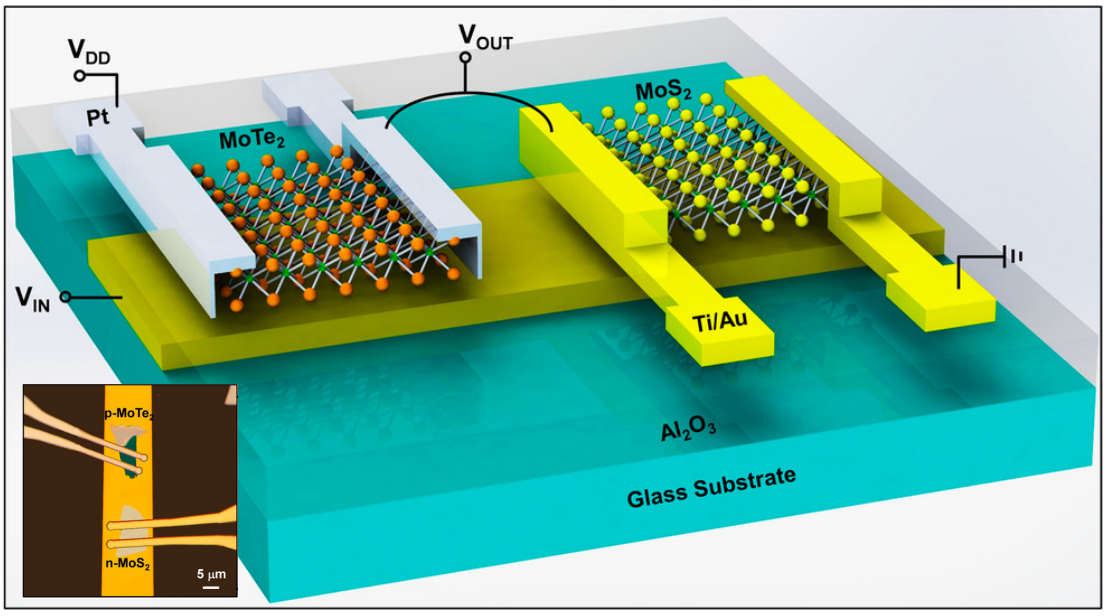

Figure 1.3: An experimental example of a CMOSFET inverter device that combines $MoS2_2$ n-FET and TMD α-$MoTe_2$ p-FET horizontally [1].

To address these fabrication obstacles, researchers have explored the use of ambipolar TMDs, which are TMD materials that can exhibit both n-type and p-type behavior

doi:10.6342/NTU202403452

depending on various factors like doping or gate voltage. Materials like $MoTe_2$ [64] and $ReSe_2$ [64] have shown promise as single-channel CMOSFET materials. This approach eliminates the need for complex multi-material transfer processes and separate contact metals, simplifying fabrication and potentially paving the way for more efficient and scalable TMD-based CMOSFET production.

1.3 Transport Properties Simulation on TMD Materials

Just like the material's transport properties, mobility also significantly impacts a FET's performance. Higher mobility translates to better current density and faster switching speeds. While current limitations in TMD fabrication, such as grain boundaries and defects, hinder mobility in real-world devices, simulations can predict the optimal mobility achievable with future advancements. This allows researchers to envision the upper-performance limits of TMD-based FETs.

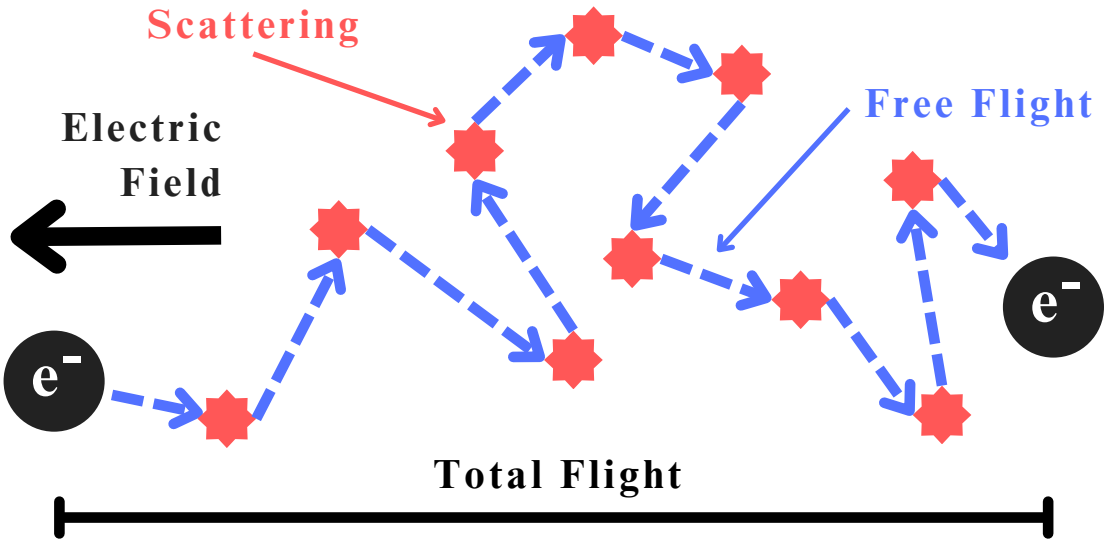

Figure 1.4: An illustration of a model used to comprehend semiconductor carrier transport.

The Boltzmann transport equation (BTE) and Monte Carlo method are the two common approaches that are frequently implemented in theoretical transport studies. To repre-

doi:10.6342/NTU202403452

sent the transport phenomena, the BTE used a distribution function under an external perturbation in terms of the Fermi-Dirac function. We can infer all of the transport parameters from the distribution, which would show us how electrons are spread in the k-space. The distribution function will stabilize after taking scattering, applied fields, and carrier diffusion into account through an iterative approach or writing into a balanced equation form. Transport characteristics under an electric field, such as conductivity and mobility, may then be computed by using the relaxation time approximation. However, another effective technique for modeling electron transport turns out to be the Monte Carlo approach. To reflect the possibility of various interaction scenarios, the procedure starts with specifying the precise scattering processes in mathematical equations that are then put into probability distributions. Next, a large number of simulated electron scattering events are generated by the Monte Carlo approach using random number generators. Based on the stated distributions, the model determines the likelihood of different scattering events (such as collisions with phonons or impurities) for each route. Following each scattering event, the energy and direction of the electron are then updated to simulate its motion through the medium, similar to the carrier transport behavior in a material. As a result, characteristics like conductivity and mobility are achieved [65]. Numerous studies have estimated the top bound of intrinsic transport in various TMDs by calculating the high-field peak velocities and low-field mobility using the two previously described approaches [4, 66], where the comparison with experimental value is also given in Table 1.1. The huge difference between the simulated and experimental values indicates that significant advancements are needed in TMD fabrication processes to realize the full potential of TMD devices.

doi:10.6342/NTU202403452

Table 1.1: Intrinsic carrier mobility at room temperature of TMDs and Janus TMDs from the literature. Mobilities (μ) are all in units of $cm^2V^{-1}s^{-1}$.

TMD Material	Simulated μ_e	Experimental μ_e	Simulated μ_h	Experimental μ_h
MoS_2	181 [4]	30 [67]	270 [66]	8.5(Doped)[53]
$MoSe_2$	150 [4]	50 [68]	90 [66]	0.023 [69]
MoSSe	157 [4]	-	-	-
WS_2	382 [4]	33 [67]	540 [66]	18.84 [70]
WSe_2	264 [4]	140(Flake) [68]	270 [66]	110 [71]
WSSe	238 [4]	-	-	-

1.4 Introduction and Applications of Janus TMD Materials

Different from the MX_2 composition, Janus transition metal dichalcogenides (JTMDs) exist in MXY stoichiometry, where M = transition metal and X, Y = S, Se, or Te, with X $\neq$ Y, might be an additional approach to creating a CMOSFET from a single material. Several JTMDs have been successfully synthesized in recent years using various methods. Lin *et al.* [72] prepared Janus WSSe by pulsed laser deposition, while monolayer MoSSe was synthesized using chemical vapor deposition combined with plasma stripping [73] or an atomic replacement process [74]. Previous theoretical studies of these JTMDs have confirmed their manufacturing stability, which unequivocally demonstrates that their phonon spectra are stable and free of imaginary frequencies [75, 76]. In contrast to TMDs, JTMDs feature two distinct chalcogen-atom layers that combine to form an asymmetric sandwich shape that generates an electric field vertical to the horizontal atomic plane. Due to the dipole-like property of this out-of-plane field, it may find use in gas sensing devices, catalysts, as well as piezoelectric, and electronic spinning devices [77–79].

Nevertheless, simulation research has demonstrated that when different sides are attached to graphene, this intrinsic dipole feature of JTMDs can allow the formation of both

doi:10.6342/NTU202403452

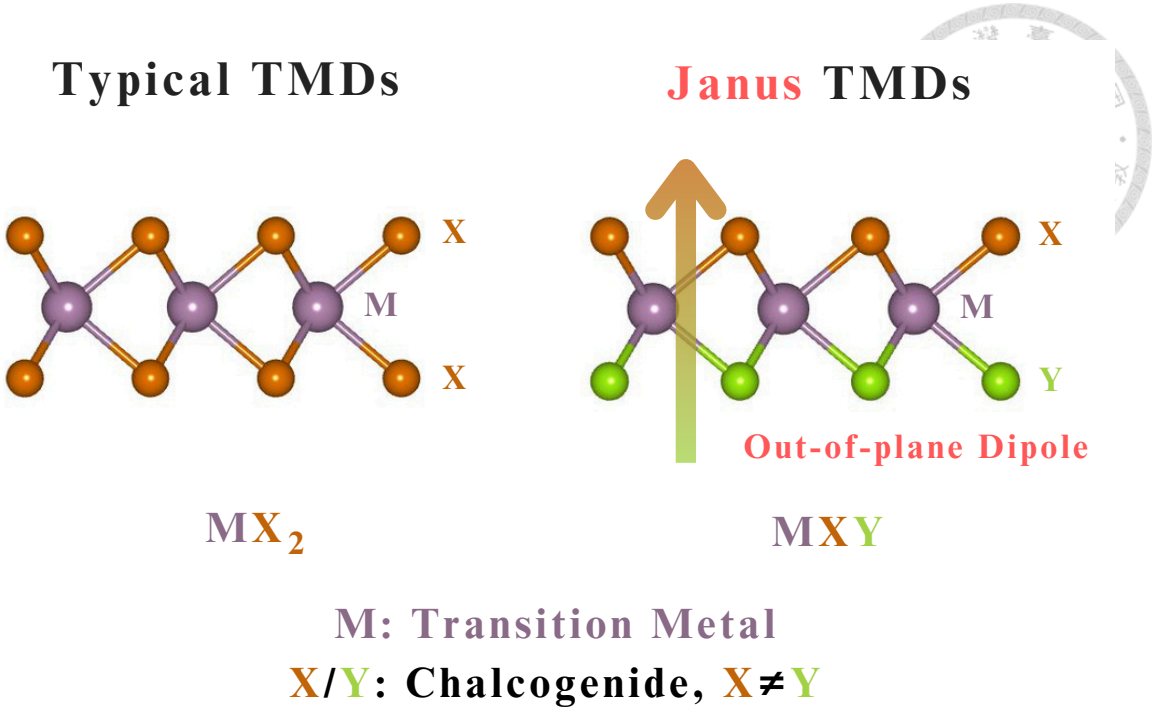

Figure 1.5: An illustration of a comparison of typical TMD and Janus TMD crystal structures in atomistic configurations. Janus TMDs have an intrinsic out-of-plane dipole due to structural asymmetry.

n- and p-type contacts concurrently without the need for extra doping [80–82]. This can be implemented in the construction of pin-diode[81] or photovoltaic[82] devices. Furthermore, theoretical research has demonstrated that the intrinsic dipole present in JTMD MoSSe linked to metals could significantly diminish the SB upon contact [57]. Under some circumstances, the aforementioned JTMD/electrode contact devices may even achieve Ohmic contact[57, 80]. Nevertheless, the utilization of n- and p-type Ohmic contacts' advantages in FET applications has not yet been investigated, in contrast to optoelectronic devices. Moreover, little research has been done on using this intrinsic dipole feature to create doping-free FETs or CMOSFETs. Therefore, looking at the possible application of JTMD on CMOSFET is crucial and necessary. Part of this work has been published in [3].

doi:10.6342/NTU202403452

Chapter 2

Methodology

2.1 Overview

This chapter details the methodological framework employed to calculate and analyze the electronic and contact properties of layered MoSSe, ultimately investigating its device behavior in CMOSFETs. We use a variety of computational techniques, such as density functional theory (DFT), density functional perturbation theory (DFPT), electron-phonon Wannierization (EPW), non-parabolic band fitting, the multi-valley Monte Carlo method, and the Poisson–Drift–Diffusion iterative solver. Figure 2.1 shows a detailed flowchart that illustrates the simulation procedure from start to finish. The mobility extraction procedure (Blue-dash box in Figure 2.1) of the TMD materials which utilized the first-principle and Monte Carlo combination method was published by Pai [4], those interested can find more information in his paper. The basic principles of the computational techniques are given in the following sections, where the computational details for each calculation method are also given as a reference.

doi:10.6342/NTU202403452

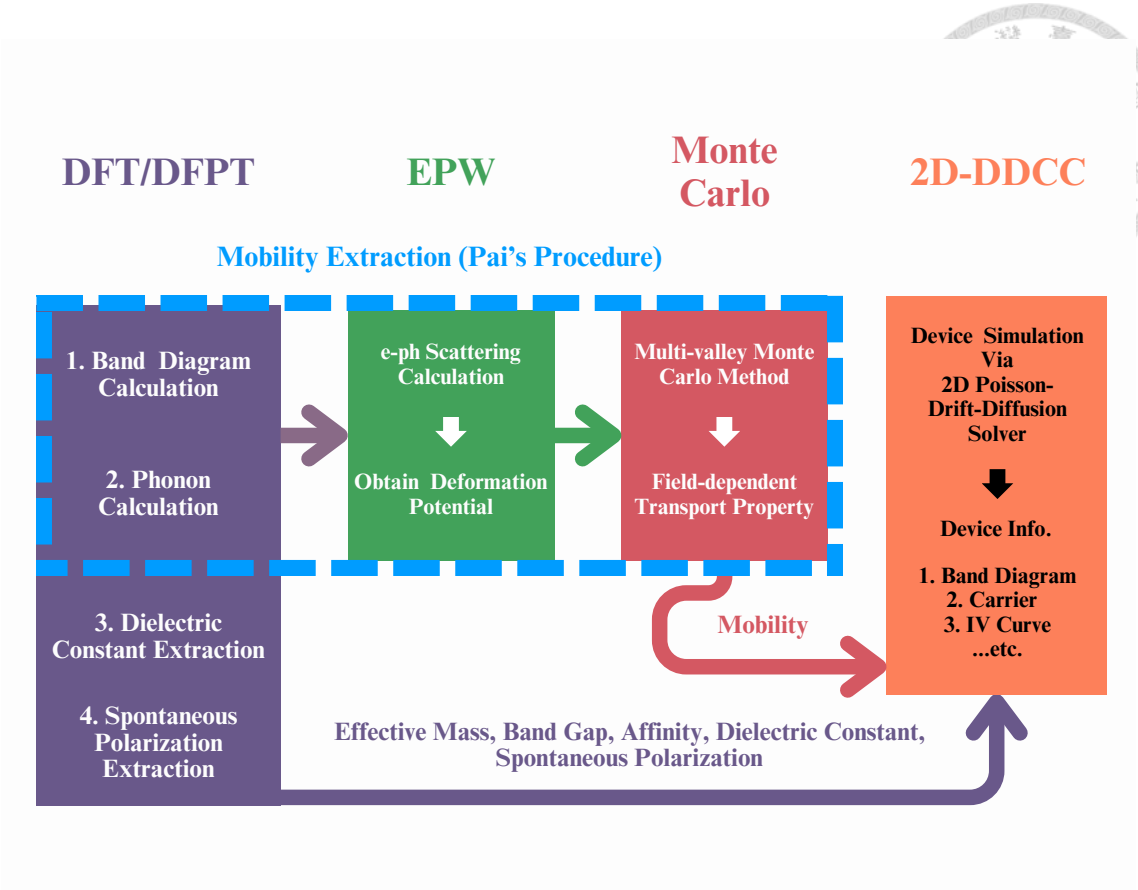

Figure 2.1: Flowchart of the device simulation process. JTMD-related inputs of the device simulations are all calculated by the first-principle method.

2.2 Structure Building

The atomic structure buildings and visualization of the layered JTMD and MoSSe contact in this work are all produced by VESTA, which is a powerful and versatile tool for researchers and students who need to visualize and analyze 3D structures [83]. We specify our contact structure building here since it is somewhat complicated. To achieve MoSSe contact structure, we affix a $\sqrt{7} \times \sqrt{7} \times 1$ supercell of Graphene to a $2 \times 2 \times 1$ MoSSe supercell for contact simulation. Six layers of (111) Al in a $2 \times 2 \times 1$ supercell are connected to a $\sqrt{3} \times \sqrt{3} \times 1$ MoSSe supercell, whereas six layers of (111) Cu in a $\sqrt{7} \times \sqrt{7} \times 1$ supercell is connected to a $2 \times 2 \times 1$ MoSSe supercell. The bulk feature of the metal is guaranteed by the six layers of metal slabs. Below 5%, all lattice incompatibilities

doi:10.6342/NTU202403452

are managed and an energetically favorable surface simulation model is developed for each metal [84]. The vacuum is set to 15-20 Å for all systems to avoid interactions between neighboring supercells.

2.3 Density Functional Theory and Related Methods

2.3.1 Introduction

To know the solid's characteristics, solving the time-independent Schrödinger equation with a high number of electrons, which is a many-body problem, is necessary. However, even a basic two-electron system is already quite hard to acquire an analytical solution through the Schrödinger equation, let alone solid materials. The problem creates difficulties for researchers to directly apply simulation approaches to solid material research and analysis in the past.

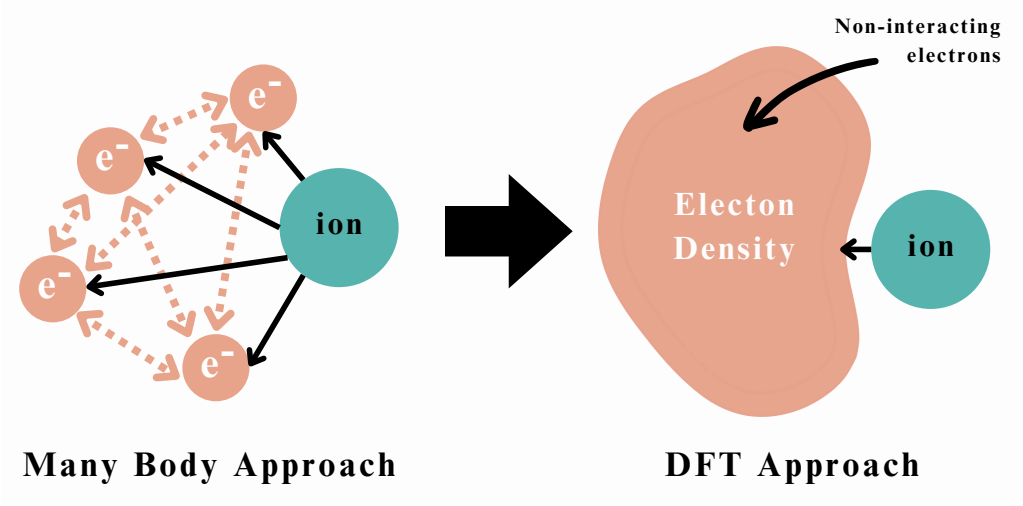

Figure 2.2: Diagrammatic representation of the transition from a many-electron system to an electron density.

Density Functional Theory (DFT), introduced recently, is now the basis for first-principles simulations due to the reasonable balance between calculating efficiency and ac-

doi:10.6342/NTU202403452

curacy. This theory reduces complex many-body problems to the motion of non-interacting electrons in an effective way. For instance, consider a system with N electrons. The classic many-body approach requires 3N coordinates parameters; however, DFT requires just 3 coordinates, regardless of the number of electrons in the system. Stated differently, the electron density is reduced to a simpler computational entity. The wave functions in terms of electron density can be obtained iteratively by solving two sets of equations: the Kohn–Sham equations (Simplified Schrödinger equation) and the Effective Potential equation. As the electron densities are known, any electron-related ground state properties, such as electronic distribution, band diagram, density of states (DOS), and electrostatic potential, can be calculated [2].

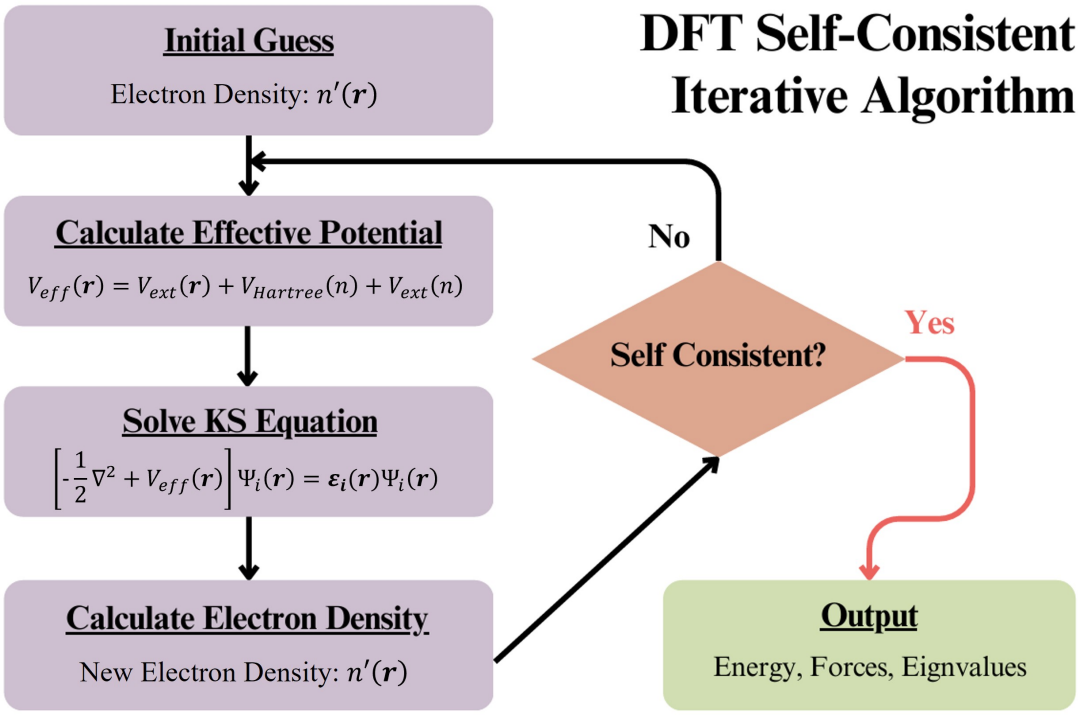

Figure 2.3: Flow chart of the self-consistent iterative algorithm in DFT [2].

Given that intrinsic carrier transport is primarily constrained by phonon-related scattering at room temperature, gaining insights into how carriers interact with phonons becomes crucial for resolving transport behavior from a theoretical standpoint. The electron-

doi:10.6342/NTU202403452

phonon (e-ph) interaction plays a significant role, involving the phonons generated by lattice dynamics and the electrons. Researchers commonly integrate DFT with other techniques or employ advanced variants to tackle specific challenges in simulation. For example, phonon frequencies, dielectric constants, and phonon dynamical matrix are computed by combining DFT with perturbation theory, known as Density Functional Perturbation Theory (DFPT). By examining how the system's electrical structure responds to minor perturbations, DFPT expands on DFT. With DFPT, we can compute several physical parameters by examining the perturbation-caused reaction [2].

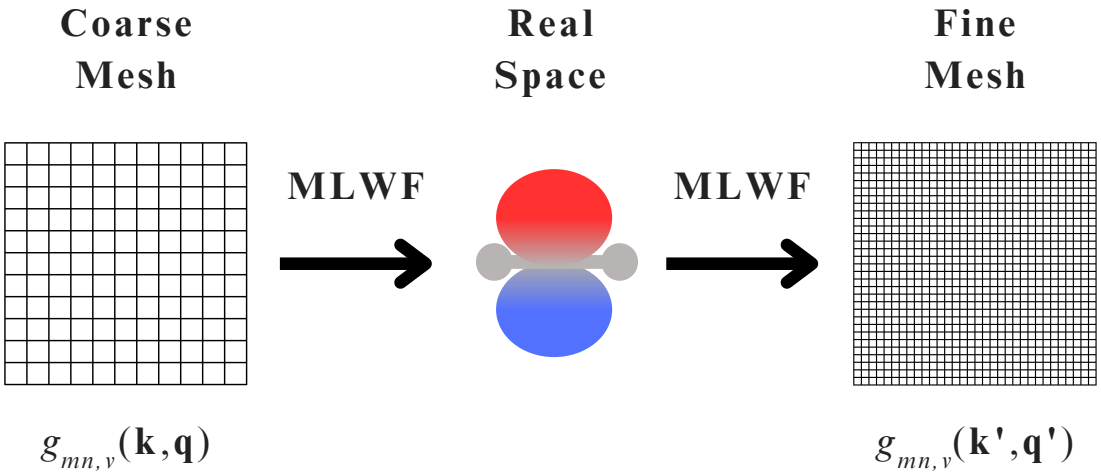

Figure 2.4: Diagrammatic representation of the physics-based interpolation from a course to a dense mesh, where $g_{mn,\nu}(\mathbf{k},\mathbf{q})$ is the e-ph matrix element.

Common material characteristics like resistivity, thermoelectricity, and superconductivity, among others, are intimately linked to how electrons and lattice vibrations interact. As comprehensive data on electron and phonon properties is available, interpolation can be performed using maximally localized Wannier functions (MLWFs), allowing us to leverage the spatial localization of e-ph matrix elements in the Wannier representation on highly dense momentum grids. Though localized, MLWF offers an appealing alternative to convey the same information as the Bloch functions when depicting the space occupied by a Bloch band in a crystal. This localized representation lowers computational costs by

doi:10.6342/NTU202403452

enabling accurate band structure interpolation in reciprocal space, enabling precise computation of derived features, including optical properties, transport, and e-ph coupling calculation [85]. Subsequently, computing acoustic- and optical-phonon scattering rates becomes feasible through Fermi's golden rule, given the availability of known e-ph matrix elements.

Quantum ESPRESSO[86] is used to do the DFT/DFPT computations while the Electron-Phonon Wannier (EPW) program [87] is in charge of electron-phonon-related computations. Both software are free and open-source computational tools widely employed in first-principles calculations across diverse research fields.

2.3.2 2D System Dielectric Constant Extraction

The inclusion of the vacuum layer across the z-axis presents a challenge when seeking to calculate the in-plane dielectric constant ($\epsilon_{\parallel}$) and out-of-plane dielectric constant ($\epsilon_{\perp}$) using DFT in 2D material systems. In DFT calculations, the necessity of including a vacuum layer to prevent interactions between periodic images introduces an artifact, leading to discrepancies between the calculated macroscopic dielectric constant and the actual value for thin-layered TMDs. Akash Laturia et al. proposed a method utilizing the principle of the equivalent capacitance method [88] to distill the dielectric constants by eliminating the contribution of the vacuum layer. After applying the equivalent capacitance method in series on 2D material systems, the $\epsilon_{2D,\parallel}$ and $\epsilon_{2D,\perp}$ can be written as:

$$\epsilon_{2D,\parallel} = [1 + \frac{c}{d}(\epsilon_{All,\parallel} - 1)\,], \tag{2.1}$$

doi:10.6342/NTU202403452

$$\epsilon_{2D,\perp} = [1 + \frac{c}{d}(\frac{1}{\epsilon_{All,\perp}} - 1)]^{-1}. \tag{2.2}$$

In Eq. (2.1) and Eq. (2.2), $\epsilon_{All,\parallel}$ and $\epsilon_{All,\perp}$ indicate the whole simulated system's in-plane and out-of-plane dielectric constants, c is the thickness of the simulated cell containing the 2D material, and d is the layer-to-layer thickness from transition metal to transition metal. A common approach to determine the parameter d for an N-layer TMD system involves calculating the DFT relaxed structure of an (N+1)-layer system using DFT. The average value of d obtained from the (N+1)-layer system is then used for the N-layer system. This method is pretty sensitive to layer thickness which sometimes causes unreasonable dielectric constants. Thus, relaxation conditions have to be set strictly and carefully to prevent incorrect results.

2.3.3 Spontaneous Polarization Extraction

Spontaneous polarization (P_{sp}) is an intriguing phenomenon that may happen in the microscopic realm of materials where their average balance of positive and negative electrical charges are not exactly equal. The fundamental feature of P_{sp} is this internal separation of charge because of their electrical and crystallographic characteristics, which occurs in the appearance of structural asymmetry. Materials like GaN, AlN, $BaTiO_3$, and JTMDs exhibit this property. In the device simulations, this dipole effect is represented by a P_{sp} term, as seen by the vertical arrow in Fig. 1.5. The P_{sp} term can be expressed as a combination of the internal electric field E and the out-of-plane dielectric constant $\epsilon_{2D,\perp}$:

$$P_{\text{sp}} = \epsilon_{2D,\perp} E. \tag{2.3}$$

doi:10.6342/NTU202403452

The $\epsilon_{2D,\perp}$ can be calculated using the method described in the previous section. The E is then determined based on the JTMD thickness and the difference in electron affinity between the two outermost layers.

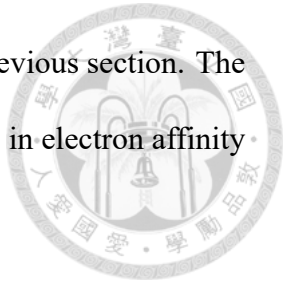

2.3.4 Computational Details

Table 2.1: First-principle DFT/DFPT simulation input parameters in QE software.

Executed Program	Parameters	Input Value
pw.x	forc_conv_thr	10^{-4} Ry
	etot_conv_thr	10^{-6} Ry
	conv_thr	10^{-8} (MoSSe) / 10^{-7} (Hetero) Ry
	ecutwfc	50 (MoSSe) / 40 (Hetero) Ry
	ecutrho	ecutwfc×8
	mixing_beta	0.7 (MoSSe) / 0.5 (Hetero)
	k-point mesh	18×18×1 (MoSSe) / 8×8×1 (Hetero)
	tefield	TRUE
	dip_field	TRUE
	eamp	0
	edir	3
	emaxpos	0.95
	eopreg	0.05
ph.x	tr2_ph	10^{-14} Ry
	alpha_mix(i)	0.7
	q-point mesh	6×6×1

Quantum ESPRESSO is used for all DFT/DFPT-related computations. The generalized gradient approximation (GGA) of the norm-conserving Vanderbilt[89] pseudopotentials and Perdew – Burke – Ernzerhof (PBE) exchange-correlation functional is combined with DFT-D3 van der Waals correction[90]. For all computations, the Monkhorst-Pack k sampling is employed. The geometry is revised until the maximal residual forces are smaller than 0.015 eV/Å. Currently, dipole correction (tefield, dip_field, eamp, edir, emaxpos, and eopreg are all dipole-correction-related parameters) is applied to all MoSSe structures to counteract the artificial electric field that arises from their asymmetric topologies. For MoSSe hetero-structures, Marzari-Vanderbilt smearing with 0.01 Ry degauss is

doi:10.6342/NTU202403452

applied due to the metal material in the system. Table 2.1 provides the in-depth specifications.

Table 2.2: First-principle e-ph scattering rate simulation input parameters in EPW software.

Executed Program	Parameters	Input Value
epw.x	lifc	TRUE
	asr_typ	'crystal'
	efermi_read	TRUE
	fsthick	6.0 eV
	temps	300 K
	degaussw	0.001
	nk mesh	30×30×1
	nq mesh	6×6×1
	nqf mesh	800×800×1
	elecselfen	TRUE
	phonselfen	FALSE
	a2f	FALSE
	system_2d	TRUE

EPW handles the e-ph interaction calculation on an ultra-dense mesh to assess the e-ph matrix elements between electronic states and phonon wave vectors. This requires using MLWF interpolation to evaluate the Brillouin zone integral for each phonon wave vector. In our study, an 800×800×1 fine q-point mesh is used to evaluate the matrix element. The e-ph matrix element $g_{mn,\nu}$ (Eq. (2.4)), electron self-energy $\Sigma^{\mathrm{e-ph}}_{n\boldsymbol{k}}$ (Eq. (2.5)), and the e-ph scattering rate in terms of relaxation time $\tau_{n\mathbf{k}}$ (Eq. (2.6)) are given as follows:

$$g_{mn,\nu}(\mathbf{k},\mathbf{q}) = \frac{1}{\sqrt{2\omega_{\mathbf{q}\nu}}} \langle \psi_{m,\boldsymbol{k}+\boldsymbol{q}} | \partial_{\boldsymbol{q}\nu} V | \psi_{n,\boldsymbol{k}} \rangle \,, \tag{2.4}$$

$$\begin{aligned} \Sigma^{\mathrm{e-ph}}_{n\boldsymbol{k}} = \sum_{m,\mathbf{q}\nu} \int_{BZ} \frac{d\mathbf{q}}{\Omega_{BZ}} |g_{mn,\nu}|^2 \times \Bigg[& \frac{n(\omega_{\mathbf{q}\nu}) + f(\epsilon_{m\mathbf{k}+\mathbf{q}})}{\epsilon_{n\mathbf{k}} - \epsilon_{m\mathbf{k}+\mathbf{q}} + \omega_{\mathbf{q}\nu} + i\delta} \\ & + \frac{n(\omega_{\mathbf{q}\nu}) + 1 - f(\epsilon_{m\mathbf{k}+\mathbf{q}})}{\epsilon_{n\mathbf{k}} - \epsilon_{m\mathbf{k}+\mathbf{q}} - \omega_{\mathbf{q}\nu} + i\delta} \Bigg] , \end{aligned} \tag{2.5}$$

doi:10.6342/NTU202403452

$$\frac{1}{\tau_{n\mathbf{k}}} = \frac{2}{\hbar}\mathrm{Im}(\Sigma^{\mathrm{e-ph}}_{n\boldsymbol{k}}). \tag{2.6}$$

The electron wave function is denoted by ψ, the phonon of wave vector $\mathbf{q}$, branch index ν, and frequency $\omega_{\mathbf{q}\nu}$ is represented by $\epsilon_{n\mathbf{k}}$, the phonon energy in the phonon branch ν and state $\mathbf{q}$ by $\omega_{\mathbf{q}\nu}$, the Bose occupation factors are represented by $n(\omega_{\mathbf{q}\nu})$, and δ is a real positive infinitesimal parameter that ensures the correct mathematical formalization of the self-energies and prevents numerical issues. The Brillouin Zone (BZ) of volume Ω_{BZ} is covered by the integrals. In-depth specifications are provided in Table 2.2.

2.4 Non-parabolic Band Fitting

In this study, the materials possess a multi-valley band structure with energy variations between the valleys. This characteristic leads to significant electron scattering via both intravalley and intervalley phonon interactions, which are crucial for electron transport behavior under various electric fields. To address this complexity, a multi-valley model is employed. This model simplifies the transport across the entire Brillouin zone by focusing on the two lowest valley types that dominate the transport properties. Following density DFT calculations, we utilize a non-parabolic effective mass approximation to perform material parameter fitting:

$$E(1+\alpha E) = \frac{\hbar^2\mathbf{k}^2}{2m^*}. \tag{2.7}$$

Using m^* as the effective mass to represent the low energy band and the non-parabolicity coefficient α to describe the isotropic nature in the high energy region, the Eq. (2.7) could

doi:10.6342/NTU202403452

be extended into a two-dimensional specification:

$$E(1+\alpha E) = \frac{\hbar^2 k_x^2}{2m_x^*} + \frac{\hbar^2 k_y^2}{2m_y^*}. \tag{2.8}$$

The k_x and k_y present the difference in different transport directions if the valley in the two directions is anisotropic.

2.5 Deformation Potential Model

2.5.1 Intravalley Scattering

Unlike a perfect picture, real crystals have constantly vibrating atoms. These vibrations strain the crystal, affecting electron behavior and creating strain energy. Phonons, acting like particles, capture this effect. Collisions between electrons and phonons are a result of these vibrations, which is the concept of previous e-ph interaction. Two main phonon types exist: acoustic (atoms move in identical directions) and optical (atoms vibrate against each other). The acoustic phonon scattering rate, after using the perturbation potential representation, can be described by [91]:

$$W_{ac}(k) = \frac{\pi k_B T D_{ac}^2}{\hbar \rho v_{ac}^2} N_{2D}(E_k), \tag{2.9}$$

where $k_B T$ is the Boltzmann constant times temperature, ρ is the mass density of a two-dimensional substance, v_{ac} is the sound velocity, D_{ac} is the intravalley acoustic phonon deformation potential and N_{2D} is the 2D density of states. In low electric field or low electron energy circumstances, acoustic phonon scattering is the predominant scattering process because of the small amount of transfer of energy.

doi:10.6342/NTU202403452

On the other hand, optical phonon scattering, also originated from the energy perturbation caused by strain even though optical phonons exist in different atomic vibration directions. Optical phonon energy remains non-zero even as the **q** momentum approaches zero. When there is no phonon energy, energy must either be emitted or absorbed during the electron and phonon contact process. Using the perturbation potential formulation, the optical phonon scattering rate may be expressed as the following equation similarly [91]:

$$W_{Op}(k) = \frac{\pi D_{Op}^2}{2\rho\omega_0}\left[n(\omega_0) + \frac{1}{2} \mp \frac{1}{2}\right] N_{2D}(E_k \pm \hbar\omega_0), \tag{2.10}$$

2.5.2 Intervalley Scattering

Carriers may travel from one valley to another since the band structure has several valleys. This valley-to-valley scattering of carriers resembles a deformation potential interaction. Energy conservation must be met during the scattering process whenever electrons take in and release a phonon. The phonon-assisted scattering between intervalley may be expressed as [91]:

$$W_{Ac}^{abs/emi}(k) = \frac{\pi D_{Ac}^2}{2\rho\omega}\left[n(\omega_{Ac}) + \frac{1}{2} \mp \frac{1}{2}\right] N_{2D}(E_k \pm \hbar\omega_{Ac}), \tag{2.11}$$

$$W_{Op}^{abs/emi}(k) = \frac{\pi D_{Op}^2}{2\rho\omega}\left[n(\omega_{Op}) + \frac{1}{2} \mp \frac{1}{2}\right] N_{2D}(E_k \pm \hbar\omega_{Op}), \tag{2.12}$$

The footnotes ”Ac” or ”Op” indicate the phonon type engaged in intervalley scattering. All scattering mentioned above formulas could be applied to hole transport as well.

doi:10.6342/NTU202403452

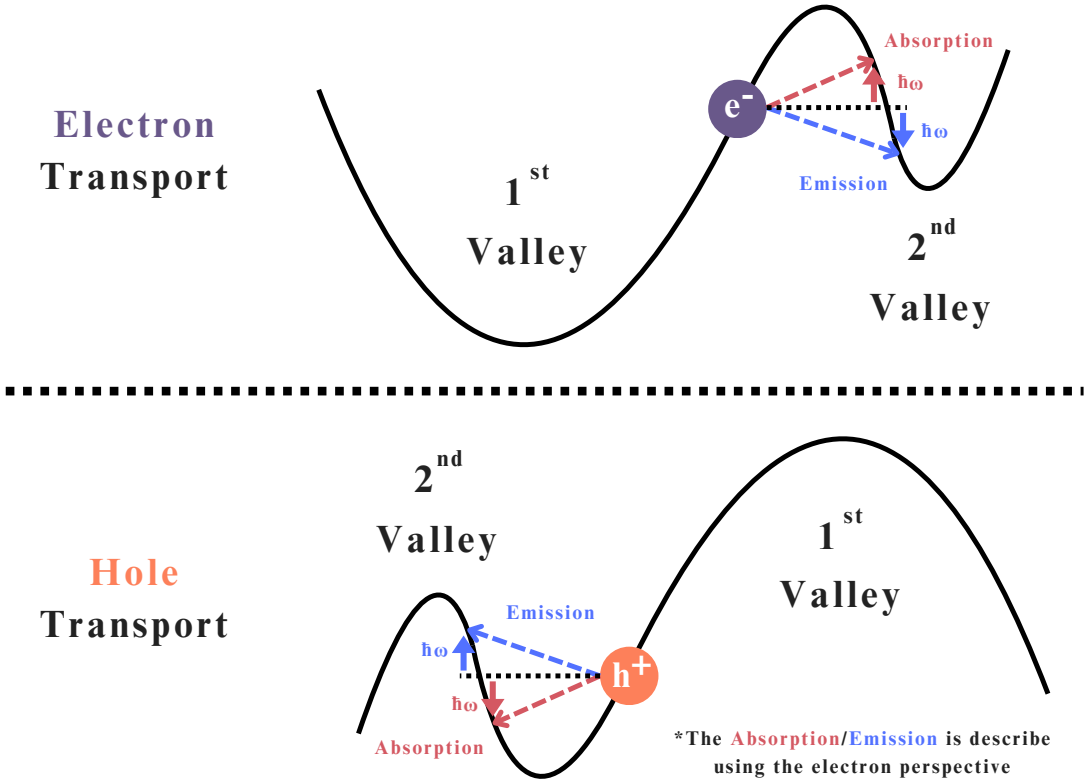

Figure 2.5: The electron/hole mechanism of intervalley e-ph scattering. Electrons from phonons can be absorbed or emitted, causing scattering between the two valleys.

doi:10.6342/NTU202403452

2.6 Multi-valley Monte Carlo method

The physical information required to model transport qualities using the Monte Carlo approach is provided via DFT, DFPT, and EPW computations. Carrier transport in a similar fashion to Fig. 1.4 after accelerated by an electric field. During ballistic transport, a carrier experiences repeated collisions with phonons–quantized lattice vibrations within a material. The carrier's momentum and velocity fluctuate randomly due to these scattering occurrences. An effective technique for simulating this intrinsically unpredictable process is the Monte Carlo approach. The approach precisely reconstructs the carrier's track, allowing the study of its transport characteristics within the material, by statistically sampling the time intervals between scattering events and the post-scattering state. The Monte Carlo method's specific stages are shown in Fig 2.6.

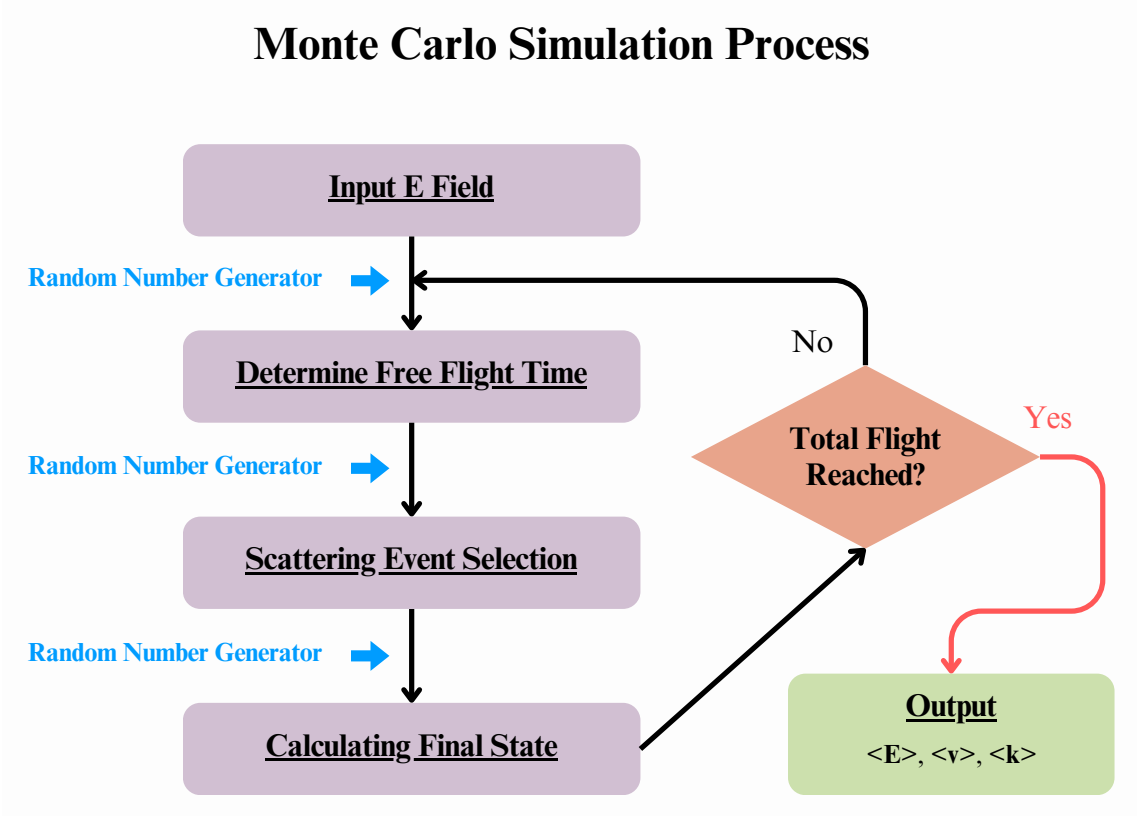

Figure 2.6: The process of Monte Carlo simulation.

doi:10.6342/NTU202403452

The final state of simulated electrons, scattering events, and free-flight time are controlled by a Monte Carlo method using random number generation. Through hundreds of repetitions of this procedure in a certain electric field, we can determine the average carrier velocity and mobility. To ensure statistical stability and mitigate any potential biases resulting from the random number sequence, every simulated electron is given a total flight period of 10^5 nm. Mobility and velocity parameters that depend on the given field can be assessed using this method.

2.7 Poisson and Drift-Diffusion Model

The self-consistent drift-diffusion equation model is the most basic and well-known model that describes semiconductor device physics and its electrical properties. This approach was created over 20 years ago and has been extremely successful in numerous academic groups ever since. The Poisson equation describes the potential distribution in the device via carrier distribution under a given bias, and the drift-diffusion equation expresses the current distribution. Both the Poisson and drift-diffusion equations are solved self-consistently through an iterative process, in which the equations are as follows:

$$\nabla D = \nabla_r \cdot [\epsilon \nabla_r V(r)] = q(N_A^- - N_D^+ + n(E_c, E_{fn}) - p(E_v, E_{fp})), \tag{2.13}$$

$$J_n = -q\mu_n n(E_c, E_{fn}) \nabla_r V(r) + qD_n \nabla_r n(E_c, E_{fn}), \tag{2.14}$$

$$J_p = -q\mu_p p(E_v, E_{fp}) \nabla_r V(r) - qD_p \nabla_r p(E_v, E_{fp}), \tag{2.15}$$

where V is the electric potential, E_c is the conduction band potential, E_v is the valance band potential, E_{fn} and E_{fn} are the quasi-fermi level for electron and hole, respectively. N_A^- is the doping concentration of the acceptor, N_D^+ is the doping concentration of the

doi:10.6342/NTU202403452

donor, n is the concentration of electrons, p is the concentration of holes, notations J and D are the current densities and diffusion coefficients, accordingly. Our in-house developed 2D finite-element-based Poisson-drift-diffusion solver (2D DDCC) is employed for all simulations, enabling us to analyze the performance of a wide range of devices. This solver is the basis for all device simulations discussed in this work. Those who are interested in this software could check Dr. Wu's website at http://yrwu-wk.ee.ntu.edu.tw/.

2.8 Absorption-related Properties Extraction

A random-phase approximation (RPA) frequency dependent complex dielectric function is used to obtain the absorption-related properties implemented in the epsilon.x code in Quantum Espresso [86]. Mainly three parameters are calculated using this code: the real part of the dielectric function ϵ_r, the imaginary part of the dielectric function ϵ_i, and the joint density of states (JDOS). The smearing type is set to 'gauss', the number of points of the frequency mesh is set to 10000 to ensure enough emergence of JDOS peaks, and the smearing is set to 0.0259 (close to a single k_BT) in all epsilon.x calculation input.

After requiring the three key parameters, the absorption coefficient α for the interested 2D material is calculated using the following equation:

$$\alpha(\hbar\omega) = \frac{\epsilon_i \omega}{cn} = \frac{W_{abs}}{cn_{ph}}, \tag{2.16}$$

with the light speed c and the refractive index $n = 1$ due to a large vacuum introduced in the simulated system [7]. Then the α can written into the form of a direct band-to-band absorption rate W_{abs} and the incident photon number n_{ph}, which can further be used to extract the energy equivalents of the principal inter-band momentum matrix elements $\mathbf{E}_p$.

doi:10.6342/NTU202403452

The band-to-band absorption rate W_{abs} is written as [65]:

$$\mathbf{W}_{abs} = \frac{\pi e^2 \hbar n_{ph}}{\epsilon_r m_0^2 (\hbar\omega)} |(a \bullet p)_{cv}|^2 N_{JDOS}, \tag{2.17}$$

and the $\mathbf{E}_p$ is defined as:

$$\mathbf{E}_p = \frac{2|(a \bullet p)_{cv}|^2}{m_0}, \tag{2.18}$$

where N_{JDOS} stands for epsilon.x calculated JDOS for the calculated system, which is calculated using the below formula:

$$N_{JDOS} = \sum_{\mathbf{k}} \sum_{i} \sum_{f} \frac{1}{\sigma\sqrt{\pi}} \exp\left\{ \frac{-(E_{\mathbf{k},f} - E_{\mathbf{k},i} - \omega)^2}{\sigma^2} \right\} \times \frac{2k_x k_y}{(2\pi)^2}, \tag{2.19}$$

with a broadening factor σ, and the transition energy of $E_{\mathbf{k},f} - E_{\mathbf{k},i}$. On the other hand, the N_{JDOS} using the theory of 2D JDOS can be written via reduced effective mass (m_r^*) as follow:

$$N_{2D,JDOS} = \frac{m_r^*}{\pi\hbar} = \frac{(\frac{1}{m_e^*} + \frac{1}{m_h^*})^{-1}}{\pi\hbar}. \tag{2.20}$$

doi:10.6342/NTU202403452

Chapter 3

Properties of Janus MoSSe

3.1 Overview

This chapter delves into the fundamental transport and contact properties of Janus MoSSe. MoSSe was chosen for this investigation due to its pioneering role as the first discovered JTMD and its prevalence in synthesis [73, 74]. We begin by examining the band structures of MoSSe for mono-layer (1L), bi-layer (2L), and tri-layer (3L) configurations. Subsequently, leveraging calculated deformation potentials, we determine the intrinsic transport mobilities of electrons and holes for 1L- and 3L-MoSSe. These intrinsic mobilities, dominant under low carrier and impurity concentrations, represent the upper limit of a material's transport properties. Notably, the mobility of 3L-layer MoSSe is further employed in device simulations. In parallel, we explore the hetero-structures of MoSSe to elucidate their contact characteristics and understand how MoSSe's contacts deviate from those of traditional TMD materials.

doi:10.6342/NTU202403452

3.2 Band Structures and Related Electronic Characteristics of MoSSe

3.2.1 Structural Relaxation and Band Structures

To study how the MoSSe layer affects the electron characteristic, we construct an AA' 2L-MoSSe and AA'A 3L-MoSSe structure as our main calculating systems since The AA' and AA'A stacking shows a relatively stable stacking sequence among five stacking sequences for TMD materials [92, 93].

The DFT calculated lattice constant for the 1L-, 2L-, and 3L-MoSSe are 3.25 Å, 3.23 Å, and 3.23 Å, respectively. The layer distance (From Mo to Mo) and the interlayer distance are about 6.44 Å and 3.24 Å, respectively, showing a good agreement with previous studies [79, 81].

Table 3.1: The DFT calculated lattice constants, band gaps, K – Q valley separations (ΔE_{KQ}), K–Γ valley separations ($\Delta E_{K\Gamma}$ / $\Delta E_{\Gamma K}$), and the effective masses at relevant energy valleys for all MoSSe systems.

MoSSe Layer	a (Å)	E_g (eV)	ΔE_{KQ} (eV)	$\Delta E_{K\Gamma}$ / $\Delta E_{\Gamma K}$ (eV)	m_{eK} (m_0)	m_{eQ} (m_0)	m_{hK} (m_0)	$m_{h\Gamma}$ (m_0)
1L	3.25	1.56	0.21	0.02 ($\Delta E_{K\Gamma}$)	0.51	0.81	0.61	2.90
2L	3.23	0.78	0.11	0.15 ($\Delta E_{\Gamma K}$)	0.46	0.79	0.58	1.30
3L	3.23	0.24	0.40	0.36 ($\Delta E_{\Gamma K}$)	0.37	0.47	0.48	0.75

Figure 3.1 depicts three systems' resulting electronic band structures. Only the single layer MoSSe exhibits a direct band gap with the conduction minimum and valence band maximum located at the same K point in the momentum space. Increasing the number of MoSSe layers to two and three induces a transition in the valence band maximum to the Γ point, signifying a characteristic shift towards an indirect band gap. 1L-MoSSe exhibits a band gap of 1.56 eV, which progressively decreases to 0.78 eV and 0.24 eV for 2L-MoSSe

doi:10.6342/NTU202403452

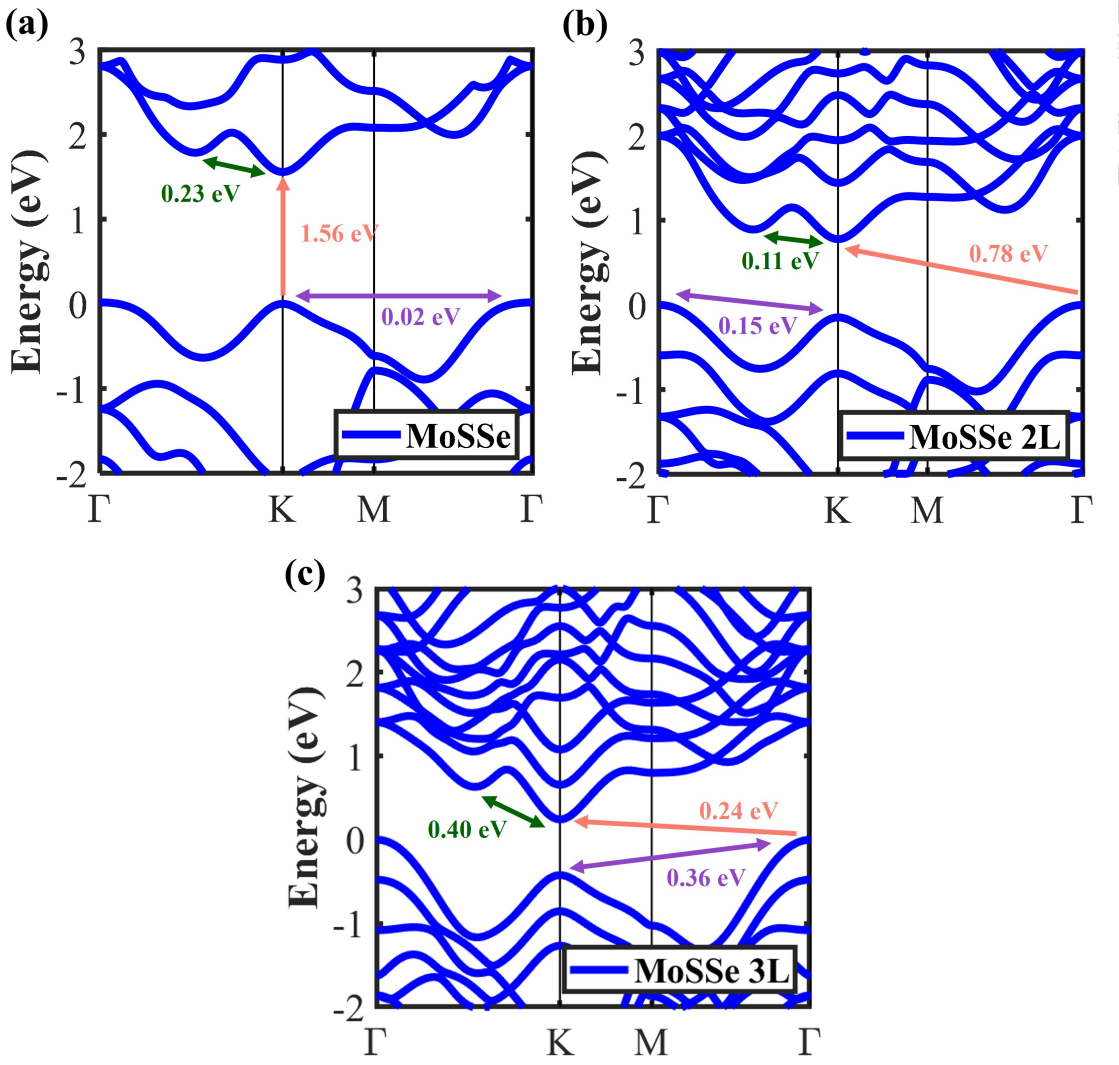

Figure 3.1: Schematic of the calculated band diagram of (a) 1L-layer MoSSe, (b) AA' stacking 2L-MoSSe, and (c) AA'A stacking 3L-MoSSe.

and 3L-MoSSe, respectively. Beyond the band gap, the first conduction band displays the second lowest six-fold degeneracy valley at the K-Γ direction, often referring to the Q valley. The energy difference between K and Q valleys, denoted as ΔE_{KQ}, can be directly extracted from the band diagram. Similarly, the highest valence band exhibits two dominant valleys at the K and Γ points. Their energy difference, $\Delta E_{K\Gamma}$, can also be determined from the calculated band structure. These energy differences significantly influence transport characteristics, which will be discussed in a dedicated chapter. In summary, Table 3.1 compiles the band-related parameters obtained from the DFT calculations.

doi:10.6342/NTU202403452

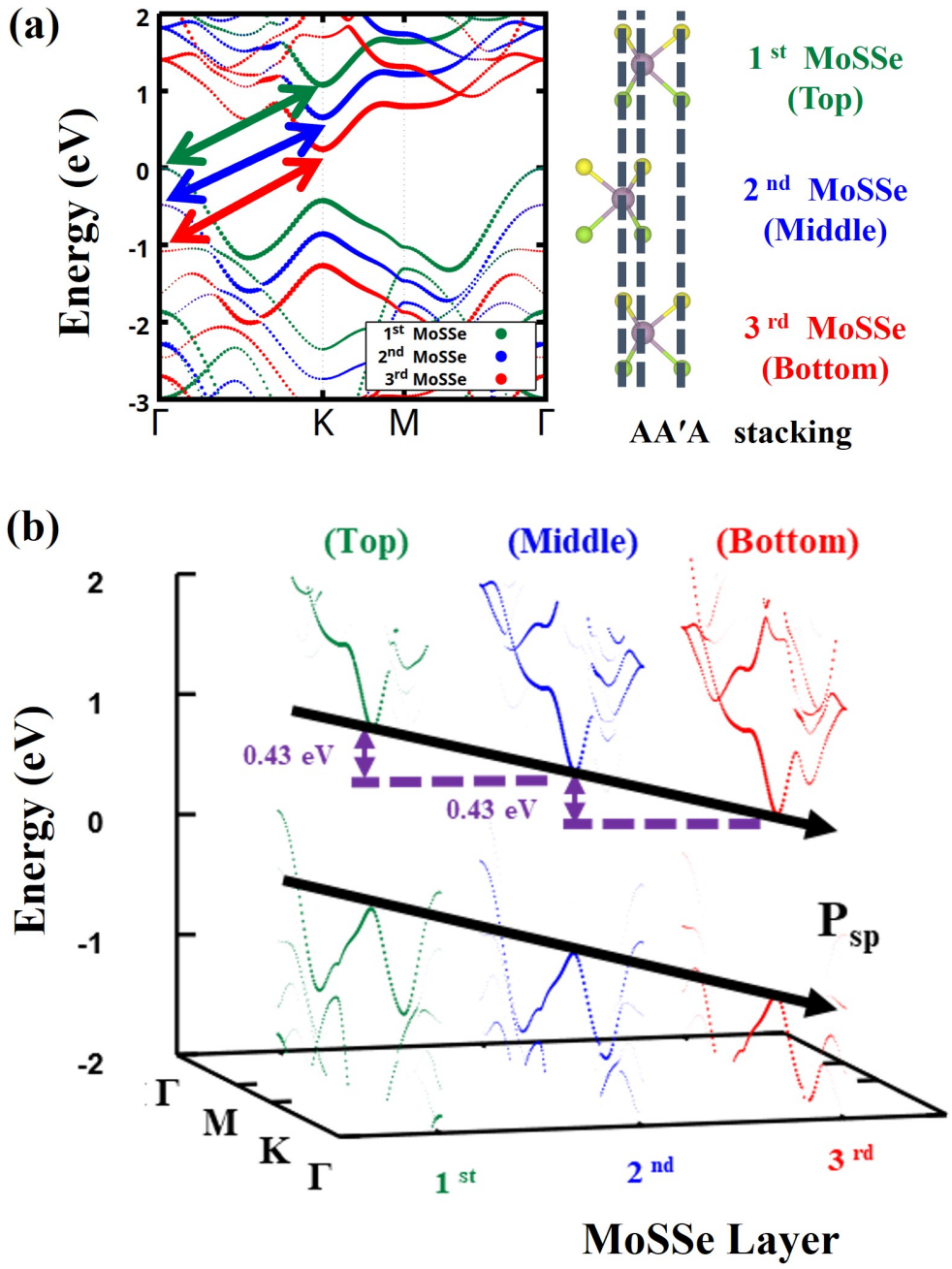

Figure 3.2: (a) The projected band structure of 3L-MoSSe with AA'A stacking is presented. Green, blue, and red dots differentiate the top, middle, and bottom MoSSe layers, respectively. (b) The projected band structure of the 3L-MoSSe is shown from a side view, highlighting the mutual offset in each layer. This offset leads to a P_{sp} throughout the system, depicted by the black arrow. This work has been published in [3].

To delve deeper into the layer-dependent properties of the 3L-MoSSe system, its projected band structure is presented in Fig. 3.2(a). All three MoSSe layers exhibit an indirect band gap, with the conduction band minimum located at the K valley and the valence band maximum at the Γ valley. Figure 3.2(b) further details the projected band

doi:10.6342/NTU202403452

structure for each MoSSe layer. The green, blue, and red dots represent the contributions from the top, middle, and bottom layers, respectively, corresponding to the colored arrows in Fig. 3.2(a). By isolating the band components of each layer, we observed a systematic shift of 0.43 eV with the addition of each MoSSe layer. This translates to an average band gap of 1.212 eV for a single MoSSe layer if considered independently. This inter-layer interaction stems from the intrinsic out-of-plane dipole moment within MoSSe. Analogous to those spontaneous polarization inherent materials such as gallium nitride, this dipole effect can be incorporated in device simulations using a spontaneous polarization term, P_{sp}, represented by the two diagonal black arrows in Fig. 3.2(b).

3.2.2 Spontaneous Polarization

The electrostatic potential plot can also present the P_{sp} phenomenon, which is also used to determine the intrinsic electric field E in MoSSe systems. As Fig. 3.3 shows, the electron affinity of MoSSe decreases from 5.33 eV for a mono-layer to 4.47 eV for a bi-layer and reaches 3.97 eV for a tri-layer. The energy offset in 3.3(c) also corresponds well with the systematic shift in Fig. 3.2(b). By dividing the single-layer energy difference by the distance between two vacuum regions, we can obtain the MoSSe's intrinsic dipole field, presented by E, in the vertical direction. According to the calculation results, the calculated electric dipole field is approximately 1.36×10^9 V/m. This electric dipole field value is much higher than that of common III-V semiconductor compounds such as GaN. This strong dipole characteristic endows MoSSe with significant potential for application in various devices.

The out-of-plane dielectric constant, which is the other important component for P_{sp}, is calculated through the DFPT method and is distilled to a 2D component using the equiv-

doi:10.6342/NTU202403452

alent capacitance strategy (See section 2.3.2), which the results before and after distilled are both given in Table 3.2. After extracting $\epsilon_{2D,\perp}$ and E, the MoSSe's P_{sp} term can be obtained by Eqn. (2.3), which the results are also recorded in Table 3.2.

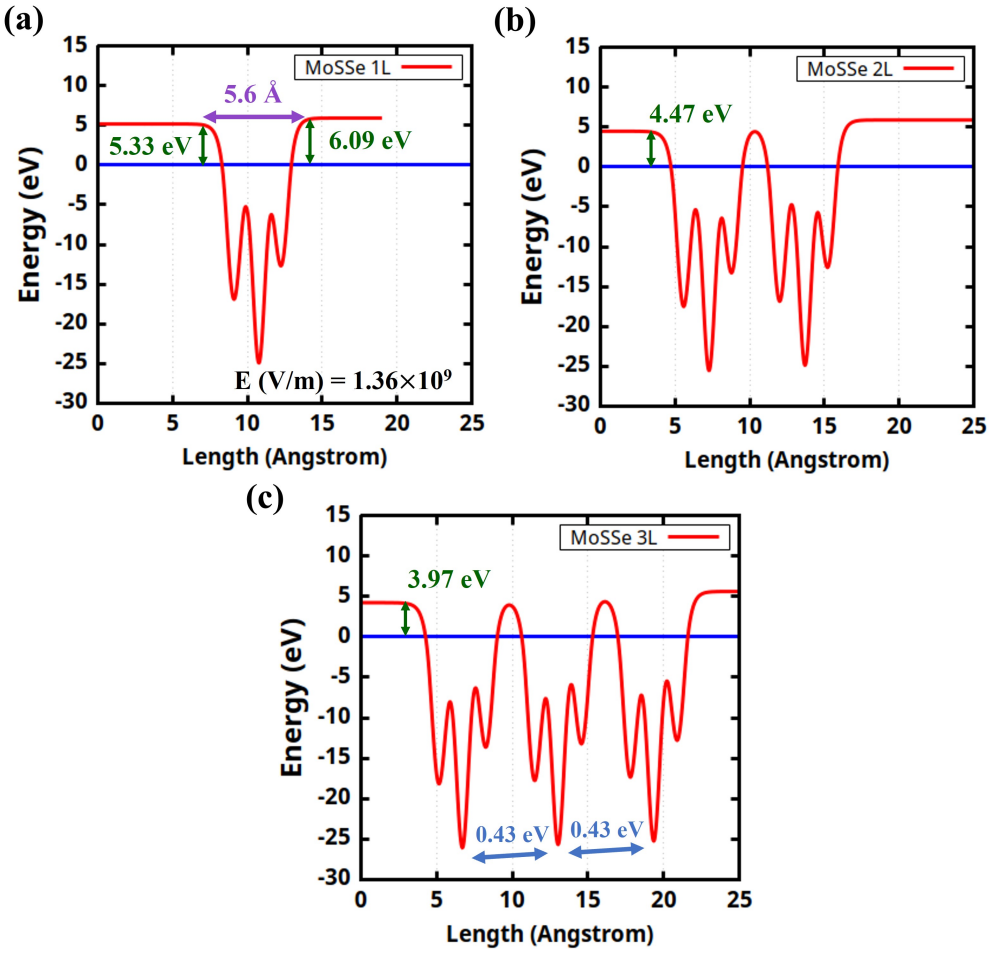

Figure 3.3: The DFT calculated electrostatic potential plot with (a) 1L-MoSSe, (b) 2L-MoSSe, and (c) 3L-MoSSe. The intrinsic dipole field of MoSSe is also calculated. The electron affinity for each system can also be known from the left-hand side vacuum region.

Table 3.2: The DFT calculated electron affinity, in-plane dielectric constant, out-of-plane dielectric constant, and the spontaneous polarization for all MoSSe systems. d and c are defined Eqn. (2.1) and (2.2).

MoSSe Layer	E_{ea} (eV)	c (nm)	d (nm)	$\epsilon_{All,\parallel}$ (ϵ_0)	$\epsilon_{All,\perp}$ (ϵ_0)	$\epsilon_{2D,\parallel}$ (ϵ_0)	$\epsilon_{2D,\perp}$ (ϵ_0)	P_{sp} (cm^{-2})
1L	5.33	20	6.42	5.70	1.36	15.65	5.81	4.31×10^{13}
2L	4.47	35	13.05	6.48	1.45	15.70	5.96	4.40×10^{13}
3L	3.97	35	19.00	9.10	1.84	15.93	6.31	4.76×10^{13}

doi:10.6342/NTU202403452

3.3 Contact Characteristic of MoSSe

3.3.1 MoSSe with Graphene as Contact

Building upon the influence of P_{sp}, we now investigate its impact on MoSSe-contact interactions. Our initial focus is on the common 2D material contact graphene (Gr). Thus, the Gr/AA'A-MoSSe/Gr heterostructure, where the S and Se sides of MoSSe are attached to Gr electrodes. This configuration introduces a 1.11% lattice mismatch between MoSSe and Gr. Figure 3.4(b) depicts the projected band structures of this system. Intriguingly, when Gr contacts the Se-face of 3L-MoSSe (shown in red), the Fermi level of the entire system dips 0.38 eV below the MoSSe conduction band, signifying the formation of an n-type Schottky barrier. Conversely, Gr contact with the S-face of 3L-MoSSe (shown in green) reveals a p-type Ohmic contact at the Γ point. These observations align well with previous research on JTMD-graphene contacts [80, 81].

The unique P_{sp} property likely explains the formation of both n- and p-type contacts depending on the contacting face of MoSSe with Gr. Furthermore, Figure 3.4(c) illustrates the impact of this intrinsic dipole. When the Se-face contacts Gr, the P_{sp} pulls Gr downwards, shifting its Fermi level above the Dirac cone, resulting in intrinsically n-doped Gr. Additionally, the P_{sp} tilts the band edges of Gr, leading to a smaller energy difference between the Gr Fermi level and the MoSSe conduction band compared to the valence band offset at the Se/Gr interface. This scenario favors the formation of an n-type region. On the other hand, S-side attachment elevates the Gr band energy, causing the valence band edge to intersect the Fermi level. This indicates intrinsic p-doping of Gr and the formation of a p-type contact region. Notably, the integrity of the Dirac cone in both Gr structures within

doi:10.6342/NTU202403452

the band diagram suggests the presence of physisorption between the two materials [94].

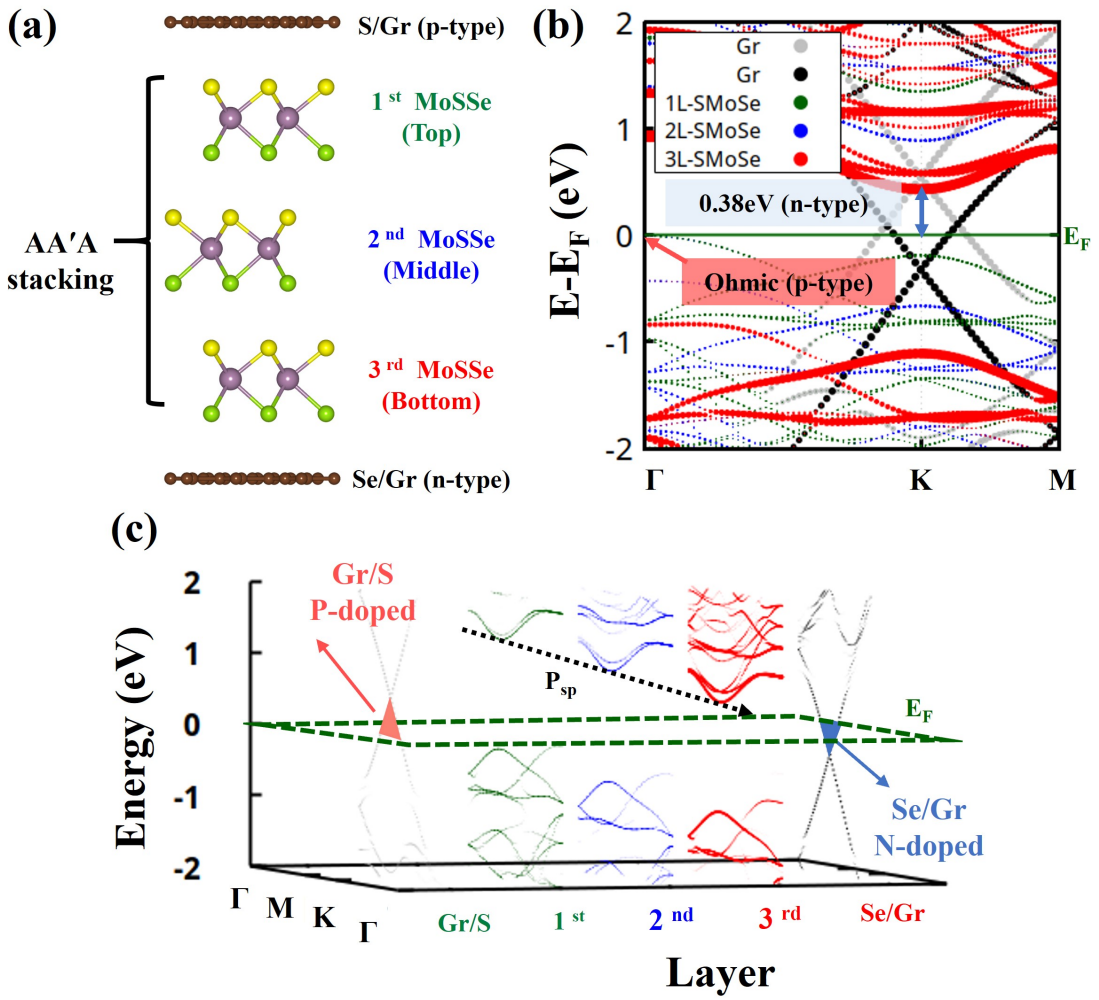

Figure 3.4: (a) Schematic of the calculated Gr/AA'A-MoSSe/Gr heterostructure. The color scheme for the MoSSe layers corresponds to the previous 3L-MoSSe projected band figure. Gray and black dots represent the contributions from the S/Gr and Se/Gr electrodes, respectively. (b) Projected band structures for the Gr/AA'A-MoSSe/Gr system, revealing a 0.38 eV n-type Schottky barrier contact and a p-type Ohmic contact. (c) Side-view depiction of the layer separation within the Gr/AA'A-MoSSe/Gr system. The intrinsic dipole field (i.e. P_{sp}) induces p-type doping on the Gr electrode attached to the S-face of MoSSe and n-type doping on the Gr electrode attached to the Se-face. This work has been published in [3].

3.3.2 MoSSe with Metal as Contact

Complementing our investigation with practical considerations, we explore metal contact systems due to their prevalence in electrode applications. Common materials like

doi:10.6342/NTU202403452

aluminum (Al) and copper (Cu) were chosen for this exploration [42, 43, 47–49]. Figure 3.5(a) depicts the simulated heterostructure of a 2L-MoSSe material with a metal contact. Figures 3.5(b) and 3.5(c) showcase top-down views of this structure for both Al and Cu contacts, revealing lattice mismatches of 0.44% and 2.97% for 2L-MoSSe/Al and 2L-MoSSe/Cu, respectively.

To understand the electronic interactions, Figures 3.6(a) through 3.6(d) present the projected band structures. Figures 3.6(a) and 3.6(c) depict the scenario where the Se-face of MoSSe contacts the electrode, while Figures 3.6(b) and 3.6(d) represent the S-face attachment. When bilayer MoSSe (2L-MoSSe) attaches to the Al (111) face on either the Se or S side (as shown in Figures 3.6(a) and 3.6(b)), the 2L-MoSSe band aligns with the Fermi level, indicating the formation of Ohmic contacts between the metal and 2L-MoSSe states. Unlike the previous Gr cases, the projected band structures for these metal contacts reveal chemisorption characteristics due to the presence of significant hybridization evident in the band diagram.

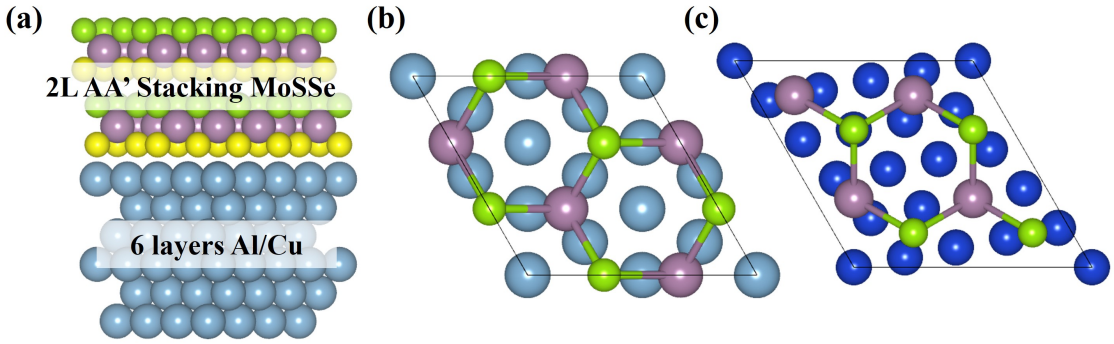

Figure 3.5: (a) A computed 2L-MoSSe/metal heterostructure system illustration. Top views of the 2L-MoSSe/Al (111) and 2L-MoSSe/Cu (111) systems are shown in (b) and (c), respectively.

A key difference between MoSSe and typical TMDs is the role of the internal electric field in MoSSe. This field plays a crucial role in enhancing the density of interface states. In MoSSe specifically, the electric field promotes the creation of electronic energy levels

doi:10.6342/NTU202403452

at the metal-semiconductor interface through a chemisorption-like bonding process. This phenomenon leads to a higher density of interface states between the two materials [57]. These additional bonding states, arising from the P_{sp} in MoSSe, are highlighted by the dotted frames in the density of states (DOS) plots for all systems [94]. Due to the presence of these additional chemical bonding states, it becomes difficult to definitively identify the MoSSe band edge closest to the metal layer.

We analyze the impact of the previously mentioned P_{sp} direction on the band-edge distribution of the MoSSe layer closest to the metal (1L MoSSe). We then correlate this analysis with the peak observed at the valence band edge (Ev edge) of MoSSe layers. The corresponding band edge with its Density of States (DOS) is depicted on the right side of Figs. 3.6(d) and (e). In the Se-face contact with Al (Fig. 3.6(a)), the Fermi level aligns with the valence band edge of the outer MoSSe layer (2L MoSSe). Due to the upward P_{sp}, the energy band of the inner layer (1L MoSSe) shifts downwards. Supported by the peak at the Ev edge, this suggests a Fermi level closer to the conduction band, indicative of an n-type contact tendency. Conversely, when the S face contacts Al (Fig. 3.6(b)), the downward P_{sp} pushes the energy band of 1L MoSSe upwards. Comparing this scenario, the Fermi level resides in the middle of the band gap, suggesting a p-type contact tendency. While we can infer n- or p-type tendencies in both systems, the presence of numerous bonding states within the gap region of 1L MoSSe signifies the formation of Ohmic contacts. This implies that both electrons and holes can readily flow through this low-tunneling barrier, ultimately enhancing device performance. Similar observations of n- and p-type Ohmic contact formation are made for Cu (111) with different face attachments (Fig. 3.6(c) and (d)). This suggests that Cu can also form Ohmic contacts upon attachment to 2L-MoSSe. This chemisorption-like property offers the advantage of reducing the tunneling barrier at

doi:10.6342/NTU202403452

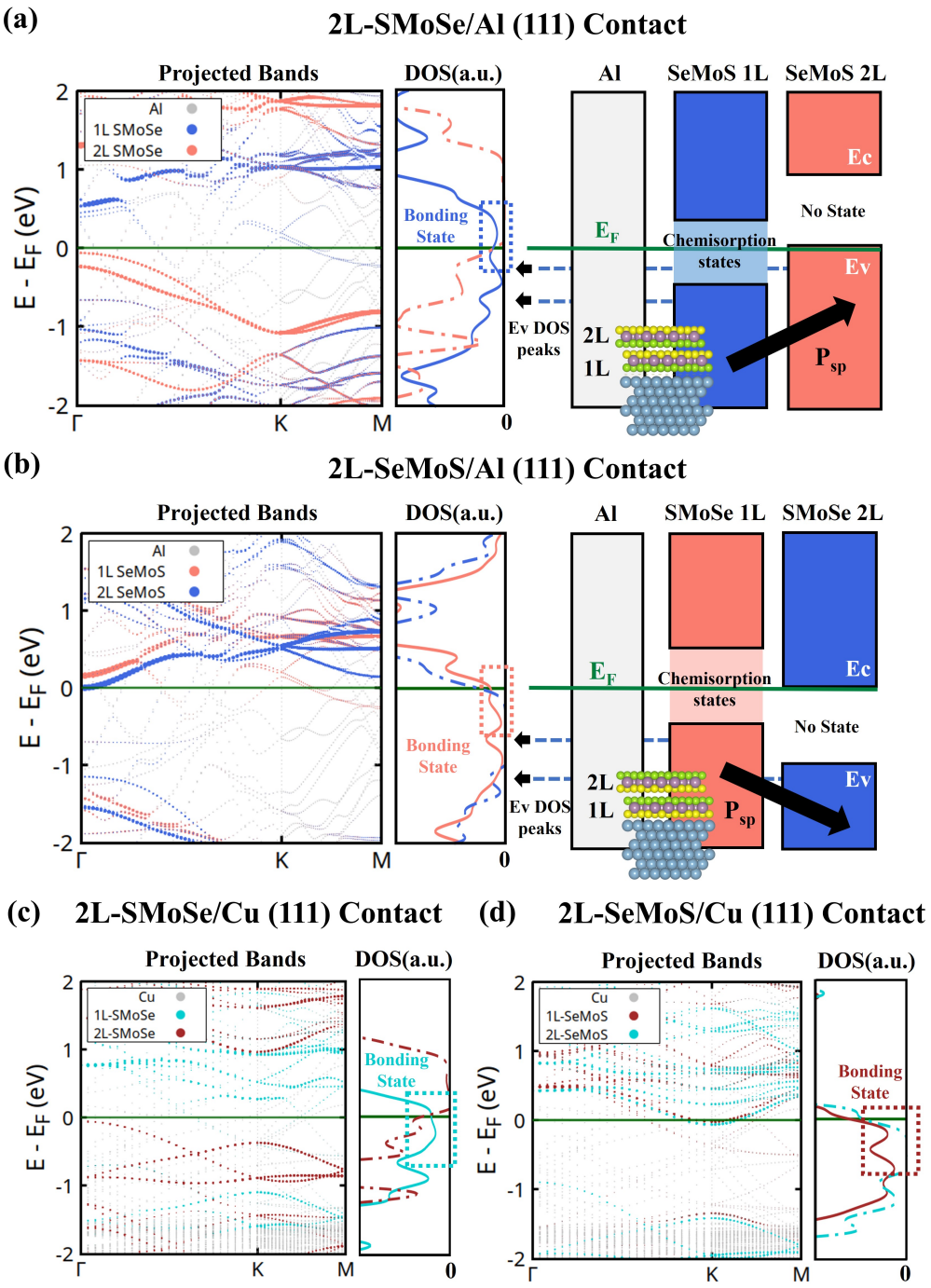

Figure 3.6: (a) and (c) are the projected band structures with Se-side contact. (b) and (d) are the projected band structures with S-side contact. For all 2L-MoSSe/Al systems, the 2L-MoSSe DOS is given. For reference, the band-edge correspondence diagram showing the connection between the valence band (Ev) and conduction band (Ec), and Fermi level (Ef) is placed on the right side of the picture. The projected band structures and the 2L-MoSSe DOS of the MoSSe Se-side and S-side contact with Cu are shown in (c) and (d), respectively. The metals' contributions are the gray areas. This work has been published in [3].

doi:10.6342/NTU202403452

the contact region, leading to improved device performance [57, 94].

3.4 Intrinsic Transport of Mono- and Tri-layered MoSSe

Phonon scattering mechanisms, particularly acoustic, optical, and inter-valley scattering, significantly influence the intrinsic transport properties of TMD materials. The calculated scattering rates from the EPW method are used within a Monte Carlo simulator to determine transport characteristics like mobility and peak velocity. This analysis focuses on both 1L- and 3L- MoSSe. 1L-MoSSe is the foundation for layered MoSSe structures, while 3L-MoSSe will be employed in future device simulations.

Figure 3.7 presents the EPW-calculated scattering rates for electrons and holes in 1L-MoSSe. All scattering rates are calculated at 300 K. Figure 3.7(a) shows the electron scattering rates for K valleys, with the wave vector k of the initial electronic state selected along the K-Γ direction. Similarly, panel Fig. 3.7(b) depicts the Q-valley electron scattering rates with the wave vector k chosen along the Q-Γ direction. Figure 3.7(c) and (d) depict the scattering rates for holes in the K and Γ valleys along the K-Γ path of MoSSe, respectively. As carrier energy increases, acoustic phonon scattering consistently dominates over optical phonon scattering for both electron valleys (Fig. 3.7(a) and (b)) and the Γ valley for holes (Fig. 3.7(c)). However, for the K valley in holes (Fig. 3.7(d)), optical phonon scattering plays a more significant role at low carrier energies, gradually diminishing at higher energies. The abrupt increases in scattering rates likely correspond to the onset of intervalley scattering (e.g., K-to-Q electron or K-to-Γ hole transitions) or the emission of the optical phonon. The initiation of intervalley transition is mainly determined by the valley energy difference ($\Delta E_{K\Gamma}$ for electron and $\Delta E_{K\Gamma}$ for hole) in the

doi:10.6342/NTU202403452

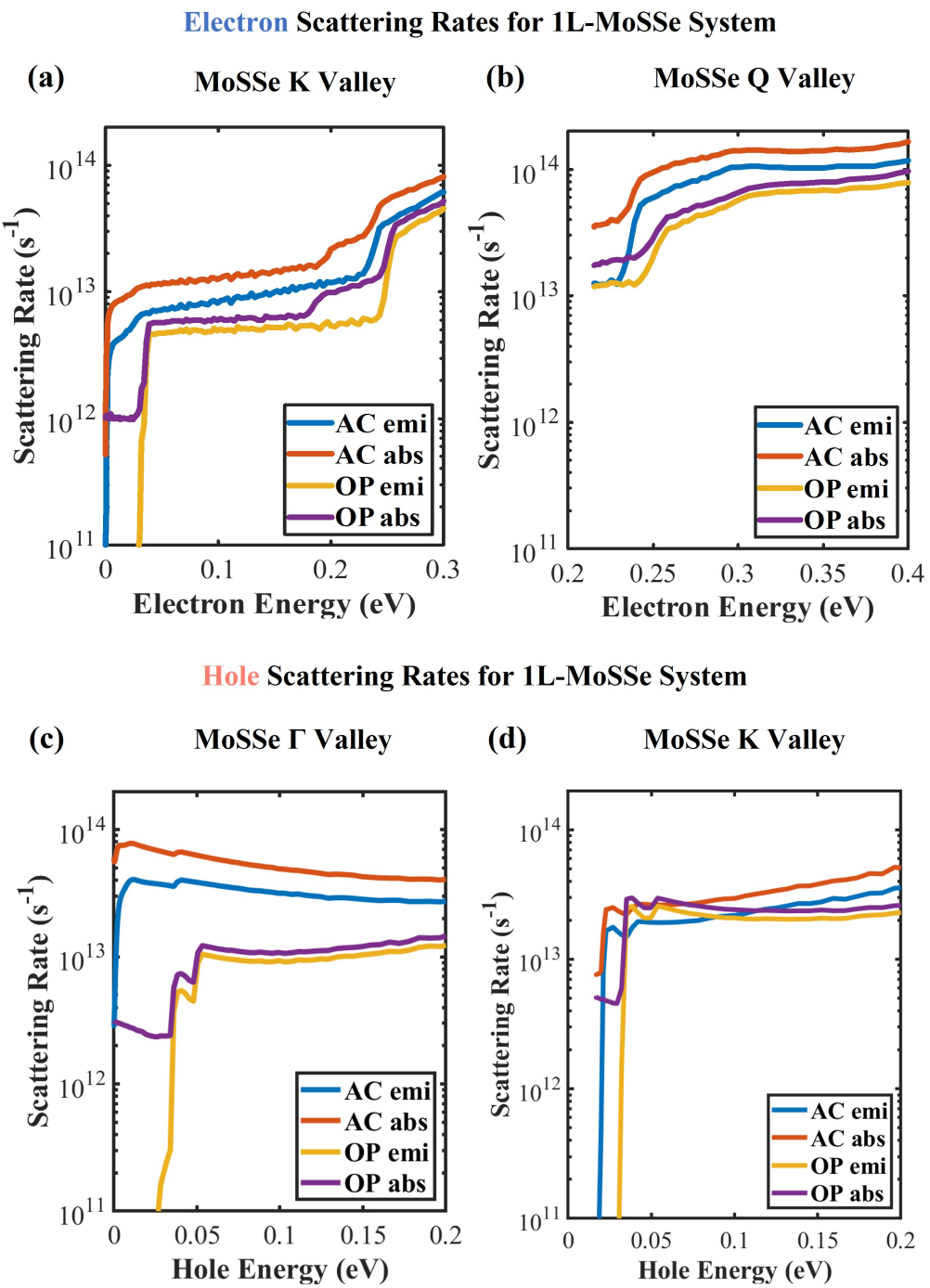

Figure 3.7: Electrons scattering rates of the lowest conduction band in (a)K and (b)Q valleys of 1L-MoSSe calculated at 300 K. Hole scattering rates in (c)Γ and (d)K valleys of 1L-MoSSe calculated at 300 K. The AC and OP denote acoustic and optical phonon; emi and abs denote emission and absorption, respectively.

band diagram. DFT calculation retrieves the phonon energy and deformation potential constants needed for the computation, where the deformation potential used for MoSSe electron and hole are given in the following two tables:

doi:10.6342/NTU202403452

Table 3.3: MoSSe deformation potential constants in the K and Q conduction bands, where D stands for the deformation potential constants. "ac" is acoustic phonons, and "op" is optical phonons. The relevant modes' phonon energies are averaged and shown in the third column [4].

MoSSe Electron		
Intravelly Transition	D_1 (eV)	$\hbar\omega$ (meV)
K→ K(Γ), (ac)	5.8	0
Q→ Q(Γ), (ac)	4.8	0
Intervelly Transition	D_0 (10^8 eV/cm)	$\hbar\omega$ (meV)
K→ K(K), (op)	3.6	30.62
K→ K(K), (ac)	1.8	19.18
K→ K(K), (op)	3.3	31.88
K→ Q(Q), (ac)	2.0	14.95
K→ Q(Q), (op)	5.2	32.51
K→ Q(M), (ac)	3.7	18.30
K→ Q(M), (op)	6.2	31.89
Q→ Q(Γ), (op)	6.4	30.62
Q→ Q(Q), (ac)	4.8	14.95
Q→ Q(Q), (op)	4.6	32.51
Q→ Q(M), (ac)	2.5	18.30
Q→ Q(M), (op)	4.9	31.89
Q→ Q(K), (ac)	3.0	19.18
Q→ Q(K), (op)	5.4	31.88
Q→ K(Q), (ac)	1.2	14.95
Q→ K(Q), (op)	5.1	32.51
Q→ K(M), (ac)	3.3	18.30
Q→ K(M), (op)	6.0	31.89

Since deformation potential is mainly dependent on lattice dimensions, which differs less than 1% between mono-layer (3.25 Å) and tri-layer (3.23 Å) comparing our variable cell relaxation results[95, 96], thus, deformation potentials extracted from 1L-MoSSe are applied onto 3L-MoSSe for both electron and hole transport. Figure 3.8 presents the Monte Carlo simulations of electron and hole low field mobility and peak velocity versus electric field for 1L- and 3L-MoSSe. The 3L-MoSSe shows the best low-field mobility with a value of 667 $cm^2V^{-1}s^{-1}$, while 1L-MoSSe showcases the worst 22 $cm^2V^{-1}s^{-1}$ mobility.

Comparing the carrier low-field mobility values between the two systems reveals a

doi:10.6342/NTU202403452

Table 3.4: MoSSe deformation potential constants in the Γ and K valence bands, where D stands for the deformation potential constants. "ac" is acoustic phonons and "op" is optical phonons. The relevant modes' phonon energies are averaged and shown in the third column.

MoSSe Hole		
Intravelly Transition	D_1 (eV)	$\hbar\omega$ (meV)
K→ K(Γ), (ac)	3.8	0
Γ → Γ(Γ), (ac)	3.8	0
Intervelly Transition	D_0 (10^8 eV/cm)	$\hbar\omega$ (meV)
K→ K(K), (ac)	0.8	25.37
K→ Γ(K), (ac)	1.1	25.37
Γ → K(K), (ac)	2.8	25.37
K→ K(Γ), (op)	4.0	46.52
K→ K(K), (op)	1.5	42.83
K→ Γ(K), (op)	3.0	42.83
Γ → Γ(Γ), (op)	5.2	46.52
Γ → K(K), (op)	1.8	42.83

significant improvement in the 3L system for both electrons and holes. Since the deformation potential remains the same between 1L and 3L, the low-field mobility is mainly affected by the valley energy separation (ΔE) and effective first valley's mass, where table 3.5 listed the information of these curtail factors. The mobility enhancement is partially attributed to the increased ΔE between the two valleys. Specifically, ΔE rises from 0.21 eV to 0.4 eV for electrons, and ΔE increases from 0.02 eV (indicating strong intervalley scattering in very low energy) to 0.36 eV. This elevation in energy difference enhances carrier confinement within the same valley, reducing changes in carrier transport valleys,

Table 3.5: The MoteCarlo simulated low-field mobility, accompanied by valley energy separation, the two valley's effective masses, and the two valley's non-parabolic parameter α for all MoSSe systems.

MoSSe System	μ ($cm^2V^{-1}s^{-1}$)	ΔE (eV)	1^{st} Valley m (m_0)	2^{nd} Valley m (m_0)	$\alpha_{1^{st}}$ (eV^{-1})	$\alpha_{2^{nd}}$ (eV^{-1})
1L Electron	157	0.21	0.51	0.81	1.3	1.3
3L Electron	667	0.40	0.37	0.47	1.1	2.8
1L Hole	22	0.02	0.61	2.90	0.6	1.7
3L Hole	324	0.36	0.75	0.48	2.2	1.5

doi:10.6342/NTU202403452

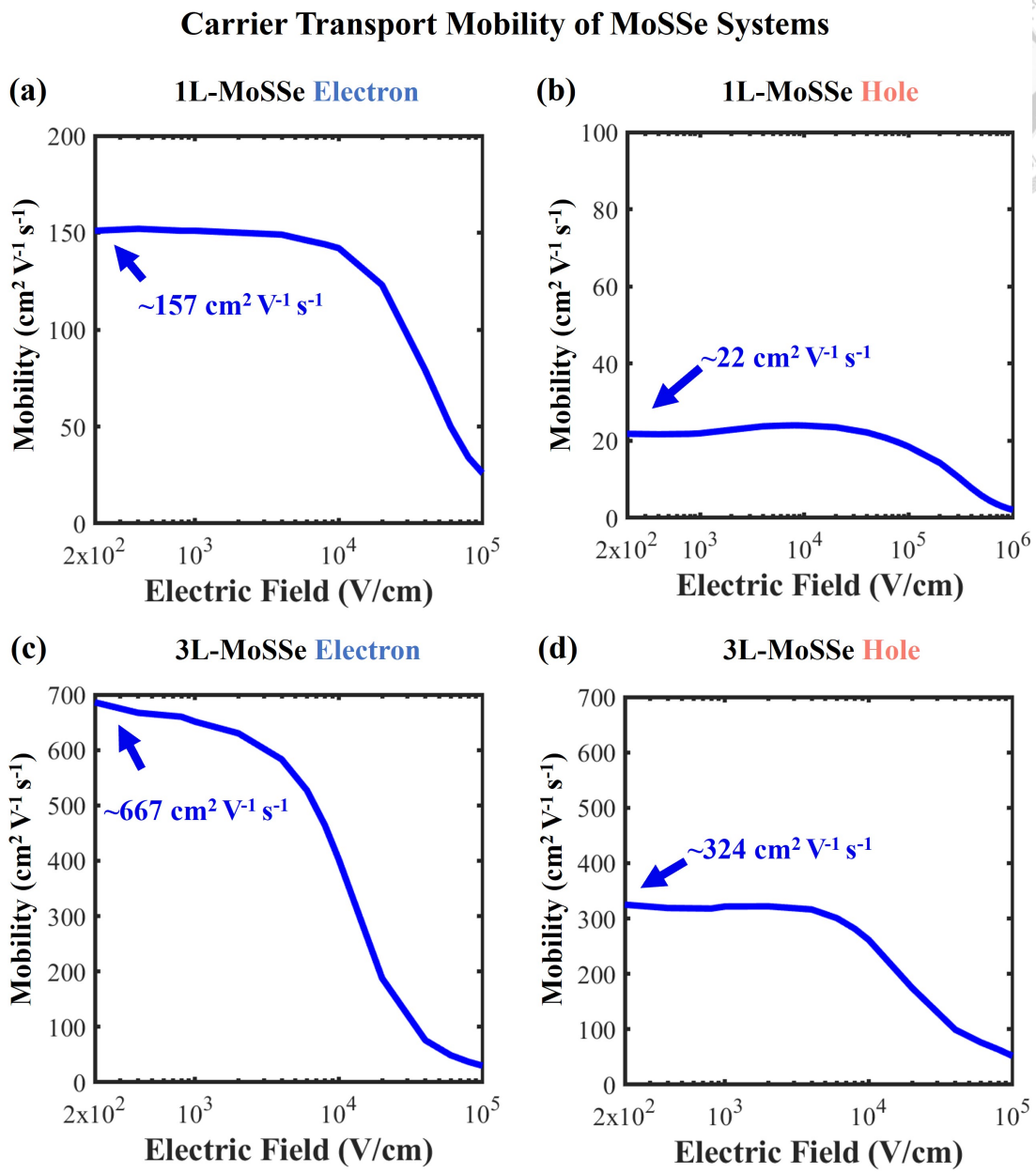

Figure 3.8: (a) and (b) Monte Carlo simulated electron and hole mobility of the 1L-MoSSe system. (c) and (d) Monte Carlo simulated electron and hole mobility of the 3L-MoSSe system.

and thereby improving mobility. Additionally, as MoSSe transitions to the 3L configuration, all effective masses decrease in both valleys, signifying a reduction in the 2D DOS. Fermi's golden rule states that the scattering rate is proportional to the 2D DOS. Thus, the reduction in 2D DOS lowers the scattering rate, further contributing to the mobility improvement. All in all, 3L-MoSSe shows better mobility compared to 1L-MoSSe.

doi:10.6342/NTU202403452

3.5 Absorption Properties of Mono-layer MoSSe

In the previous section, we discussed the fundamental transport characteristics of MoSSe, highlighting its suitability for electrical devices. However, the potential of MoSSe extends far beyond these applications. By leveraging the strong absorption coefficients and the intrinsic dipole of MoSSe, devices such as MoSSe abrupt pn-junctions can be developed [81]. These devices can exploit MoSSe's P_{sp} to enhance absorption efficiency. To further investigate the absorption properties of MoSSe, we employ first-principles methods to calculate the imaginary part of epsilon (ϵ_i), the joint density of states (JDOS), absorption coefficient, $\mathbf{E}_p$, and the band orbital contributions of 1L-MoSSe. A related discussion with results is given in the below subsections.

The band diagram calculated via Quantum Espresso utilizes a non-self-consistent field (NSCF) calculation, which calculates the missing **k**-point based on the previous self-consistent field calculation result (method shown in Fig. 2.2). Under typical conditions, the band structure's form would be little influenced by sampling the **k**-points, although not significantly. However, due to the delta function being represented by the Gaussian or Lorentzian function in the JDOS calculation, the difference between band-to-band energy offset and photon energy may cause an infinitesimal value, resulting in some missing point in the JDOS calculation. In epsilon.x calculation, these vanished points are made up through an inter-band broadening factor. This approach makes the calculation result less accurate when the NSCF sampling of the **k**-point is too coarse, resulting in most of the data being generated by broadening.

To address the "loosely sampled NSCF **k**-points causing JDOS point disappearance" issue, we calculated different NSCF sampling meshes and observed their effects on the

doi:10.6342/NTU202403452

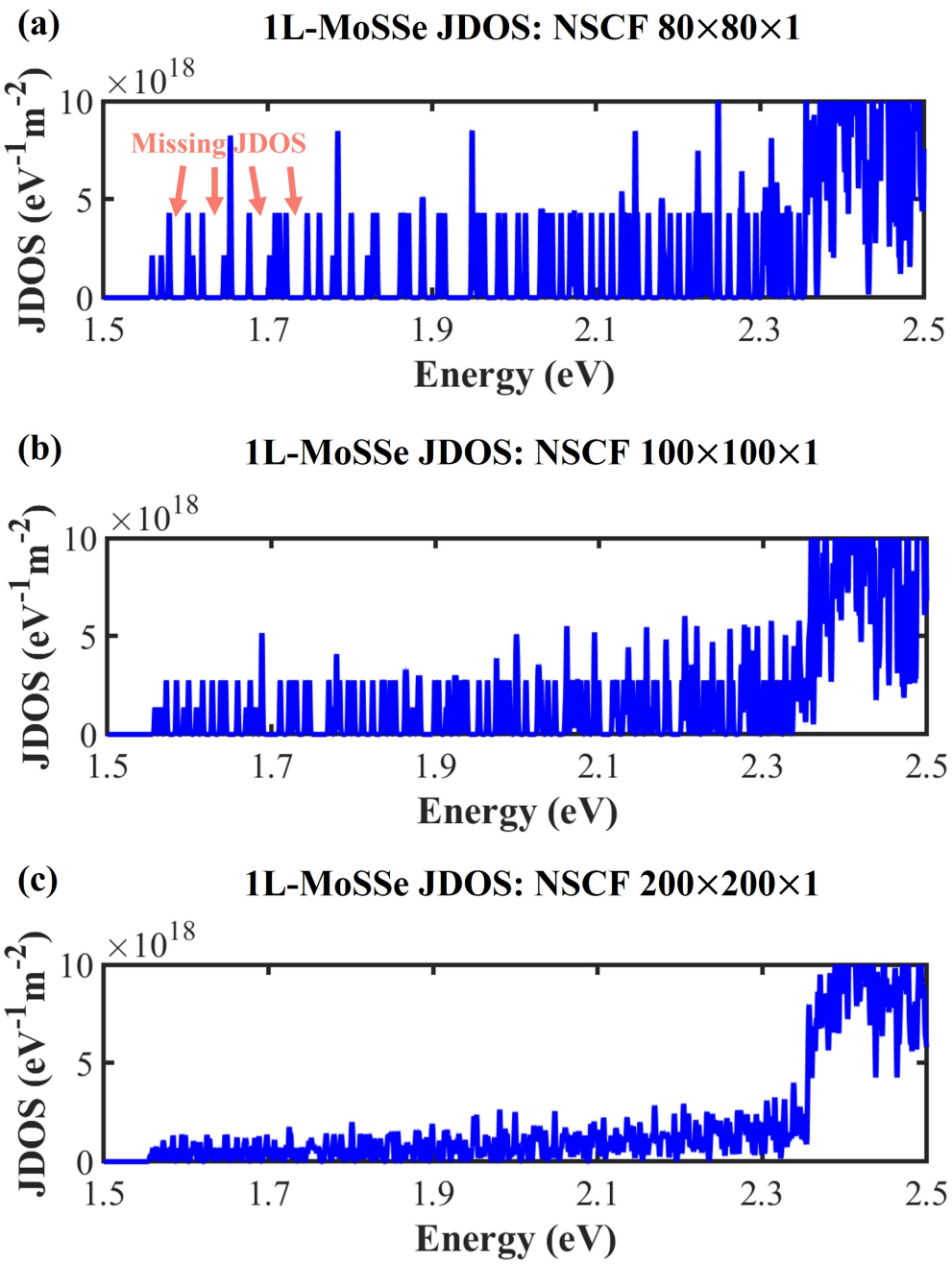

Figure 3.9: The comparison of DFT calculated JDOS versus photon energy plot with the 1L-MoSSe using a 0.001 eV broadening factor in an (a) 80×80×1, (b) 100×100×1, and (c) 200×200×1 NSCF **k**-mesh calculation.

JDOS calculations. We set the inter-band broadening factor to 0.001 eV to minimize its impact. Additionally, we set the photon energy sampling interval to 0.0001 eV to ensure that the photon energy and absorption transition energy do not differ excessively, preventing the generation of extremely small JDOS values. Figure 3.9 shows the calculated JDOS versus photon energy for three NSCF meshing densities: $80 \times 80 \times 1$, $100 \times 100 \times 1$, and

doi:10.6342/NTU202403452

$200 \times 200 \times 1$. As depicted in Fig. 3.9(a), the $80 \times 80 \times 1$ sampling shows many missing JDOS values, indicated by the red arrows, particularly near the band edge region (around 1.56 eV). When the meshing density increases to $100 \times 100 \times 1$, although some missing JDOS points are recovered, a few peak vacancies remain among the photon energies. Both cases indicate insufficient NSCF sampling points for accurate JDOS calculation. Conversely, with a high-density $200 \times 200 \times 1$ NSCF sampling, shown in Fig. 3.9(c), all peaks appear at each photon energy, demonstrating that this calculation is fundamentally more accurate than the previous two, as none of the JDOS data is purely generated through the inter-band broadening factor.

Even though each peak appears in the $200 \times 200 \times 1$ NSCF sampling, the convergence of the JDOS calculation under this circumstance is not certain. However, aimlessly increasing the mesh density in NSCF calculation is not a feasible approach, as the calculation becomes extremely resource-demanding (e.g., over 500 GB of storage is needed). Therefore, the band eigenvalue for each **k**-point is extracted from the $200 \times 200 \times 1$ mesh, and a linear interpolation method is employed to refine the 3D band diagram (Fig. 3.10(a)).

As shown in our calculations, after a small 0.005 eV broadening with interpolation, the JDOS calculation using 200 mesh sampling appears huge unreasonable flutter in the JDOS calculation. The calculations using a 400 mesh show a slightly smoother curve, however, there still exists a small shakiness in the curve as shown in the enlarged figure in Fig. 3.10(b). As the mesh sampling keeps on increasing to 1000 and 2000, both curves show a smooth curve with a good convergence compared with the theoretical JDOS value (see Eqn. (2.20)) at the band edge, as depicted in Fig. 3.10(b). The overlapping of the 1000 and 2000 mesh curves indicates the convergence of the interpolation. Thus, we concluded that the mesh density of $1000 \times 1000 \times 1$ is enough for JDOS to reach the theoretical

doi:10.6342/NTU202403452

2D JDOS value and good convergence. In summary, to accurately calculate the dielectric function using the DFT-RPA method, one must ensure a sufficiently fine NSCF mesh to avoid generating empty JDOS versus energy points. Additionally, band interpolation is recommended to ensure the calculation results match the theoretical 2D JDOS at the band edges.

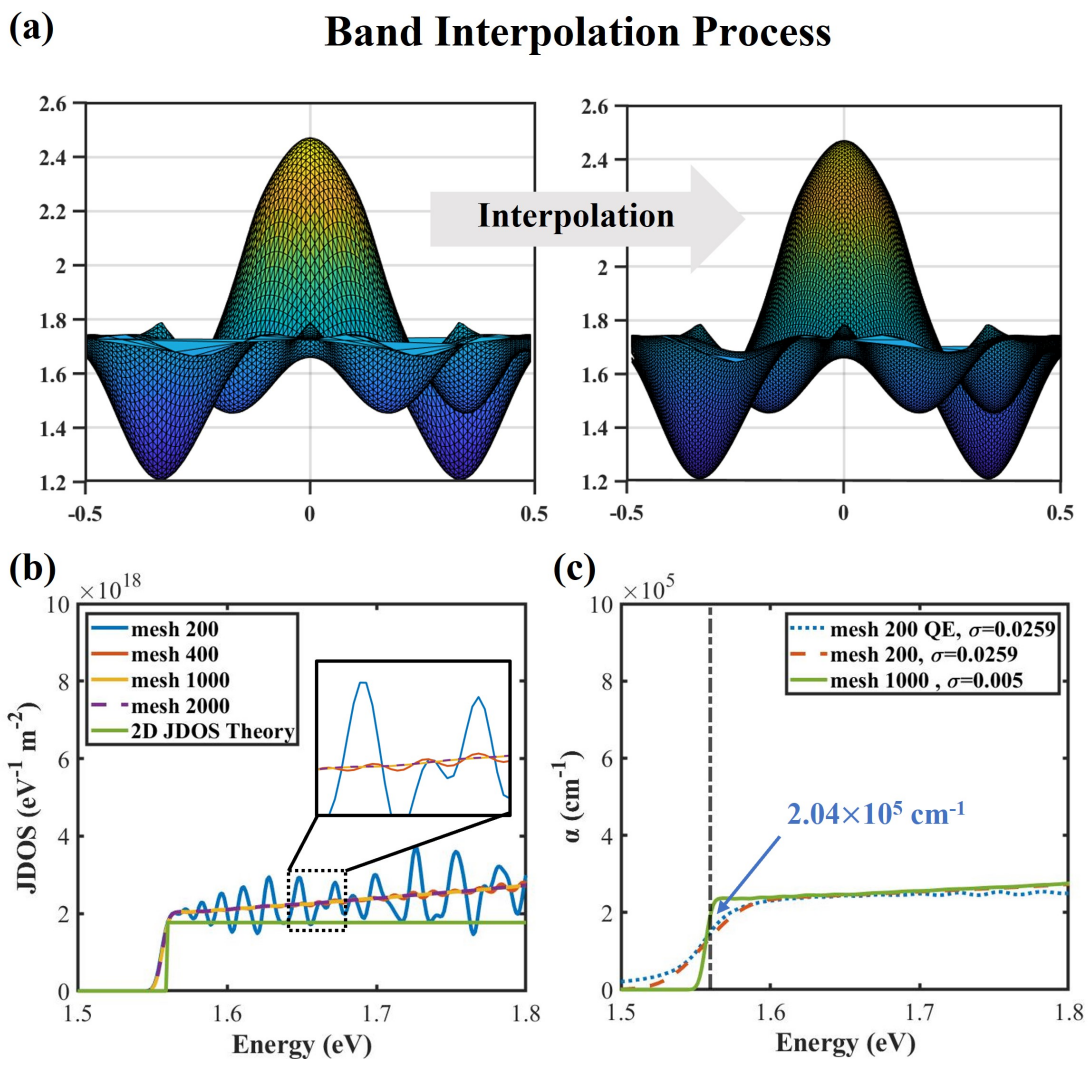

Figure 3.10: (a) Schematic of the band linear interpolation process. (b) The comparison between the theory 2D JDOS and the calculation result of different interpolation mesh sampling with a small broadening factor. (c) The 1L-MoSSe absorption coefficient α was calculated using 1000 mesh sampling JDOS. The $\mathbf{E}_p$ is first extracted using interpolated JDOS in the same condition. Then applied to the refined 1000 mesh JDOS to calculate α.

Figure 3.10(c) presents the absorption properties of 1L-MoSSe, calculated using the

doi:10.6342/NTU202403452

interpolation method after the NSCF utility in the Quantum Espresso package [86]. These calculations assume vertical transitions (optical approximation) where the **k** momentum is preserved, with intra-band transitions being negligible due to the relatively small momentum transfer by incoming/outgoing photons.

To obtain the $\mathbf{E}_p$ value, we fitted the epsilon.x calculated 200 mesh sample absorption coefficient (blue dotted line in Fig. 3.10(c)) with our absorption coefficient calculation using the same condition in JDOS interpolation calculation (red dashed line in Fig. 3.10(c)). The proximity of two lines indicates the rationality of $\mathbf{E}_p$, giving the extraction value of $\mathbf{E}_p$ = 26 eV. Then, by putting in the interpolated JDOS values and an extracted value of $\mathbf{E}_p$, we calculated the absorption coefficient in Fig. 3.10(c) using a finer mesh and a small broadening factor to obtain the correct value, which is the convergence case of the 1000 meshing JDOS in Fig. 3.10(b). Thus, the absorption coefficient at the band-gap is extracted to be 2.04×10^5 cm^{-1}, which is slightly lower than that of MoS_2 compared to the reference using similar approach [7] (about 2-3$\times 10^5$ cm^{-1}). This suggests that MoSSe exhibits slightly lower absorption performance compared to MoS_2. However, the absorption value that 1L-MoSSe has is still higher than the typical semiconductors such as Si, Ge, and GaAs at the band edge, showing its potential for optical applications [65]. The following Tab. 3.6 shows the extracted absorption-related parameter, which either the $\mathbf{E}_p$ or absorption coefficient can be further put into device simulation.

Table 3.6: The extracted absorption-related parameters near band edge for the 1L-MoSSe system.

Absorption-related Parameter	1L-MoSSe	Description
Eg	1.56 eV	Band Gap
m_r^*	$0.208m_0$	Reduced Effective Mass
α	$2.04 \times 10^5 cm^{-1}$	Absorption Coefficient
$\mathbf{E}_p$	26 eV	Energy Equivalents Deformation Constant

doi:10.6342/NTU202403452

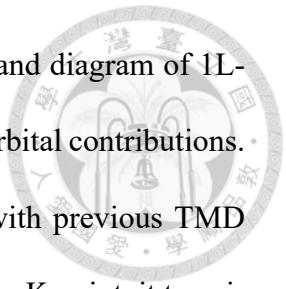

Figure 3.11 illustrates the DFT calculated orbital composition band diagram of 1L-MoSSe. The projected band plot in Fig. 3.11(a) shows the outermost orbital contributions. Mo's d orbitals dominate the band edge's composition, consistent with previous TMD studies [97]. When an electron is absorbed in the direct band gap at the K point, it transitions from an equal contribution of $d_{x^2-y^2}$ and d_{xy} orbitals in the valence band maximum to a predominantly d_{z^2} orbital in the conduction band minimum. These transitions ($d_{x^2-y^2}$ to d_{z^2} and d_{xy} to d_{z^2}) remain significant as the absorption shifts from the K point towards the Γ and M points, until leaving the K valley.

Figures 3.11(b) and 3.11(c) depict the band composition at the band edge corresponding to the energy difference ($E_c - E_v$) for the first conduction band and the last valence band, respectively, corroborating the aforementioned observations. Around the K point, the orbital contribution is dominated by 80% d_{z^2} in Ec and 40% each of $d_{x^2-y^2}$ and d_{xy} in Ev at the band gap energy. This indicates that extracted $\mathbf{E}_p$ near band edge in Tab. 3.6 is composited by the Hamiltonian between d_{z^2} with $d_{x^2-y^2}$ and d_{z^2} to d_{xy} . As the absorption transition moves away from the K point, the energy difference increases, resulting in a reduction of d_{z^2} by about 20% in Ec and 10% each for $d_{x^2-y^2}$ and d_{xy} in Ev. To compensate for this decrease, d_{z^2} in Ev increases from zero to nearly 15%, while $d_{x^2-y^2}$ and d_{xy} in Ec each rise by approximately 10%, as the transition approaches from the K to the Q and M points. This suggests that an additional independent transition, or second $\mathbf{E}_p$, might be required beyond the 2.3 eV energy transition to describe the absorption phenomenon in higher energy regions.

doi:10.6342/NTU202403452

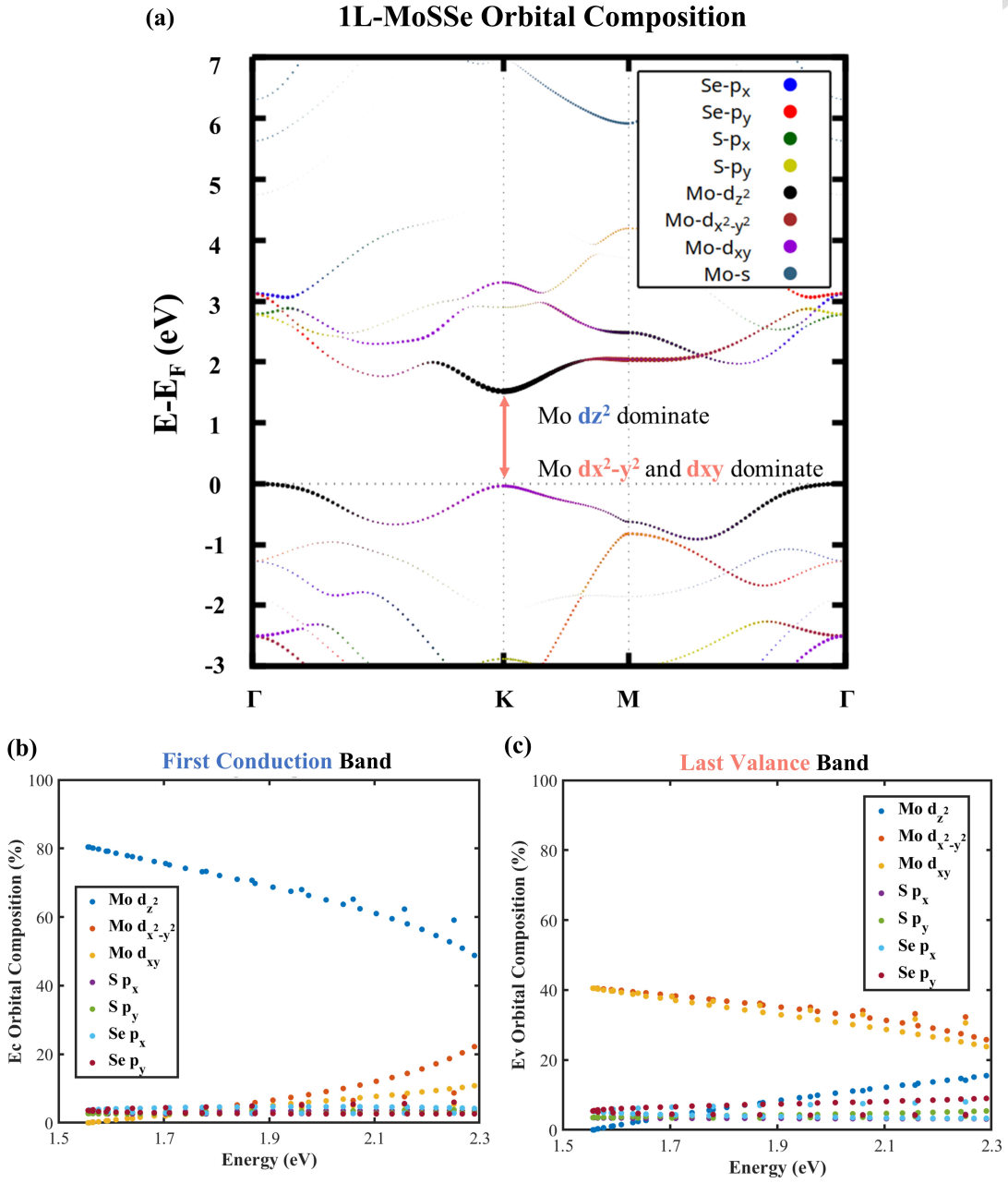

Figure 3.11: (a) Projected band of 1L-MoSSe with the orbital composition information. (b) Orbital contribution versus Ec-Ev energy difference of the first conduction band in 1L-MoSSe. (c) Orbital contribution versus Ec-Ev energy difference of the last valance band in 1L-MoSSe.

doi:10.6342/NTU202403452

Chapter 4

MoSSe Complementary Metal-Oxide-Semiconductor Field-Effect Transistor Design and Simulation

4.1 Device Conceptualization and Simulation Parameter

Figure 4.1 shows a double-gate CMOSFET structure and schematic that takes use of MoSSe's strong intrinsic dipole characteristics. The process of creating a P-MOSFET involves attaching two metal electrodes to the S face to form a p-type source and drain regions, as shown to the left of the black dashed line. After the oxide and gate have been set vertically, the remaining MoSSe region between them functions as a channel area. Similar steps may be taken to build an N-MOSFET, as shown to the right of the dotted line. The only difference is that metals are connected to the Se face in this instance instead of the S face near the source and drain. Two benefits of this horizontal CMOSFET architecture are:

doi:10.6342/NTU202403452

Because only a single channel of material is needed to generate n- and P-MOSFETs, the Janus MoSSe (1) simplifies the process of material selection and (2) allows layer-by-layer development throughout the manufacturing process, increasing the process reliability.

Table 4.1: The JTMD MOSFET simulations' input parameters. The MoSSe-related variables are represented by the values in the first section of the table, while the oxide parameters are found in the second section. Using DFT, all MoSSe parameters are derived. In 2D DDCC, the parameters SiO_2 and Al_2O_3 are intrinsically provided. This work has been published in [3].

Parameter	Numerical value	Description
E_g	1.212 eV	MoSSe Average band gap
E_{ea}	3.97 eV	MoSSe Electron affinity
μ_e	667 $cm^2/(V{\cdot}s)$	MoSSe Electron mobility
μ_h	324 $cm^2/(V{\cdot}s)$	MoSSe Hole mobility
$m^*_{e,K}$	$0.37m_0$	MoSSe Electron K-valley effective mass
$m^*_{e,Q}$	$0.47m_0$	MoSSe Electron Q-valley effective mass
$m^*_{h,\Gamma}$	$0.75m_0$	MoSSe Hole Γ-valley effective mass
$m^*_{h,K}$	$0.48m_0$	MoSSe Hole K-valley effective mass
$\epsilon_{\|\|}$	$15.93\epsilon_0$	MoSSe In-plane dielectric constant
$\epsilon_\perp$	$6.31\epsilon_0$	MoSSe Out-of-plane dielectric constant
P_{sp}	4.76×10^{13} cm^{-2}	MoSSe Spontaneous polarization
E_{g,SiO_2}	9.0 eV	SiO_2 band gap
E_{g,Al_2O_3}	8.9 eV	Al_2O_3 band gap
E_{g,HfO_2}	5.8 eV	HfO_2 band gap [98]
E_{ea}	0.95 eV	SiO_2 Electron affinity
E_{ea}	1.50 eV	Al_2O_3 Electron affinity
E_{ea}	2.70 eV	HfO_2 Electron affinity [98]
ϵ_{SiO_2}	$3.9\epsilon_0$	SiO_2 dielectric constant
$\epsilon_{Al_2O_3}$	$9.3\epsilon_0$	Al_2O_3 dielectric constant
ϵ_{HfO_2}	$25\epsilon_0$	HfO_2 dielectric constant [99]

The 2D DDCC solver simulates device characteristics to examine the device-related properties of the developed MoSSe MOSFETs. Since the 5-nm channel thickness of MoSSe guarantees enough carrier flow in the channel area, we used this thickness to create our device to simulate MoSSe multi-layers. Table 4.1 contains all of the parameters utilized in the 2D DDCC simulation. We show that even under the most extreme metal selection conditions, n- and p-type contact generation may occur by placing the metal work function setup near the mid-gap of the MoSSe in the device's contact. Although the 5-nm

doi:10.6342/NTU202403452

MoSSe corresponds to approximately 6 layers of MoSSe, the metal on both sides will pin the MoSSe's conduction and valence band edge, limiting the effect of P_{sp}. Thus, we used the P_{sp} value before screening phenomenon in DFT (i.e., 3L-MoSSe) as the representative value in the MoSSe channel.

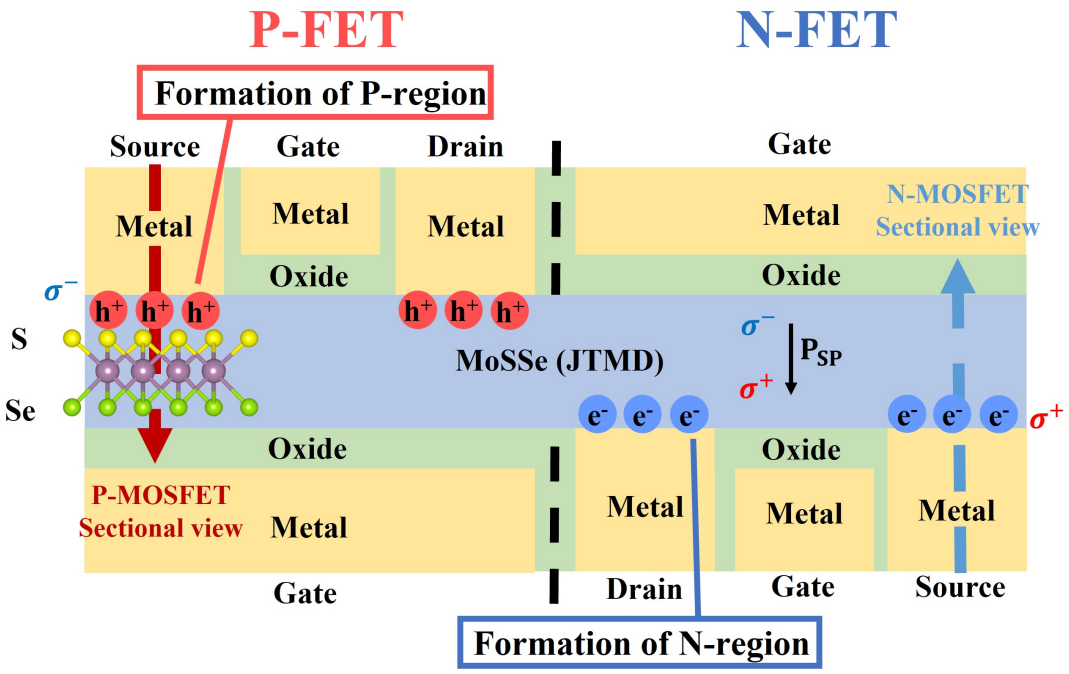

Figure 4.1: The illustration of 2D MoSSe JTMD CMOSFET device design. This work has been published in [3].

4.2 Spontaneous Polarization Effect on Band Diagram

For the dashed arrows denoted in the Fig. 4.1, the corresponding cross-sectional images of the energy band diagram are displayed in Figs. 4.2(a) and 4.2(b) for the p- and N-MOSFETs cross-section, respectively. Similar to partial positive and negative charges, the strong P_{sp} in the MoSSe vertically attracts electrons and holes. At the MoSSe region interface, a negative polarization charge causes the Ec and Ev band to pull the Ec and Ev upward (Fig. 4.2(a)) and to bend lower (Fig. 4.2(b)). This band-edge bending from P_{sp} is

doi:10.6342/NTU202403452

crucial for enabling Ohmic contact generation in the device, which is consistent with the previously described DFT computations. Here, the variation in sign of P_{sp} simply correlates to the disparity in physical behavior among the opposite sides of MoSSe attachment.

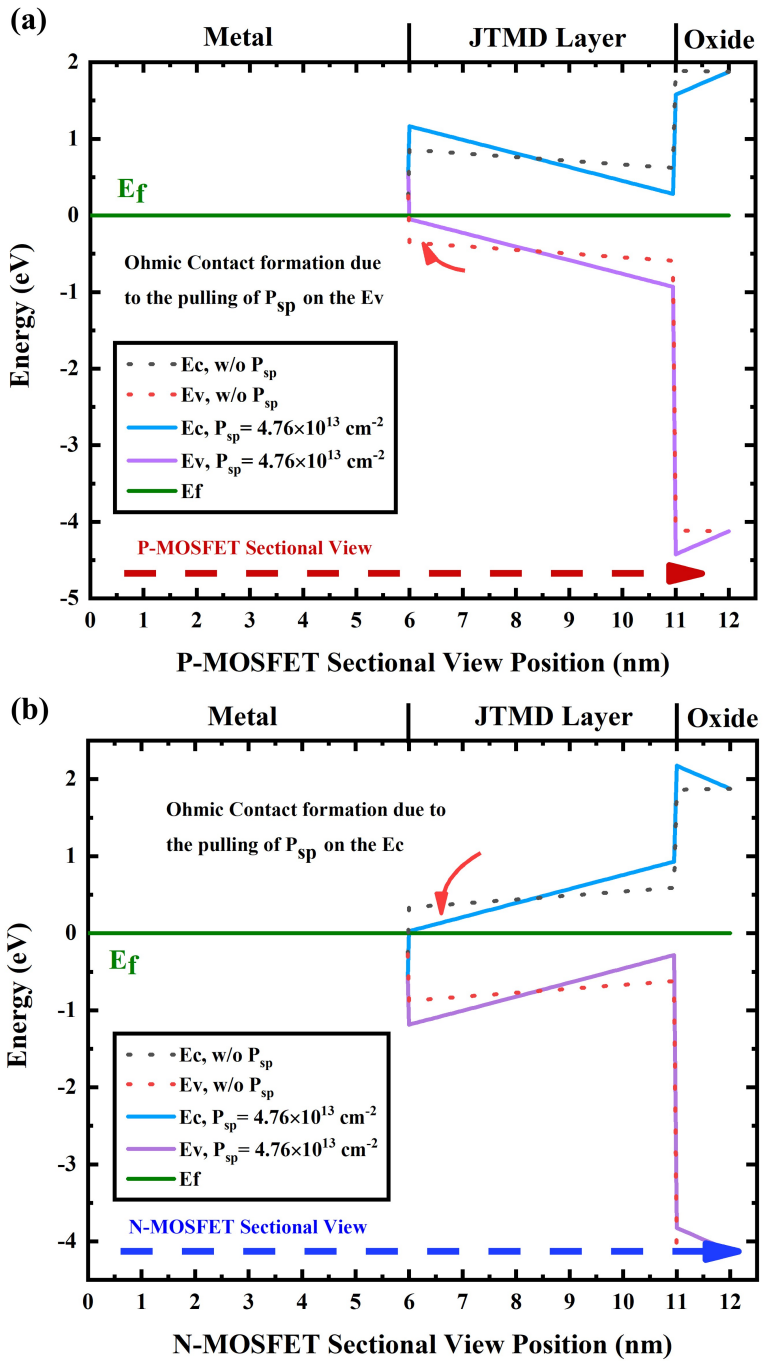

Figure 4.2: (a) P-MOSFET and (b) N-MOSFET energy band sectional-view diagrams. The solid and dash lines compare the band diagram with and without P_{sp} from source metal to gate, respectively. This work has been published in [3].

On the contrary, the same device structure is used to simulate TMDs without this

doi:10.6342/NTU202403452

inherent dipole, where P_{sp} is changed to 0 (dot lines marked "w/o P_{sp}"). When P_{sp} is not there, there is insufficient Ohmic contact creation, which leads to a Schottky barrier at the contact region due to the lack of the band-bending effect.

4.3 Effect of Gate Design

The I-V characteristics of several MoSSe MOSFET designs are now investigated. Figure 4.3(a) shows a single-gate design with gate length $L_g = 1$ μm, which is a common dimension adopted in experimental studies of FETs based on 2D materials [62, 67]. Device modifications such as the use of double gates (Fig. 4.3(b)) and smaller dimensions (Fig. 4.3(c)) are also simulated. The addition of the second gate can decrease the minority carrier concentration on the other side of the channel interface since the gate metal will inhibit the P_{sp} effect on the potential, aiding the formation of the majority carrier in the channel region. The simulations for all devices assume an HfO_2 gate oxide of thickness $t_{\text{ox}} = 1$ nm.

Figure 4.4 shows the transfer characteristics (I_{ds}-V_g) of the MOSFETs from Fig. 4.3(a) to Fig. 4.3(c), where the transfer curve results are shown in Fig. 4.4(a) for P-MOSFET and Fig. 4.4(b) for N-MOSFET. The curves with squares, circles, diamonds, and stars correspond to the N-MOSFETs in Fig. 4.3(a), Fig. 4.3(b), Fig. 4.3(c) with $L_g = 200$ nm and Fig. 4.3(c) with $L_g = 50$ nm, respectively.

The key distinction lies in the opposite orientation of P_{sp} in the JTMD layer. The typical I_{ds}-V_g curves for the n- and P-MOSFETs indicate that all three devices exhibit satisfactory enhancement-mode MOSFET behavior. Among the three devices, the single-gate design (Figure 4.3(a)) has the most significant subthreshold swing (SS) and the lowest

doi:10.6342/NTU202403452

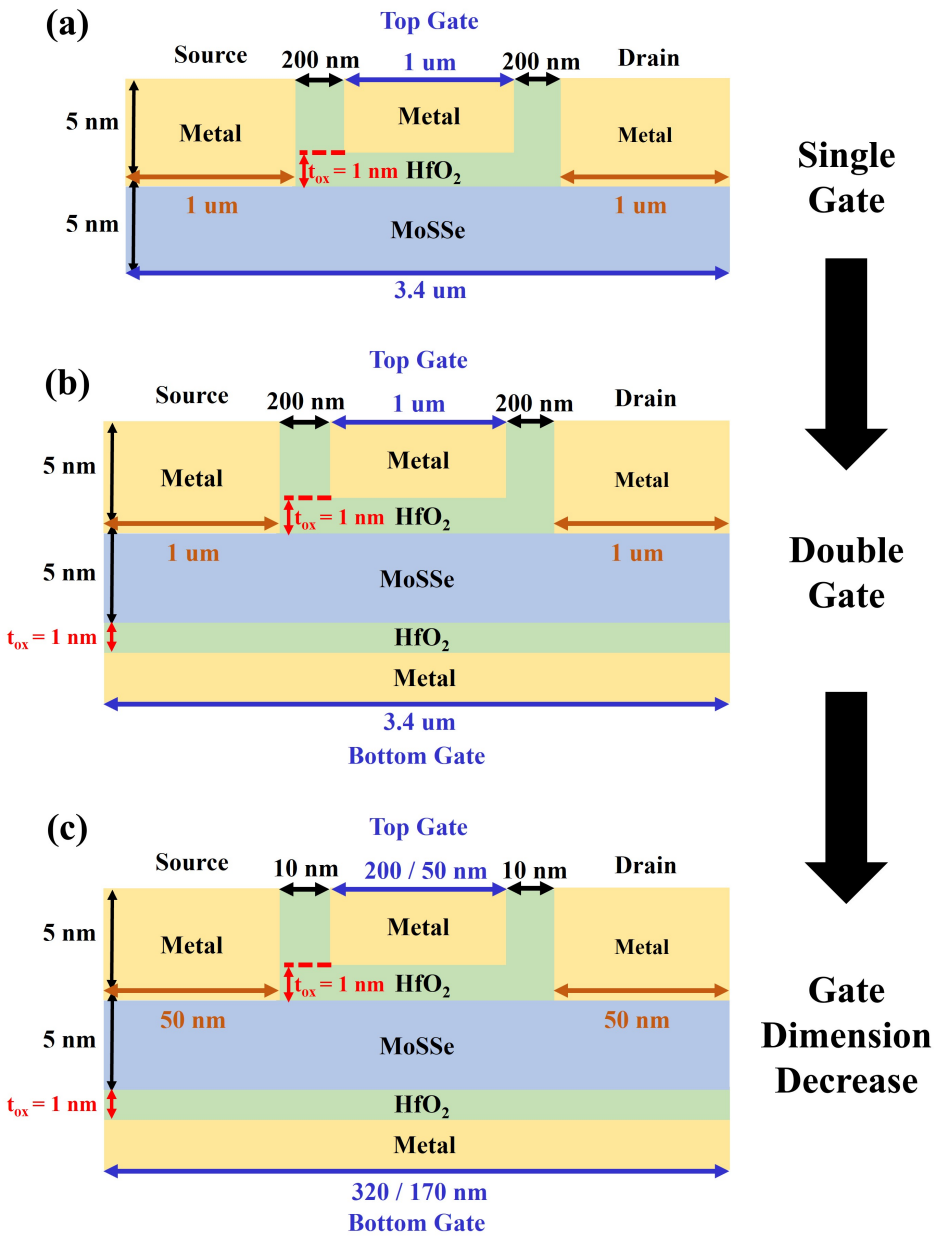

Figure 4.3: (a) and (b) Layouts of the key device dimensions and $L_g = 1$ μm structure of single- and double-gate MoSSe MOSFET devices, respectively. (c) Double-gate MoSSe MOSFET layout diagram, where $L_g = 200$ and $L_g = 50$ nm. This work has been published in [3].

ON current I_{ON}. When a bottom gate is added (Figure 4.3(b)), the SS drops to around 60.5 mV/dec, while I_{ON} increases by an order of magnitude, indicating an improvement in gate control. Having shown that both designs are feasible at a larger scale, we reduce the horizontal scale of the double-gate design to $L_g = 200$ and $L_g = 50$ nm (Figure 4.3(c)) to examine the device performance at a smaller scale. The decrease of the SS values in the

doi:10.6342/NTU202403452

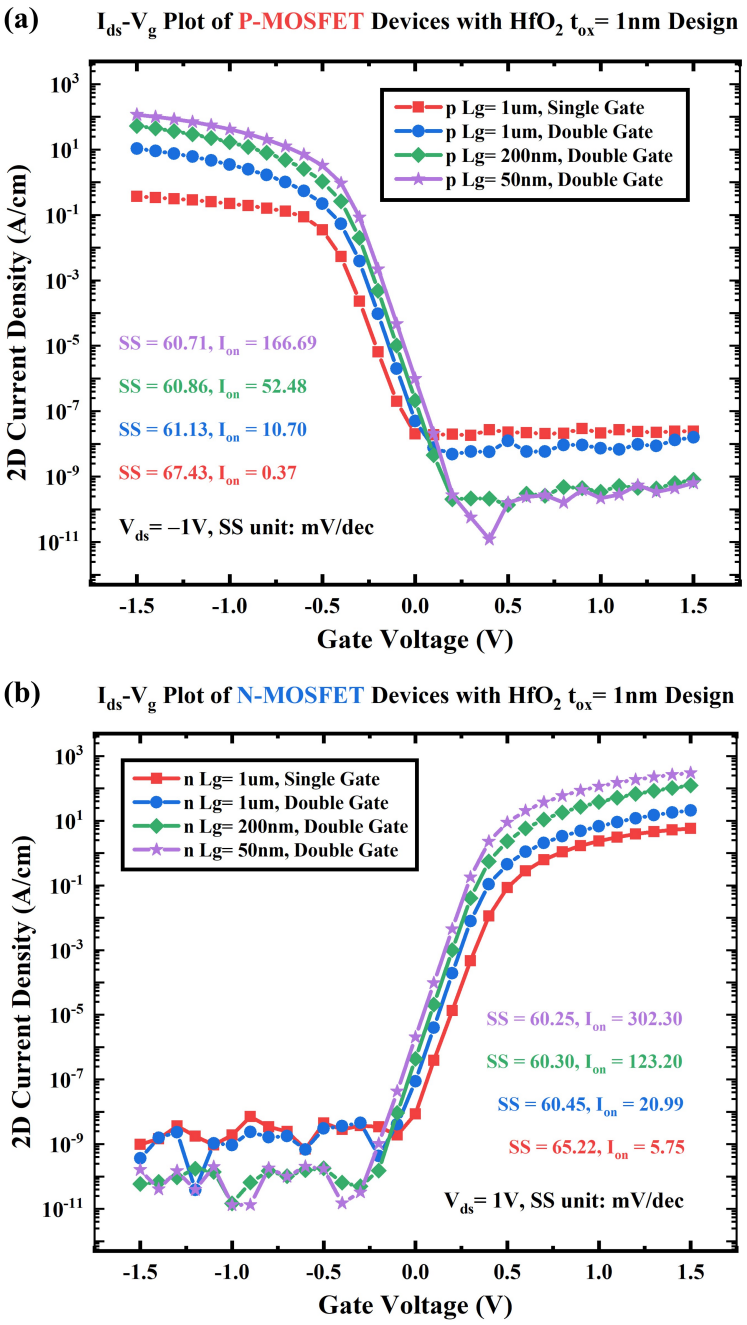

Figure 4.4: The plots of I_{ds}-V_g for P- and N-MOSFET, respectively, using the designs displayed in Figs. 4.3(a)–(c) for both polarities of the MOSFET, featuring a $t_{\text{ox}} = 1$ nm HfO_2 oxide thickness. Parameters are given in Table 4.1. This work has been published in [3].

N-MOSFET suggests that reducing L_g to 200 nm or even to 50 nm would significantly enhance the control of the gate in this design, resulting in a decrease in SS. In addition, I_{ON} is increased by an order of magnitude compared with that of the larger-scale device, while the OFF-state current I_{OFF} is decreased by about an order, indicating an improvement in

doi:10.6342/NTU202403452

I_{ON}/I_{OFF}. All of these results show that the SS and ON- or OFF-current characteristics of the designs considered are those of a typical MOSFET device. The lower SS and higher I_{ON} consistently observed for all the N-MOSFETs compared with the corresponding P-MOSFETs may originate from the slightly higher mobility of electrons compared with holes.

4.4 Effect of Equivalent Oxide Thickness

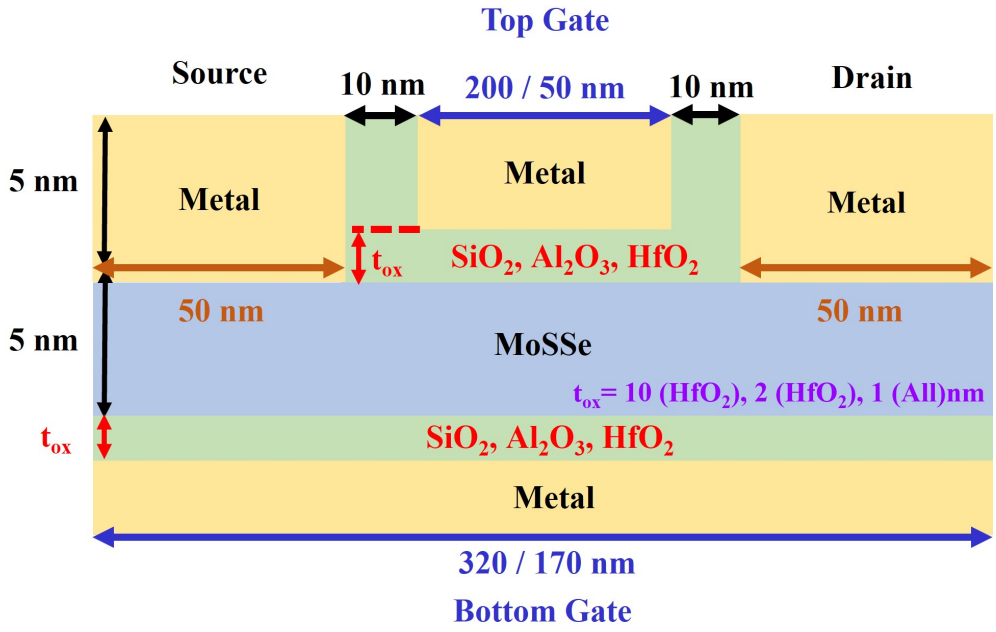

Figure 4.5: Design of a double-gate MoSSe MOSFET with $L_g = 200$ and 50 nm, using several oxides with varying EOT values.

A CMOSFET requires an enhancement-mode MOSFET to work correctly. The gate oxide thickness, t_{ox}, determines a MOSFET's operating mode. The ideal device arrangement in terms of equivalent oxide thickness (EOT) was determined by evaluating several oxides and t_{ox} values, as illustrated in Fig. 4.5. Figures 4.6 and 4.7 illustrate the findings for both MOSFET polarity with $L_g = 200$ nm and 50 nm design, accordingly. Here, we define ON or OFF state switching as $I_{ON}/I_{OFF} > 10^3$.

doi:10.6342/NTU202403452

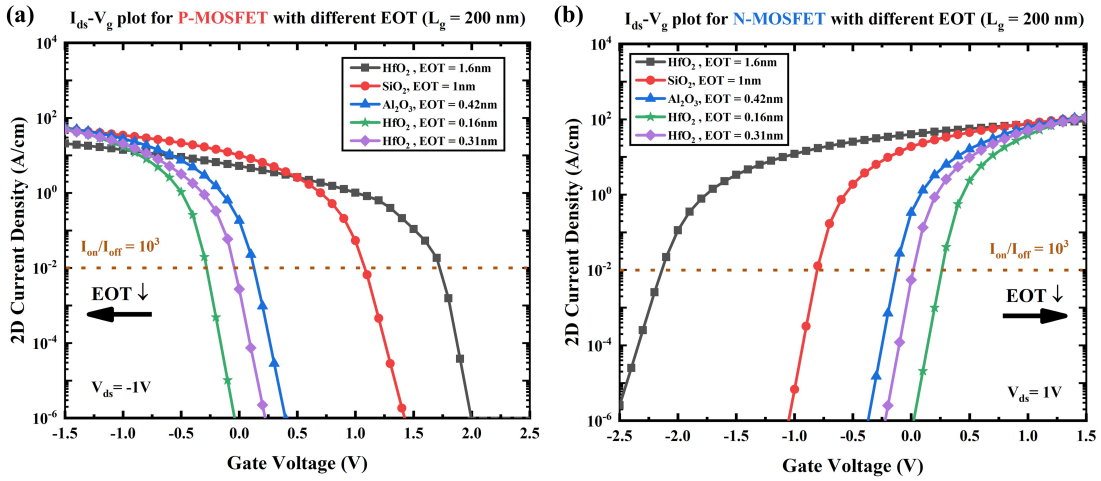

Figure 4.6: (a) and (b) I_{ds}-V_g plots for $L_g = 200$ nm design of p- and N-MOSFETs, respectively, with different values of EOT. $t_{\text{ox}} = 1$ nm for all oxides, and, in addition, results for designs with $t_{\text{ox}} = 2$ and 10 nm are also shown for HfO_2. The parameters are given in Table 4.1. This work has been published in [3].

Firstly, we investigate the impact of different EOT values on the electrical performance of transistors with a longer channel length of $L_g = 200$ nm in small-scale designs (Figure 4.5). A SiO_2 oxide gate with a thickness of 1 nm is tested, and the I_d-V_g result is illustrated by the curve of red circles. The device is obviously in the ON state ($I_d \sim 90$ A/cm^2) when no gate bias is applied, suggesting that the MOSFET is a depletion-mode device. To determine the threshold EOT at which the device changes to enhancement mode, we minimize the EOT by selecting an Al_2O_3 gate with $t_{\text{ox}} = 1$ nm (EOT = 0.42 nm, blue triangles). However, the current stays on the order of 10^1 A/cm^2 at $V_g = 0$ V, and both polarities remain in the depletion state. To reduce the EOT of MOSFETs, a high-κ substance, HfO_2, is used. Using HfO_2 with $t_{\text{ox}} = 1$ nm (EOT = 0.16 nm, green stars) produces a better enhancement-mode device for both P-MOSFETs and N-MOSFETs. Next, we tune the t_{ox} of the HfO_2 to 2 nm (EOT = 0.31 nm, purple diamonds) to avoid current flowing across the thin gate oxide. Figs. 4.6(a) and 4.6(b) show that the I_d-V_g curves for this optimized value of t_{ox} meet the OFF state brown dashed line at $V_g = 0$ V, suggesting that the enhancement mode is preserved even as the EOT increases. The findings for

doi:10.6342/NTU202403452

HfO_2 with $t_{ox} = 2$ nm indicate that the EOT crossover between depletion and enhancement modes in the present MOSFET architecture is 0.31 nm. The best MOSFET design based on HfO_2 with $t_{ox} = 2$ nm results in a SS of about 63 mV/dec, as shown in Figs. 4.6 for the $L_g = 200$ nm design.

Since such low-t_{ox} devices may encounter several processing difficulties, simulation results for a more easily fabricated thick HfO_2 gate with $t_{ox} = 10$ nm (EOT = 1.6 nm, black squares) are also given in Figs. 4.6(a) and 4.6(b). Owing to the increased EOT, both the p- and n-type MOSFETs exhibit the depletion mode in terms of transfer characteristics, where both the I_{ON} drops and the device turns off at 1.8 V and -2.1 V for p- and N-MOSFETs, respectively.

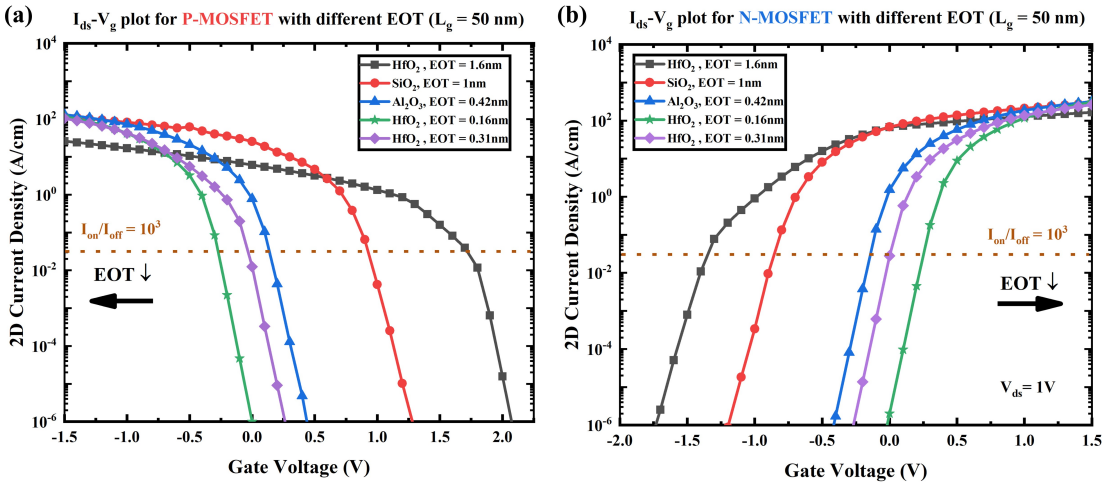

Figure 4.7: (a) and (b) I_{ds}-V_g plots for $L_g = 50$ nm design of p- and N-MOSFETs, respectively, with different values of EOT. $t_{ox} = 1$ nm for all oxides, and, in addition, results for designs with $t_{ox} = 2$ and 10 nm are also shown for HfO_2. The parameters are given in Table 4.1.

Here, a similar result is also presented as the L_g is shortened to 50 nm. The optimal MOSFET design remains the same as in the $L_g = 200$ nm case, where the mode switching between depletion and enhancement mode occurs at an EOT of 0.31 nm. Due to the shorter channel, the SS in the HfO_2 design with $t_{ox} = 2$ nm improves slightly, decreasing to

doi:10.6342/NTU202403452

62 mV/dec. Additionally, all I_{ON} values experience a slight increase during the ON state. Both results indicate an overall enhancement in the device performance as scaling down to $L_g = 50$ nm scenario. However, since the gate dimensions of the $L_g = 50$ nm device are relatively small, the lack of quantum effect consideration in our simulation model might lead to slightly inaccurate performance results. Thus, the $L_g = 50$ nm device in Figs. 4.7 serves as a simple inspection of the device scaling phenomenon. Overall, the I-V plots demonstrate the possibility of creating a workable MOSFET even with larger values of t_{ox} and provide a reference for future experimental studies.

To observe why a decrease in EOT causes a significant drop in I_{ON} current for P-MOSFET at $V_g = -1.5$ V (Fig. 4.6(a), for instance) between the devices with EOT = 0.16 nm (1 nm HfO_2) and EOT = 1.6 nm (10 nm HfO_2), we plot the majority carrier horizontal cross-section for P-MOSFET in the $L_g = 200$ nm design for both devices in Figure 4.8(a). The horizontal cross-section position in the MoSSe channel is about 0.1 nm next to the channel's top gate/oxide interface. As depicted in Fig. 4.8(b), the low EOT device (blue line) exhibits a high carrier concentration in both the source and drain contact regions, suggesting that the contact resistance (R_c) is lower compared to the high EOT device (red line). The lower R_c implies that less voltage drop occurs when the carrier flows through the contact, resulting in a greater I_{ON} current. Conversely, a low hole concentration produces a higher R_c, degrading the I_{ON} current and consequently the device's performance in higher EOT circumstances.

Additionally, the EOT also affects the amount of 2DHG in the channel, becoming a secondary reason for the decreasing I_{ON}. We compare the 2DHG values at three channel positions to illustrate this phenomenon: near the source (Fig. 4.8(a), Point A), middle (Fig. 4.8(a), Point B), and near the drain (Fig. 4.8(a), Point C). Take Point A as an example,

doi:10.6342/NTU202403452

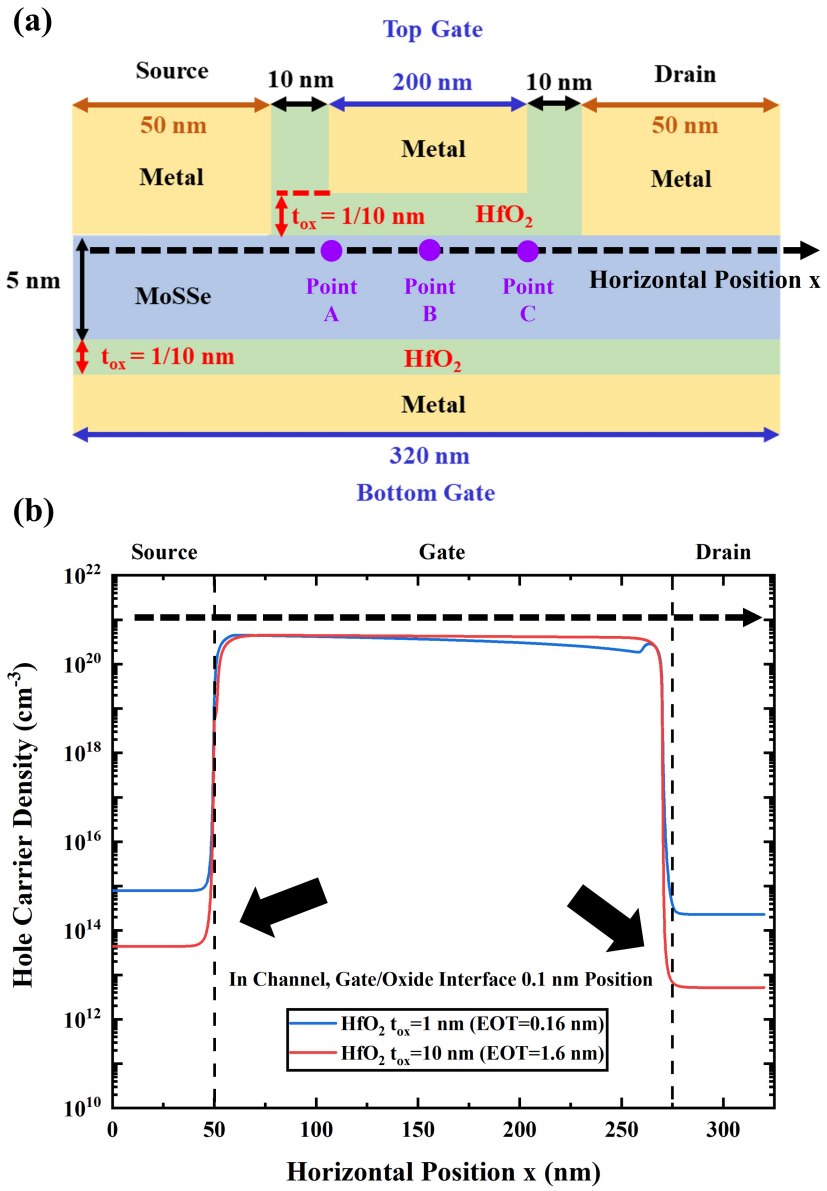

Figure 4.8: (a) Lg= 200 nm P-MOSFET with EOT = 0.16 nm and 1.6 nm. The channel horizontal cross-section is shown by the black dash arrow and the 2DHG comparison point A, B, and C are indicated in purple dots. (b) Log scale Hole concentration density in P-MOSFETs channel horizontal cross-section with EOT = 0.16 nm and 1.6 nm. The concentration drop in the source and drain (black arrow) causes the increase in R_c, thus I_{ON} drops.

the EOT = 0.16 nm channel has a 2DHG value of $4.7 \times 10^{13}\,\mathrm{cm}^{-2}$, whereas the EOT = 1.6 nm channel has $2.6 \times 10^{13}\,\mathrm{cm}^{-2}$ 2DHG (Low EOT to high EOT 2DHG ratio = 1.79). A similar outcome is observed at the other two points, with low EOT to high EOT 2DHG ratios of 1.55 and 1.20 for Point B and Point C, respectively. The lower EOT enables stronger gate control, leading to slightly higher 2DHG formation, resulting in

doi:10.6342/NTU202403452

lower resistance in the channel and thus higher I_{ON}. In summary, R_c is the primary reason for the I_{ON} drop in high EOT devices. The reduction in 2DHG in high EOT circumstances may also slightly contribute to this I_{ON} degradation phenomenon.

4.5 Effect of Spontaneous Polarization

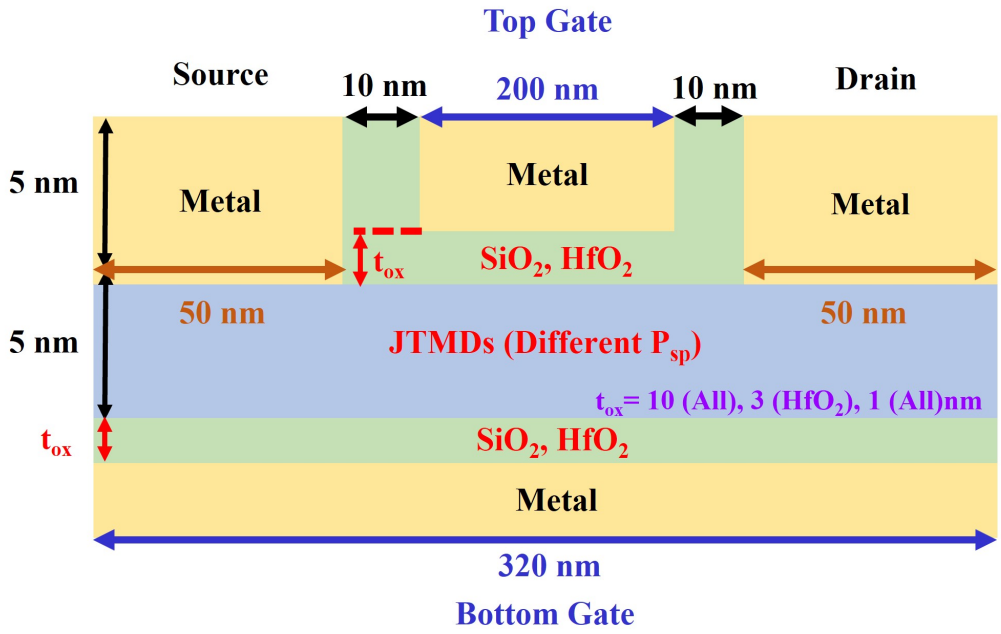

Figure 4.9: Diagram MoSSe MOSFET with several chosen JTMDs and oxides with various P_{sp} and EOT numbers, correspondingly.

The effect of P_{sp} on the carrier accumulation phenomena in the MoSSe channel area should also be considered. We compute the two-dimensional electron gas (2DEG) in an N-MOSFET device having a 200-nm channel in length. as shown in Fig. 4.9, for a range of assuming P_{sp} values, from 1×10^{13} to 5×10^{13} cm^{-2}, to investigate the effect of the intrinsic dipole's magnitude on the efficiency of the device. The amount of P_{sp} impacts the device's 2DEG, and these P_{sp} values may be thought of as JTMDs with varying inherent dipole strengths. As typical low-κ and high-κ gate oxides for this investigation, SiO_2 ($t_{ox} = 1$ and 10 nm) and HfO_2 ($t_{ox} = 1, 3$, and 10 nm) were chosen. To separate the influence

doi:10.6342/NTU202403452

of P_{sp}, the computations were carried out with zero bias, equivalent to the equilibrium condition.

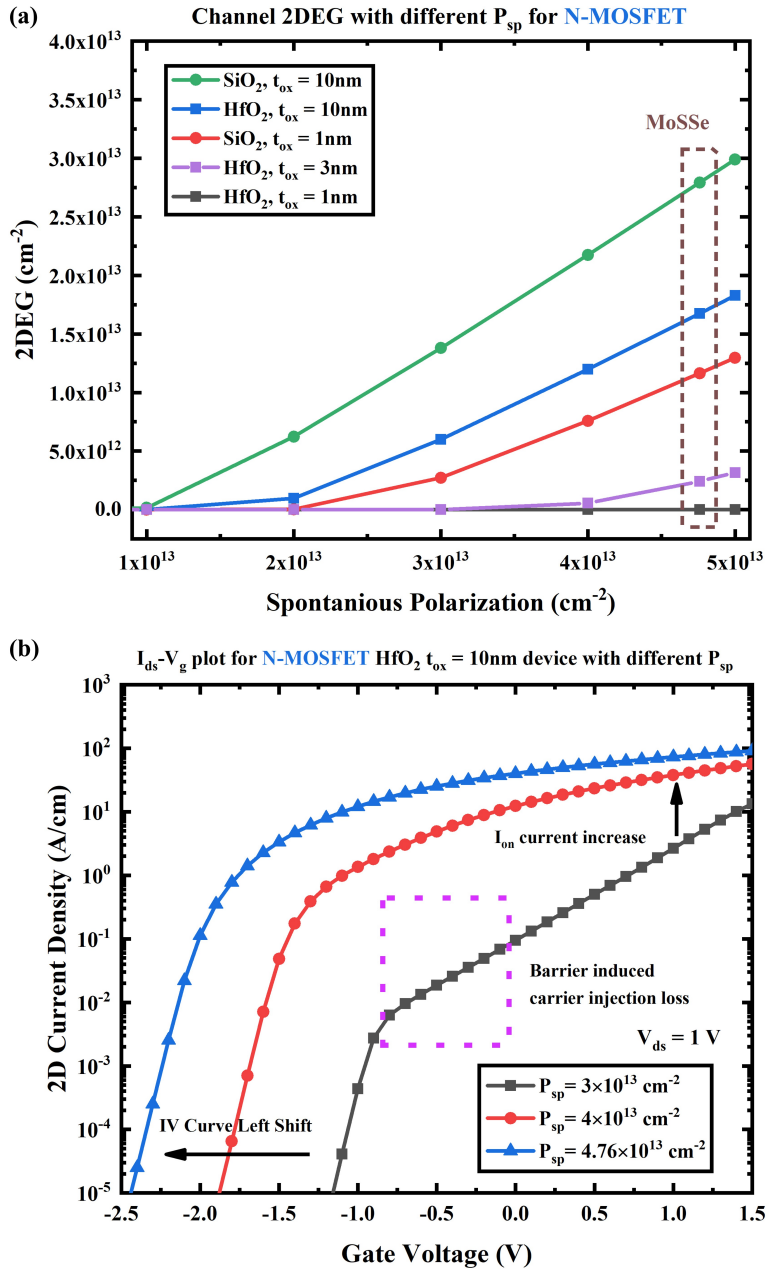

Figure 4.10: (a) 2DEG in channel vs linear scale P_{sp} magnitude diagram for N-MOSFETs. (b) Plot of I_{ds}–V_g for N-MOSFET HfO_2 with the $t_{ox} = 10$ nm design device, to comparison with distinct P_{sp}. This work has been published in [3].

Figure 4.10(a) shows how P_{sp} affects the concentration of 2DEG. When P_{sp} increases, the 2DEG increases almost linearly for situations with high EOT (SiO_2, $t_{ox} = 10$ nm). This linearity occurs because the explored P_{sp} interval (1×10^{13} -5×10^{13} cm^{-2}) permits

doi:10.6342/NTU202403452

carriers to attain saturation due to the large EOT. On the other hand, the linear region's onset moves towards greater P_{sp} values as EOT reduces. The linear zone, for example, starts at 2×10^{13} cm^{-2} for HfO_2 at $t_{ox} = 10$ nm and 3×10^{13} cm^{-2} with SiO_2 having a $t_{ox} = 1$ nm. To achieve enhancement-mode devices, one can use the P_{sp} value to signal when the linear regime starts. With $t_{ox} = 1$ nm in the HfO_2 design, the linear regime begins beyond 5×10^{13} cm^{-2} due to the lowest EOT. This suggests that because of its originally low 2DEG concentration, MoSSe (illustrated in brown dotted box) can work in enhanced mode. However, when the HfO_2 thickness is increased to 3 nm, the EOT is raised and the linear region starts at 4×10^{13} cm^{-2}. Because of the greater initial 2DEG concentration, this points to a depletion-mode response for MoSSe as HfO_2's $t_{ox} = 3$ nm.

P_{sp} has an impact on MOSFETs' *I-V* properties as well. We studied devices on P_{sp} values such as 3×10^{13}, 4×10^{13}, and 4.76×10^{13} cm^{-2}, all constructed with a 10 nm HfO_2 gate oxide , to illustrate its effect on the linear 2DEG region. Raising P_{sp} causes the transfer *I-V* curve to shift towards higher negative voltages, as Figure 4.10(b) illustrates. This shift suggests that to exhaust the greater amount of 2DEG in the channel, a higher gate voltage is required. Moreover, an increase in P_{sp} results in a larger electron concentration, which raises the ON current (I_{ON}).

Furthermore, P_{sp} may affect the contacts' carrier injection. The device displays a bigger g_m value for P_{sp} values of 4.76×10^{13} and 4×10^{13} cm^{-2}, as a result of decreased contact resistance. The purple dotted box indicates non-ideal *I-V* curves near saturation that the devices display if P_{sp} drops below a specific threshold. Inadequate P_{sp} weakens Ohmic contacts, as shown in Figure 4.2(b), which raises resistance because of an extra barrier at the contact regions. To counteract weakened band bending at the contact surface, this problem can be lessened by choosing a metal contact having a work function nearer

doi:10.6342/NTU202403452

to the band edge. The P-MOSFETs operate on the same principles.

4.6 2D Carrier Distribution

In Figure 4.11, which illustrates the ON and OFF characteristics of the P-MOSFET and N-MOSFET devices with a HfO_2 gate and $t_{ox} = 1$ nm, we present the two-dimensional distribution map of the majority carrier under various operating conditions to understand the carrier distribution within the device. The regions where the MoSSe touches the metal are designated as the source and drain zones, resulting in a relatively high carrier concentration of approximately 10^{14} cm^{-3} (indicated by the color green). The farther the location is from the contact zone, the more gradually the carrier concentration decreases. The presence of two high-concentration patches adjacent to the source and drain areas is due to the 10-nm gate metal isolation design. Due to the thicker oxide, the MoSSe dipole effect is eliminated, leaving the carrier gas in place. Using the P-MOSFET as an example, we can observe that when a negative gate bias of -0.5 V is applied, holes are attracted into the channel region, forming a strong inversion layer and activating the device (Fig. 4.11(a)). Conversely, Fig. 4.11(b) shows the device in the OFF state when a positive gate bias of 0.5 V is applied, causing holes to be depleted and the inversion layer to vanish. For the N-MOSFET, a similar result is achieved; the only difference is that when $V_g = 0.5$ V (Fig. 4.11(c)) is applied, a strong inversion layer forms, and when $V_g = -0.5$ V (Fig. 4.11(d)) is applied, the inversion layer disappears.

Utilizing a 2D simulation of a double-gate N-MOSFET device operating in both depletion (HfO_2, $t_{ox} = 10$ nm) and enhancement (HfO_2, $t_{ox} = 1$ nm) modes, Figure 4.12 illustrates the impact of the intrinsic dipole on the N-MOSFET channel region. To demon-

doi:10.6342/NTU202403452

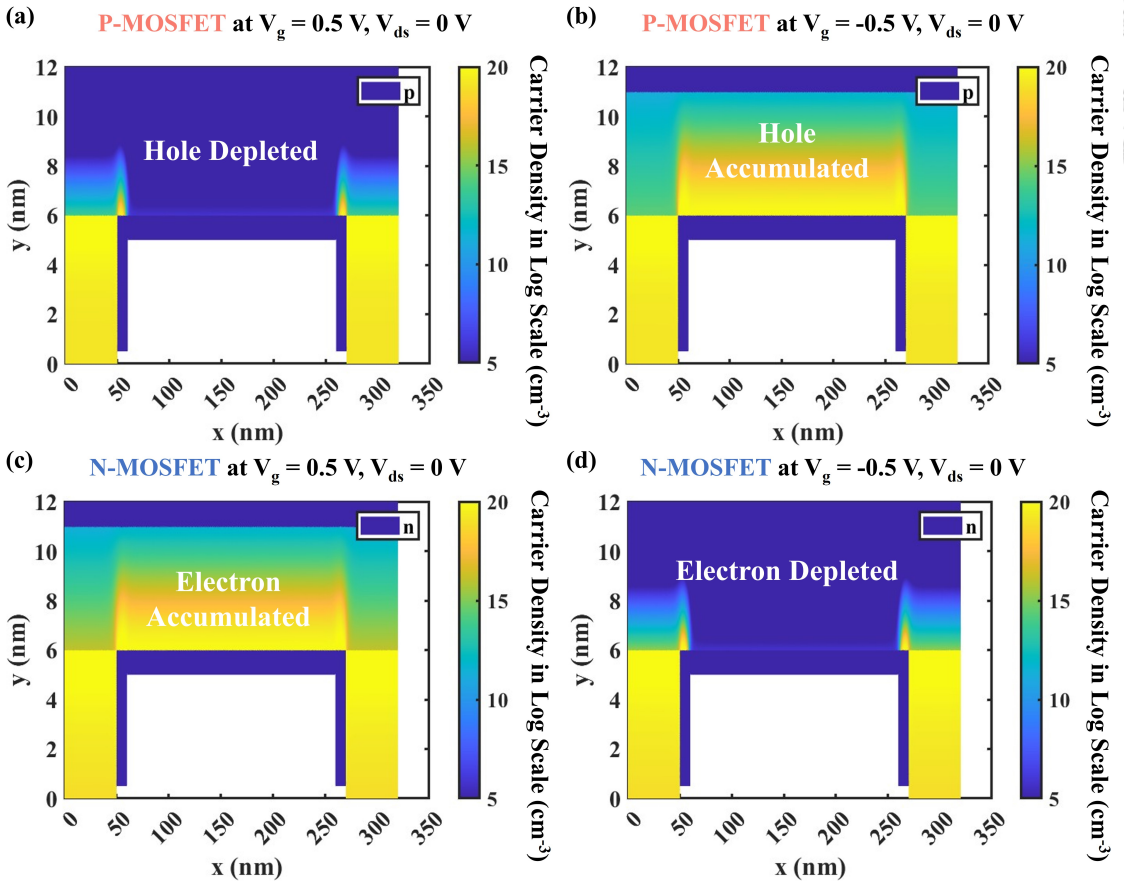

Figure 4.11: Simulated majority carrier concentration plots for double-gate HfO_2 devices are shown for (a) P-MOSFET under $V_g = -0.5$ V, (b) P-MOSFET under $V_g = 0.5$ V, (c) N-MOSFET under $V_g = 0.5$ V, and (d) N-MOSFET under $V_g = -0.5$ V bias conditions. For observational convenience, the V_{ds} bias is set to zero. This work has been published in [3].

strate the effect of P_{sp} on carrier distribution in the MoSSe channel, an additional dataset labeled "Without P_{sp}", representing standard TMD materials, is provided. To observe the carrier distribution under optimal conditions, all biases are set to zero.

When arrangements are made without an inherent dipole (as in Figs. 4.12(a) and (c)), regardless of oxide thickness, the electron concentration stays about 10^{10} cm^{-3} and no 2DEG is seen across the channel region. On the other hand, an intrinsic dipole acts as an internal electric field in the channel layer when it is present in the channel region. Figs show this field, which is affected by P_{sp}.(b) and (d) of 4.12. As a result, electrons line

doi:10.6342/NTU202403452

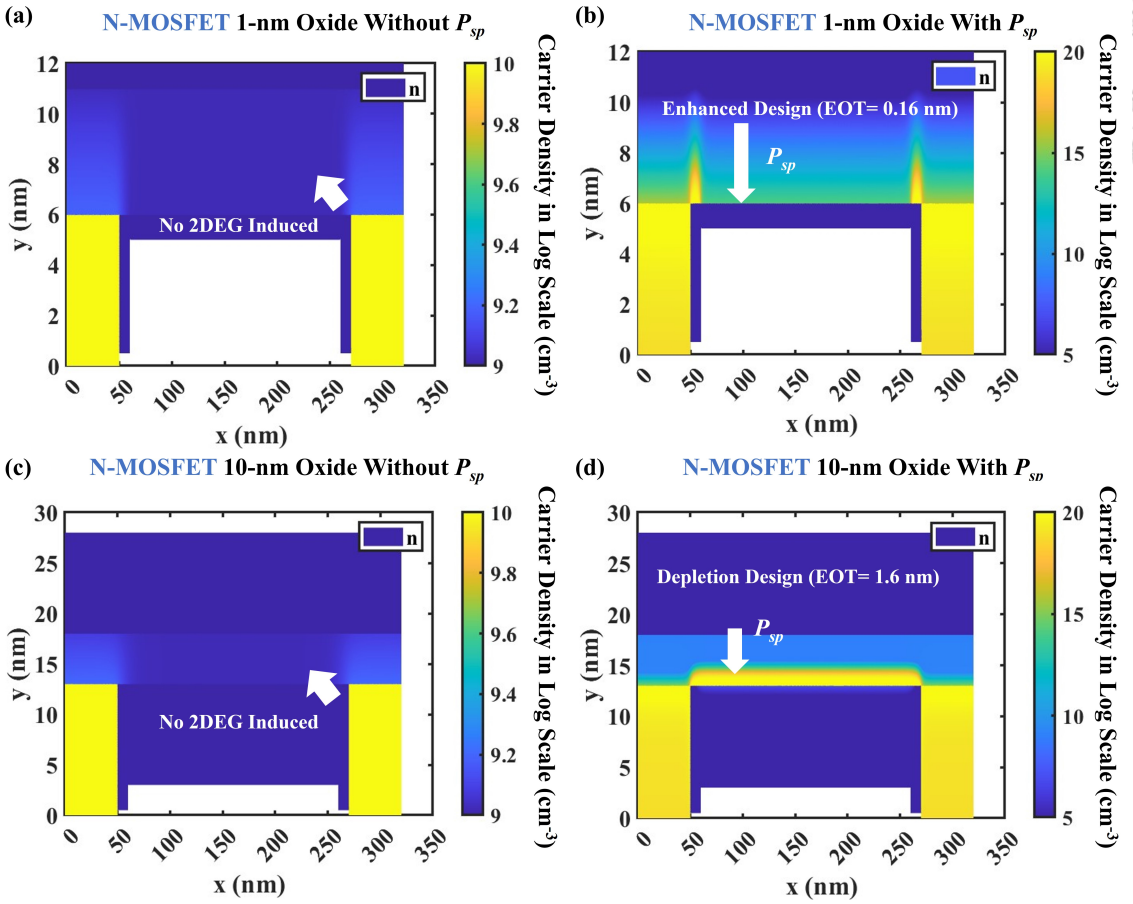

Figure 4.12: N-MOSFET 2D majority carrier concentration plots of enhance (HfO_2 t_{ox} = 1 nm) mode design (a) without P_{sp} and (b) 4.76×10^{13} cm^{-2} P_{sp} in the channel layer. And N-MOSFET depletion (HfO_2 t_{ox} = 10 nm) mode design (c) without P_{sp} and (d) 4.76×10^{13} cm^{-2} P_{sp} in the channel layer. All results are under an equilibrium state to observe the effect of the intrinsic dipole on carrier distribution in the channel. This work has been published in [3].

up with P_{sp}, creating a 2DEG that resembles a typical GaN-based n-FET channel. This typical 2DEG development will be seen in any JTMD with a prominent P_{sp}.

EOT primarily regulates the intensity of the two-dimensional electron gas (2DEG). The enhancement mode is indicated by an EOT value of 0.16 nm (Fig. 4.12(b)). As EOT extends to 1.6 nm (Fig. 4.12(d)), the number of electrons in the channel near the source and drain sides sharply increases, leading to a transition from enhancement to depletion mode. The predominant carrier distribution of P-MOSFETs is similar to that of N-MOSFETs, resulting in comparable outcomes.

doi:10.6342/NTU202403452

Chapter 5

Conclusion

This thesis has demonstrated how we utilize the intrinsic dipole properties of JT-MDs to design a CMOSFET, focusing particularly on MoSSe. Our investigation covers various heterostructures, including Gr/AA′A-MoSSe/Gr and 2L-MoSSe/Al (111) face, as well as 2L-MoSSe/Cu (111) face structures, analyzed using first-principles density functional theory. We explore the interactions between MoSSe, graphene, aluminum, and copper electrodes, identifying characteristics such as Schottky barriers and Ohmic contacts. Leveraging MoSSe's strong dipole field, we create n- and p-type contact regions, simplifying material selection for CMOSFETs. Our proposed horizontal CMOSFET architecture offers fabrication reliability and integration advantages.

Device simulations provide insights into spontaneous polarization due to band bending and related carrier distribution, with an optimized equivalent oxide thickness of 0.312 nm favoring the MOSFET's depletion and enhancement modes threshold. We discuss the influence of spontaneous polarization magnitude, crucial for achieving Ohmic contact and forming the channel's two-dimensional electron/hole gas. The majority carrier plots demonstrate the device's capability to control carriers in the MoSSe channel region,

doi:10.6342/NTU202403452

highlighting its potential for low-voltage logic elements in integrated circuits. The surface polarization strategy employed suggests the possibility of forming MOSFETs from any JTMD, provided the 2D material exhibits a strong intrinsic out-of-plane dipole.

In addition, we have explored the absorption properties of MoSSe, revealing its potential for optical applications beyond its fundamental transport characteristics. By utilizing first principles combined with interpolation methods under sufficient fine meshing situations, we calculated the JDOS, absorption coefficient, and band orbital contributions. Our results show that Mo's *d* orbitals dominate the band edges, with significant electron transitions observed in the direct band gap at the K point. The calculated absorption coefficient of $2.04 \times 10^5 cm^{-1}$ (with $\mathbf{E}_p$ of 26 eV) for 1L-MoSSe at band edge, though slightly lower than MoS_2, still surpasses typical semiconductors, underscoring its efficacy in optical devices. The extracted optical values can be further utilized in optoelectronic device simulation in a similar approach to MoSSe CMOSFET.

Overall, this work presents a promising material MoSSe, offering its insights into interfaces, optical, and CMOSFET device characteristics, which may be extended to future electronic or optoelectronic applications.

doi:10.6342/NTU202403452

References

[1] A. Pezeshki, H. Shokouh, S. Hossein, P. J. Jeon, I. Shackery, J. S. Kim, I.-K. Oh, S. C. Jun, H. Kim, and S. Im, "Static and dynamic performance of complementary inverters based on nanosheet α-$MoTe_2$ p-channel and MoS_2 n-channel transistors," *ACS Nano*, vol. 10, pp. 1118–1125, 2016.

[2] D. S. Sholl and J. A. Steckel, *Density functional theory: a practical introduction*. John Wiley & Sons, 2022.

[3] Y.-P. Chiu, H.-W. Huang, and Y.-R. Wu, "Utilizing the janus mosse surface polarization in designing complementary metal-oxide-semiconductor field-effect transistors," *Physical Review Applied*, vol. 21, no. 4, p. 044046, 2024.

[4] H.-C. Pai and Y.-R. Wu, "Investigating the high field transport properties of Janus WSSe and MoSSe by DFT analysis and Monte Carlo simulations," *J. Appl. Phys.*, vol. 131, no. 14, p. 144303, 2022.

[5] M. Ye, D. Zhang, and Y. K. Yap, "Recent advances in electronic and optoelectronic devices based on two-dimensional transition metal dichalcogenides," *Electronics*, vol. 6, no. 2, p. 43, 2017.

[6] A. Chaves, J. G. Azadani, H. Alsalman, D. R. da Costa, R. Frisenda, A. J. Chaves, S. H. Song, Y. D. Kim, D. He, J. Zhou, A. Castellanos-Gomez, F. M. Peeters, Z. Liu,

doi:10.6342/NTU202403452

C. L. Hinkle, S.-H. Oh, P. D. Ye, S. J. Koester, Y. H. Lee, P. Avouris, X. Wang, and T. Low, "Bandgap engineering of two-dimensional semiconductor materials," *npj 2D Mater. Appl.*, vol. 4, p. 29, 2020.

[7] M. Bernardi, M. Palummo, and J. C. Grossman, "Extraordinary sunlight absorption and one nanometer thick photovoltaics using two-dimensional monolayer materials," *Nano Letters*, vol. 13, no. 8, pp. 3664–3670, 2013.

[8] X. Li and H. Zhu, "Two-dimensional MoS_2: Properties, preparation, and applications," *Journal of Materiomics*, vol. 1, no. 1, pp. 33–44, 2015.

[9] M. Chhowalla, H. S. Shin, G. Eda, L.-J. Li, K. P. Loh, and H. Zhang, "The chemistry of two-dimensional layered transition metal dichalcogenide nanosheets," *Nature Chemistry*, vol. 5, no. 4, pp. 263–275, 2013.

[10] M. Chhowalla, D. Jena, and H. Zhang, "Two-dimensional semiconductors for transistors," *Nat. Rev. Mater.*, vol. 1, p. 16052, 2016.

[11] F.-X. R. Chen, N. Kawakami, C.-T. Lee, P.-Y. Shih, Z.-C. Wu, Y.-C. Yang, H.-W. Tu, W.-B. Jian, C. Hu, and C.-L. Lin, "Visualizing correlation between carrier mobility and defect density in MoS_2 FET," *Appl. Phys. Lett.*, vol. 121, no. 15, p. 151601, 2022.

[12] B. Radisavljevic, A. Radenovic, J. Brivio, V. Giacometti, and A. Kis, "Single-layer MoS_2 transistors," *Nat. Nanotechnol.*, vol. 6, pp. 147–150, 2011.

[13] M. I. Serna, S. H. Yoo, S. Moreno, Y. Xi, J. P. Oviedo, H. Choi, H. N. Alshareef, M. J. Kim, M. Minary-Jolandan, and M. A. Quevedo-Lopez, "Large-area deposition of MoS_2 by pulsed laser deposition with *in situ* thickness control," *ACS Nano*, vol. 10, no. 6, pp. 6054–6061, 2016.

doi:10.6342/NTU202403452

[14] Y. Zhang, Y. Zhang, Q. Ji, J. Ju, H. Yuan, J. Shi, T. Gao, D. Ma, M. Liu, Y. Chen, *et al.*, "Controlled growth of high-quality monolayer WS_2 layers on sapphire and imaging its grain boundary," *ACS Nano*, vol. 7, no. 10, pp. 8963–8971, 2013.

[15] C. M. Orofeo, S. Suzuki, Y. Sekine, and H. Hibino, "Scalable synthesis of layer-controlled WS_2 and MoS_2 sheets by sulfurization of thin metal films," *Appl. Phys. Lett.*, vol. 105, no. 8, p. 083112, 2014.

[16] D. Ovchinnikov, A. Allain, Y.-S. Huang, D. Dumcenco, and A. Kis, "Electrical transport properties of single-layer WS_2," *ACS Nano*, vol. 10, pp. 8174–8181, 2014.

[17] J. Choi, H. Zhang, and J. H. Choi, "Modulating optoelectronic properties of two-dimensional transition metal dichalcogenide semiconductors by photoinduced charge transfer," *ACS Nano*, vol. 10, no. 1, pp. 1671–1680, 2016.

[18] G.-H. Lee, Y.-J. Yu, X. Cui, N. Petrone, C.-H. Lee, M. S. Choi, D.-Y. Lee, C. Lee, W. J. Yoo, K. Watanabe, T. Taniguchi, C. Nuckolls, P. Kim, and J. Hone, "Flexible and Transparent MoS_2 Field-Effect Transistors on Hexagonal Boron Nitride-Graphene Heterostructures," *ACS Nano*, vol. 7, no. 9, pp. 7931–7936, 2013.

[19] K. C. Kwon, J. H. Baek, K. Hong, S. Y. Kim, and H. W. Jang, "Memristive devices based on two-dimensional transition metal chalcogenides for neuromorphic computing," *Nano-Micro Letters*, vol. 14, no. 1, p. 58, 2022.

[20] R. Ge, X. Wu, M. Kim, J. Shi, S. Sonde, L. Tao, Y. Zhang, J. C. Lee, and D. Akinwande, "Atomristor: nonvolatile resistance switching in atomic sheets of transition metal dichalcogenides," *Nano letters*, vol. 18, no. 1, pp. 434–441, 2018.

[21] Y.-C. Chen, Y.-T. Chao, E. Chen, C.-H. Wu, and Y.-R. Wu, "Studies of two-

doi:10.6342/NTU202403452

dimensional material resistive random-access memory by kinetic monte carlo simulations," *Phys. Rev. Mater.*, vol. 7, p. 094001, 2023.

[22] J. Zhang, T. Ji, H. Jin, Z. Wang, M. Zhao, D. He, G. Luo, and B. Mao, "Mild liquid-phase exfoliation of transition metal dichalcogenide nanosheets for hydrogen evolution," *ACS Applied Nano Materials*, vol. 5, no. 6, pp. 8020–8028, 2022.

[23] Y. Li, G. Kuang, Z. Jiao, L. Yao, and R. Duan, "Recent progress on the mechanical exfoliation of 2D transition metal dichalcogenides," *Materials Research Express*, vol. 9, no. 12, p. 122001, 2022.

[24] E. Pollmann, L. Madauß, S. Schumacher, U. Kumar, F. Heuvel, C. vom Ende, S. Yilmaz, S. Güngörmüs, and M. Schleberger, "Apparent differences between single layer molybdenum disulphide fabricated via chemical vapour deposition and exfoliation," *Nanotechnology*, vol. 31, no. 50, p. 505604, 2020.

[25] R. H. Zha, P. Delparastan, T. D. Fink, J. Bauer, T. Scheibel, and P. B. Messersmith, "Universal nanothin silk coatings via controlled spidroin self-assembly," *Biomater. Sci.*, vol. 7, pp. 683–695, 2019.

[26] M. K. Bayazit, L. Xiong, C. Jiang, S. J. A. Moniz, E. White, M. S. P. Shaffer, and J. Tang, "Defect-free single-layer graphene by 10 s microwave solid exfoliation and its application for catalytic water splitting," *ACS Applied Materials & Interfaces*, vol. 13, no. 24, pp. 28600–28609, 2021.

[27] L. Chen, Z. Cheng, S. He, X. Zhang, K. Deng, D. Zong, Z. Wu, and M. Xia, "Large-area single-crystal tmd growth modulated by sapphire substrates," *Nanoscale*, vol. 16, pp. 978–1004, 2024.

doi:10.6342/NTU202403452

[28] M. O'Brien, N. McEvoy, T. Hallam, H.-Y. Kim, N. C. Berner, D. Hanlon, K. Lee, J. N. Coleman, and G. S. Duesberg, "Transition metal dichalcogenide growth via close proximity precursor supply," *Scientific Reports*, vol. 4, p. 7374, 2014.

[29] Y. Zuo, C. Liu, L. Ding, R. Qiao, J. Tian, C. Liu, Q. Wang, G. Xue, Y. You, Q. Guo, J. Wang, Y. Fu, K. Liu, X. Zhou, H. Hong, M. Wu, X. Lu, R. Yang, G. Zhang, D. Yu, E. Wang, X. Bai, F. Ding, and K. Liu, "Robust growth of two-dimensional metal dichalcogenides and their alloys by active chalcogen monomer supply," *Nature Communications*, vol. 13, p. 1007, 2022.

[30] Q. Liang, Q. Zhang, X. Zhao, M. Liu, and A. T. S. Wee, "Defect engineering of two-dimensional transition-metal dichalcogenides: Applications, challenges, and opportunities," *ACS Nano*, vol. 15, no. 2, pp. 2165–2181, 2021.

[31] J. Kucharek, R. Bożek, and W. Pacuski, "Molecular beam epitaxy growth of Transition Metal Dichalcogenide (Mo, Mn)Se_2 on 2D, 3D and polycrystalline substrates," *Materials Science in Semiconductor Processing*, vol. 163, p. 107550, 2023.

[32] Y. Liu, X. Duan, H.-J. Shin, S. Park, Y. Huang, and X. Duan, "Promises and prospects of two-dimensional transistors," *Nature*, vol. 591, p. 43–53, 2021.

[33] Y. Xiong, D. Xu, Y. Feng, G. Zhang, P. Lin, and X. Chen, "P-type 2d semiconductors for future electronics," *Advanced Materials*, vol. 35, no. 50, p. 2206939, 2023.

[34] L. Zhang, Y. Zhang, X. Sun, K. Jia, Q. Zhang, Z. Wu, and H. Yin, "High-performance multilayer WSe_2 p-type field effect transistors with Pd contacts for circuit applications," *J. Mater. Sci.: Mater. Electron.*, vol. 32, pp. 17427–17435, 2021.

doi:10.6342/NTU202403452

[35] D. H. Keum, S. Cho, J. H. Kim, D.-H. Choe, H.-J. Sung, M. Kan, H. Kang, J.-Y. Hwang, S. W. Kim, H. Yang, K. J. Chang, and Y. H. Lee, "Bandgap opening in few-layered monoclinic $MoTe_2$," *Nature Physics*, vol. 11, no. 6, pp. 482–486, 2015.

[36] N. Liu, J. Baek, S. M. Kim, S. Hong, Y. K. Hong, Y. S. Kim, H.-S. Kim, S. Kim, and J. Park, "Improving the stability of high-performance multilayer MoS_2 field-effect transistors," *ACS Applied Materials & Interfaces*, vol. 9, no. 49, pp. 42943–42950, 2017.

[37] A. Daus, S. Vaziri, V. Chen, Ç. Köroğlu, R. W. Grady, C. S. Bailey, H. R. Lee, K. Schauble, K. Brenner, and E. Pop, "High-performance flexible nanoscale transistors based on transition metal dichalcogenides," *Nature Electronics*, vol. 4, no. 7, pp. 495–501, 2021.

[38] S. Z. Butler, S. M. Hollen, L. Cao, Y. Cui, J. A. Gupta, H. R. Gutiérrez, T. F. Heinz, S. S. Hong, J. Huang, A. F. Ismach, *et al.*, "Progress, challenges, and opportunities in two-dimensional materials beyond graphene," *ACS nano*, vol. 7, no. 4, pp. 2898–2926, 2013.

[39] S. Zhang, H. Xu, F. Liao, Y. Sun, K. Ba, Z. Sun, Z.-J. Qiu, Z. Xu, H. Zhu, L. Chen, *et al.*, "Wafer-scale transferred multilayer MoS_2 for high performance field effect transistors," *Nanotechnology*, vol. 30, no. 17, p. 174002, 2019.

[40] Q. Tao, R. Wu, Q. Li, L. Kong, Y. Chen, J. Jiang, Z. Lu, B. Li, W. Li, Z. Li, *et al.*, "Reconfigurable electronics by disassembling and reassembling van der waals heterostructures," *Nature communications*, vol. 12, no. 1, p. 1825, 2021.

[41] X. Zhang, J. Lai, and T. Gray, "Recent progress in low-temperature CVD growth of 2D materials," *Oxford Open Materials Science*, vol. 3, no. 1, p. 010, 2023.

doi:10.6342/NTU202403452

[42] A. Allain, J. Kang, K. Banerjee, and A. Kis, "Electrical contacts to two-dimensional semiconductors," *Nat. Mater.*, vol. 14, pp. 1195–1205, 2015.

[43] Y. Zheng, J. Gao, C. Han, and W. Chen, "Ohmic contact engineering for two-dimensional materials," *Cell Rep. Phys. Sci.*, vol. 2, p. 100298, 2021.

[44] S. Andleeb, J. Eom, N. R. Naz, and A. K. Singh, "MoS_2 field-effect transistor with graphene contacts," *Journal of Materials Chemistry C*, vol. 5, no. 32, pp. 8308–8314, 2017.

[45] Y. Du, L. Yang, J. Zhang, H. Liu, K. Majumdar, P. D. Kirsch, and P. D. Ye, "MoS_2 field-effect transistors with graphene/metal heterocontacts," *IEEE Electron Device Letters*, vol. 35, no. 5, p. 599–601, 2014.

[46] Y. Shi, K. K. Kim, A. Reina, M. Hofmann, L.-J. Li, and J. Kong, "Work function engineering of graphene electrode via chemical doping," *ACS nano*, vol. 4, no. 5, pp. 2689–2694, 2010.

[47] J. Kang, W. Liu, D. Sarkar, D. Jena, and K. Banerjee, "Computational study of metal contacts to monolayer transition-metal dichalcogenide semiconductors," *Phys. Rev. X*, vol. 4, p. 031005, 2014.

[48] B. Ouyang, S. Xiong, and Y. Jing, "Tunable phase stability and contact resistance of monolayer transition metal dichalcogenides contacts with metal," *npj 2D Mater. Appl.*, vol. 2, p. 13, 2018.

[49] H. Tang, B. Shi, Y. Pan, J. Li, X. Zhang, J. Yan, S. Liu, J. Yang, L. Xu, J. Yang, M. Wu, and J. Lu, "Schottky contact in monolayer WS_2 field-effect transistors," *Adv. Theory Simul.*, vol. 2, p. 1900001, 2019.

doi:10.6342/NTU202403452

[50] R. T. Tung, "The physics and chemistry of the Schottky barrier height," *Appl. Phys. Rev.*, vol. 1, no. 1, 2014.

[51] R. Younas, G. Zhou, and C. L. Hinkle, "A perspective on the doping of transition metal dichalcogenides for ultra-scaled transistors: Challenges and opportunities," *Appl. Phys. Lett.*, vol. 122, no. 16, 2023.

[52] G. Mirabelli, M. Schmidt, B. Sheehan, K. Cherkaoui, S. Monaghan, I. Povey, M. McCarthy, A. P. Bell, R. Nagle, F. Crupi, *et al.*, "Back-gated Nb-doped MoS2 junctionless field-effect-transistors," *AIP Advances*, vol. 6, no. 2, 2016.

[53] M. R. Laskar, D. N. Nath, L. Ma, E. W. Lee, C. H. Lee, T. Kent, Z. Yang, R. Mishra, M. A. Roldan, J.-C. Idrobo, *et al.*, "p-type doping of MoS_2 thin films using Nb," *Applied Physics Letters*, vol. 104, no. 9, 2014.

[54] J. Gao and M. Gupta, "Titanium disulfide as schottky/ohmic contact for monolayer molybdenum disulfide," *npj 2D Materials and Applications*, vol. 4, no. 1, p. 26, 2020.

[55] D. Pierucci, H. Henck, Z. Ben Aziza, C. H. Naylor, A. Balan, J. E. Rault, M. G. Silly, Y. J. Dappe, F. Bertran, P. Le Fèvre, F. Sirotti, A. T. C. Johnson, and A. Ouerghi, "Tunable doping in hydrogenated single layered molybdenum disulfide," *ACS nano*, vol. 11, no. 2, pp. 1755–1761, 2017.

[56] L. Kong, X. Zhang, Q. Tao, M. Zhang, W. Dang, Z. Li, L. Feng, L. Liao, X. Duan, and Y. Liu, "Doping-free complementary WSe_2 circuit via van der Waals metal integration," *Nat. Commun.*, vol. 11, p. 1866, 2020.

[57] N. Zhao and U. Schwingenschlögl, "Dipole-induced Ohmic contacts between monolayer Janus MoSSe and bulk metals," *npj 2D Mater. Appl.*, vol. 131, p. 72, 2022.

doi:10.6342/NTU202403452

[58] S. M. Sze, Y. Li, and K. K. Ng, *Physics of Semiconductor Devices*. Wiley, 2021.

[59] H. Liu, A. T. Neal, Z. Zhu, Z. Luo, X. Xu, D. Tománek, and P. D. Ye, "Phosphorene: An unexplored 2D semiconductor with a high hole mobility," *ACS Nano*, vol. 8, pp. 4033–4041, 2014.

[60] S. Das, M. Dubey, and A. Roelofs, "High gain, low noise, fully complementary logic inverter based on bi-layer WSe_2 field effect transistors," *Appl. Phys. Lett.*, vol. 105, no. 8, 2014.

[61] A.-J. Cho, K. C. Park, and J.-Y. Kwon, "A high-performance complementary inverter based on transition metal dichalcogenide field-effect transistors," *Nanoscale Res. Lett.*, vol. 10, p. 115, 2015.

[62] X. Xiong, A. Tong, X. Wang, S. Liu, X. Li, R. Huang, and Y. Wu, "Demonstration of vertically-stacked CVD monolayer channels: MoS_2 nanosheets GAA-FET with $I_{on} > 700$ μA/μm and MoS_2/WSe_2 CFET," in *2021 IEEE International Electron Devices Meeting (IEDM)*, pp. 7.5.1–7.5.4, 2021.

[63] S. Ullah, X. Yang, H. Q. Ta, M. Hasan, A. Bachmatiuk, K. Tokarska, B. Trzebicka, L. Fu, and M. H. Rummeli, "Graphene transfer methods: A review," *Nano Res.*, vol. 14, pp. 3756–3772, 2021.

[64] Y.-F. Lin, Y. Xu, S.-T. Wang, S.-L. Li, M. Yamamoto, A. Aparecido-Ferreira, W. Li, H. Sun, S. Nakaharai, W.-B. Jian, K. Ueno, and K. Tsukagoshi, "Ambipolar $MoTe_2$ transistors and their applications in logic circuits," *Adv. Mater.*, vol. 26, no. 20, pp. 3263–3269, 2014.

[65] J. Singh, *Electronic and optoelectronic properties of semiconductor structures*. Cambridge University Press, 2007.

doi:10.6342/NTU202403452

[66] Z. Jin, X. Li, J. T. Mullen, and K. W. Kim, "Intrinsic transport properties of electrons and holes in monolayer transition-metal dichalcogenides," *Phys. Rev. B*, vol. 90, p. 045422, 2014.

[67] A. Sebastian, R. Pendurthi, T. H. Choudhury, J. M. Redwing, and S. Das, "Benchmarking monolayer MoS_2 and WS_2 field-effect transistors," *Nature communications*, vol. 12, no. 1, p. 693, 2021.

[68] S. Larentis, B. Fallahazad, and E. Tutuc, "Field-effect transistors and intrinsic mobility in ultra-thin $MoSe_2$ layers," *Applied Physics Letters*, vol. 101, no. 22, p. 223104, 2012.

[69] Y. Xia, L. Wei, J. Deng, L. Zong, C. Wang, X. Chen, F. Liang, C. Luo, W. Bao, Z. Xu, *et al.*, "Tuning electrical and optical properties of $MoSe_2$ transistors via elemental doping," *Advanced Materials Technologies*, vol. 5, no. 7, p. 2000307, 2020.

[70] Q. Cao, Y.-W. Dai, J. Xu, L. Chen, H. Zhu, Q.-Q. Sun, and D. W. Zhang, "Realizing stable p-type transporting in two-dimensional WS_2 films," *ACS Applied Materials & Interfaces*, vol. 9, no. 21, pp. 18215–18221, 2017.

[71] S. Das, M. Dubey, and A. Roelofs, "High gain, low noise, fully complementary logic inverter based on bi-layer WSe_2 field effect transistors," *Applied Physics Letters*, vol. 105, no. 8, 2014.

[72] Y.-C. Lin, C. Liu, Y. Yu, E. Zarkadoula, M. Yoon, A. A. Puretzky, L. Liang, X. Kong, Y. Gu, A. Strasser, H. M. I. Meyer, M. Lorenz, M. F. Chisholm, I. N. Ivanov, C. M. Rouleau, G. Duscher, K. Xiao, and D. B. Geohegan, "Low energy implantation into transition-metal dichalcogenide monolayers to form Janus structures," *ACS Nano*, vol. 14, no. 4, pp. 3896–3906, 2020.

doi:10.6342/NTU202403452

[73] A.-Y. Lu, H. Zhu, J. Xiao, C.-P. Chuu, Y. Han, M.-H. Chiu, C.-C. Cheng, C.-W. Yang, K.-H. Wei, Y. Yang, Y. Wang, D. Sokaras, D. Nordlund, P. Yang, D. A. Muller, M.-Y. Chou, X. Zhang, and L.-J. Li, "Janus monolayers of transition metal dichalcogenides," *Nat. Nanotechnol.*, vol. 12, pp. 744–749, 2017.

[74] D. B. Trivedi, G. Turgut, Y. Qin, M. Y. Sayyad, D. Hajra, M. Howell, L. Liu, S. Yang, N. H. Patoary, H. Li, M. M. Petrić, M. Meyer, M. Kremser, M. Barbone, G. Soavi, A. V. Stier, K. Müller, S. Yang, I. S. Esqueda, H. Zhuang, J. J. Finley, and S. Tongay, "Room-temperature synthesis of 2D Janus crystals and their heterostructures," *Adv. Mater.*, vol. 32, no. 50, p. 2006320, 2020.

[75] R. Chaurasiya, G. Gupta, and A. Dixit, "Ultrathin Janus WSSe buffer layer for W(S/Se)$_2$ absorber based solar cells: A hybrid, DFT and macroscopic, simulation studies," *Sol. Energy Mater. Sol. Cells*, vol. 201, p. 110076, 2019.

[76] M. Petrić, M. Kremser, M. Barbone, Y. Qin, Y. Sayyad, Y. Shen, S. Tongay, J. Finley, A. Botello-Méndez, and K. Müller, "Raman spectrum of Janus transition metal dichalcogenide monolayers WSSe and MoSSe," *Phys. Rev. B*, vol. 103, p. 035414, 2021.

[77] D. Kong, F. Tian, Y. Xu, S. Zhu, Z. Yu, L. Xiong, P. Li, H. Wei, X. Zheng, and M. Peng, "Polarity reversal and strain modulation of Janus MoSSe/GaN polar semiconductor heterostructures," *Phys. Chem. Chem. Phys.*, vol. 25, pp. 30361–30372, 2023.

[78] L. Zhang, Z. Yang, T. Gong, R. Pan, H. Wang, Z. Guo, H. Zhang, and X. Fu, "Recent advances in emerging Janus two-dimensional materials: From fundamental physics to device applications," *J. Mater. Chem. A*, vol. 8, pp. 8813–8830, 2020.

doi:10.6342/NTU202403452

[79] L. Zhang, Y. Xia, X. Li, L. Li, X. Fu, J. Cheng, and R. Pan, "Janus two-dimensional transition metal dichalcogenides," *J. Appl. Phys.*, vol. 131, no. 23, p. 230902, 2022.

[80] Y.-Q. Chen, H.-H. Zhang, B. Wen, X.-B. Li, X.-L. Wei, W.-J. Yin, L.-M. Liu, and G. Teobaldi, "The role of permanent and induced electrostatic dipole moments for Schottky barriers in Janus MXY/graphene heterostructures: A first-principles study," *Dalton Trans.*, vol. 51, pp. 9905–9914, 2022.

[81] M. Palsgaard, T. Gunst, T. Markussen, K. S. Thygesen, and M. Brandbyge, "Stacked Janus device concepts: Abrupt pn-junctions and cross-plane channels," *Nano Lett.*, vol. 18, no. 11, pp. 7275–7281, 2018.

[82] X. Liu, P. Gao, W. Hu, and J. Yang, "Photogenerated-carrier separation and transfer in two-dimensional Janus transition metal dichalcogenides and graphene van der Waals sandwich heterojunction photovoltaic cells," *J. Phys. Chem. Lett.*, vol. 11, no. 10, pp. 4070–4079, 2020.

[83] K. Momma and F. Izumi, "Vesta: a three-dimensional visualization system for electronic and structural analysis," *Journal of Applied crystallography*, vol. 41, no. 3, pp. 653–658, 2008.

[84] H. L. Skriver and N. M. Rosengaard, "Surface energy and work function of elemental metals," *Phys. Rev. B*, vol. 46, no. 11, p. 7157, 1992.

[85] N. Marzari, A. A. Mostofi, J. R. Yates, I. Souza, and D. Vanderbilt, "Maximally localized wannier functions: Theory and applications," *Rev. Mod. Phys.*, vol. 84, pp. 1419–1475, 2012.

[86] P. Giannozzi, S. Baroni, N. Bonini, M. Calandra, R. Car, C. Cavazzoni, D. Ceresoli,

doi:10.6342/NTU202403452

G. L. Chiarotti, M. Cococcioni, I. Dabo, A. D. Corso, S. de Gironcoli, S. Fabris, G. Fratesi, R. Gebauer, U. Gerstmann, C. Gougoussis, A. Kokalj, M. Lazzeri, L. Martin-Samos, N. Marzari, F. Mauri, R. Mazzarello, S. Paolini, A. Pasquarello, L. Paulatto, C. Sbraccia, S. Scandolo, G. Sclauzero, A. P. Seitsonen, A. Smogunov, P. Umari, and R. M. Wentzcovitch, "QUANTUM ESPRESSO: A modular and open-source software project for quantum simulations of materials," *J. Phys.: Condens. Matter*, vol. 21, no. 39, p. 395502, 2009.

[87] J. Noffsinger, F. Giustino, B. D. Malone, C.-H. Park, S. G. Louie, and M. L. Cohen, "Epw: A program for calculating the electron–phonon coupling using maximally localized wannier functions," *Computer Physics Communications*, vol. 181, no. 12, pp. 2140–2148, 2010.

[88] A. Laturia, M. L. V. de Put, and W. G. Vandenberghe, "Dielectric properties of hexagonal boron nitride and transition metal dichalcogenides: From monolayer to bulk," *npj 2D Mater. Appl.*, vol. 2, p. 6, 2018.

[89] D. R. Hamann, M. Schlüter, and C. Chiang, "Norm-conserving pseudopotentials," *Phys. Rev. Lett.*, vol. 43, pp. 1494–1497, 1979.

[90] S. Grimme, J. Antony, S. Ehrlich, and H. Krieg, "A consistent and accurate *ab initio* parametrization of density functional dispersion correction (DFT-D) for the 94 elements H–Pu," *J. Chem. Phys.*, vol. 132, no. 15, p. 154104, 2010.

[91] P.-F. Chen and Y.-R. Wu, "Calculation of Field Dependent Mobility in MoS_2 and WS_2 with Multi-Valley Monte Carlo Method," in *2021 International Symposium on VLSI Technology, Systems and Applications (VLSI-TSA)*, pp. 1–2, IEEE, 2021.

doi:10.6342/NTU202403452

[92] M. Mansouri, A.-M. G. Dezfuli, and H. Salehi, “Stacking effect on the orbital characters and transition probability of bilayer MoS_2,” *Physica Scripta*, vol. 98, no. 10, p. 105404, 2023.

[93] K. Kubra, M. R. Islam, M. S. Hasan Khan, M. S. Islam, and M. T. Hasan, “Study of Two-Dimensional Janus WXY (X≠Y= S, Se, and Te) Trilayer Homostructures for Photovoltaic Applications Using DFT Screening of Different Stacking Patterns,” *ACS Omega*, vol. 7, no. 15, pp. 12947–12955, 2022.

[94] C. Gong, G. Lee, B. Shan, E. M. Vogel, R. M. Wallace, and K. Cho, “First-principles study of metal‐graphene interfaces,” *J. Appl. Phys.*, vol. 108, no. 12, p. 123711, 2010.

[95] J. Bardeen and W. Shockley, “Deformation potentials and mobilities in non-polar crystals,” *Phys. Rev.*, vol. 80, pp. 72–80, 1950.

[96] Z. Shuai, L. Wang, and C. Song, *Theory of charge transport in carbon electronic materials*. Springer Science & Business Media, 2012.

[97] K. Zollner, P. E. F. Junior, and J. Fabian, “Strain-tunable orbital, spin-orbit, and optical properties of monolayer transition-metal dichalcogenides,” *Phys. Rev. B*, vol. 100, p. 195126, 2019.

[98] M. Wu, Y. I. Alivov, and H. Negi, Morkoç, “High-κ dielectrics and advanced channel concepts for Si MOSFET,” *J. Mater. Sci.: Mater. Electron.*, vol. 19, pp. 915–951, 2008.

[99] B. Kumar, B. K. Kaushik, and Y. S. Negi, “Perspectives and challenges for organic thin film transistors: Materials, devices, processes and applications,” *J. Mater. Sci.: Mater. Electron.*, vol. 25, pp. 1–30, 2014.

doi:10.6342/NTU202403452